PHONON MASER ACTION IN CADMIUM SULFIDE

by

MAX BLAKE BURBANK

B.Sc. (Hon), University of Alberta, 1964
M.Sc., University of Alberta, 1967

A DISSERTATION SUBMITTED IN PARTIAL FULFILMENT

OF THE REQUIREMENTS FOR THE DEGREE OF

DOCTOR OF PHILOSOPHY

in the Department

of

Physics

SIMON FRASER UNIVERSITY

November 1971

APPROVAL

Name: Max Blake Burbank

Degree: Doctor of Philosophy

Title of Thesis: Phonon Maser Action in Cadmium Sulfide

Examining Committe:

Chairman: K.E. Rieckhoff

R. R. Haering
Senior Supervisor

B. P. Clayman

D. Dunn

J. C. Irwin

A. B. Bhatia
External Examiner
Professor
University of Alberta

Date Approved: 16 December 1971

Abstract

Exploiting the characteristic that for certain polarizations net round trip acoustical gain exists within a field biased piezoelectric semiconductor, an acoustoelectric oscillator, "Phonon Maser", has been constructed from photoconductive Cadmium Sulfide.

A theoretical analysis of the system is undertaken, starting first with a linear analysis of ultrasonic gain. Adopting a phenomenological point of view the analysis is then extended to the one dimensional cavity structure characteristic of a Phonon Maser. From this analysis the conditions of spontaneous oscillation are established and expressions are derived for the corresponding threshold frequency, threshold drift velocity, and the tuning response of the system. In addition a limited non-linear analysis of the system has been attempted.

An experimental evaluation of the threshold response of the system is then reported and compared with the predictions of the linear, theoretical formulation. The agreement in most cases is very good, lending credibility to the theoretical formulation.

Table of Contents

Page

List of Tables

List of Illustrations

List of Symbols

$\alpha(2)$	second rank piezocaloric tensor
$b(1)$	first rank heat of polarization tensor
$\beta(3)$	third rank piezoelectric tensor
β_{ijk}, β_{ij}	components of the piezoelectric tensor
$c(4)$	fourth rank stiffness tensor
c_{ijkl}, c_{ij}	components of the stiffness tensor
$d(3)$	third rank direct piezoelectric tensor
$D(1)$	first rank electric displacement field
D_i	component of the electric displacement field
δ	threshold frequency correction factor (exact solution)
δ_1	threshold frequency correction factor (linearized approximation)
e	electric charge
$E(1)$	first rank electric field tensor
E_o	externally induced D.C. electric field
E, E_i	A.C. self-consistent electric field
$\varepsilon(2)$	second rank dielectric tensor
ε, ε_{ij}	real components of dielectric tensor
f	acoustoelectric frequency
$f(2)$	second rank thermal pressure tensor
G	feedback gain

γ, γ_-	$1 - v/s_o$; forward wave drift velocity parameter
γ_+	$1 + v/s_o$; reverse wave drift velocity parameter
Γ	piezo-acoustoelectric attenuation coefficient
Γ_N	$\Gamma_+ + \Gamma_-$; net round trip attenuation coefficient
Γ_L	$\alpha\omega^\beta$; lattice attenuation coefficient
Γ_T	$\Gamma_N + 2\Gamma_L$; total attenuation coefficient
$\Gamma_N^{(M)}$	maximized net round trip gain
I	light intensity/electric current
J	current density
k	$q + i\Gamma$; complex acoustical wave vector
K	Boltzman's constant
κ	thermal conductance
$\kappa(2)$	second rank inverse dielectric tensor
L	crystal thickness
μ	electron drift mobility
n	deviation from equilibrium charge density/ harmonic number
n_o	equilibrium charge density
p(1)	first rank pyroelectric tensor
P	pressure
P/V	power dissipation per unit volume

q	stiffened acoustical wave vector
q_o	unstiffened acoustical wave vector
Δq	$\frac{q_- - q_+}{2}$; difference wave vector
Q	thermal power (per unit volume)/ Quality factor
r	acoustical reflection coefficient
R	$\left[\frac{\varepsilon KT}{4\pi n_o e}\right]^{\frac{1}{2}}$; Debye screening radius
ρ	mass density of crystal
s	stiffened velocity of sound
s_o	unstiffened velocity of sound
$s(4)$	fourth rank compliance tensor
$S(2)$	second rank strain tensor
S_{ij}, S_i	components of strain tensor
$\mathscr{S}(0)$	zero rank entropy tensor
σ	electrical conductivity
t	time
T	temperature
ΔT	temperature differential
$T(2)$	second rank stress tensor
T_{ij}, T_i	components of stress tensor
τ	$\frac{\varepsilon}{4\pi\mu e n_o}$; dielectric relaxation time
u_i, u	material displacement
θ	acoustical boundary phase shift
Θ/C	absolute temperature divided by heat capacity

v	electron drift velocity
v_{th}	threshold drift velocity
V, V_-, V_+	voltage
ϕ	feedback gain angle
ω	$2\pi f$; angular frequency
ω_o	s_o/R; unconnected frequency of maximum gain
ω_m	$\omega_o(1+\delta)$; frequency of maximum gain
ω_D	$\frac{es_o^2}{\mu KT}$; diffusion frequency
ω_u	gain limited upper frequency
ω_L	gain limited lower frequency
$\omega_u(\Delta T)$	thermally limited upper frequency
x_i, x	position
χ	$\frac{4\pi\beta^2}{\varepsilon c}$; piezoelectric coupling coefficient
Z	electrical impedance
Ω	ohms

Acknowledgements

I would like to thank my supervisor, Dr. R.R. Haering for suggesting this project and for his continued and enthusiastic support throughout its development.

I would like also to extend my thanks to Miss Bridgette Anderson, Mrs. Bridgette Brix, and Mr. Joel Mercier for their invaluable technical assistance in preparing the samples.

Appreciation is also extended to Mr. Frank Wick and the members of his machine shop for their assistance

Credit and appreciation is also extended to Mrs. Donna Watt for her patience and proficiency in typing this thesis.

Finally, I would like to thank the International Nickel Company of Canada Limited, and Simon Fraser University for their financial support during the course of this research.

CHAPTER I

Introduction

1-1 Historical Development

In the study of propagating high-frequency (ultrasonic) elastic waves in solids, attention is generally directed at an analysis of the corresponding attenuation and phase velocity in terms of the fundamental properties of the medium. In general the study of attenuation divides itself broadly into an analysis of scattering and absorption processes. The analysis of phase velocity, on the other hand, is used most extensively in evaluating the relevant stiffness tensor.

In relation to the study of attenuation, the analysis of scattering processes relates most directly to the lattice properties of solids, such as: (i) the anharmonicity of the lattice potential (and subsequent coupling of the ultrasonic wave to the thermal phonon spectrum) and (ii) the influence and concentration of crystal defects and dislocations. The analysis of absorption processes, on the other hand, relates to such features as: (i) electron-phonon, (ii) phonon-magnon, and (iii) spin-phonon coupling

mechanisms within a solid.

Within this topical breakdown the phenomenon of Phonon Maser action comes under the heading of an electron-phonon (acoustoelectric) interaction. More specifically it related to the coupling between the acoustically-activated piezoelectric field and the conduction electrons of a piezoelectric semiconductor (and is aptly referred to as the piezo-acoustoelectric interaction).

The pioneering work in this field was initiated by J. J. Kyame (Ky-54) in a theoretical discussion of the influence of a non-zero conductivity within a piezoelectric. His principal conclusion was that the resulting dispersion relationship was complex, corresponding to a piezo-acousto-electric attenuation factor. However, at this time the existence of piezoelectric semiconductors had not come to light since most tests for piezoelectricity were of a static or quasi-static nature. For such measurements the finite conductivity of piezoelectric semiconductors effectively shorted out any induced fields and thus masked their piezo-electric character.

Prompted by an anomalous thermoelectric response in ZnO (Hu-59) and a photosensitive attenuation dependence in CdS (Ni-60), A.R. Hutson (Hu-60) set out to test the piezoelectric response of these two semiconductors. In an

effort to quench their conductivity, Lithium compensators were added to ZnO while CdS was sulfur annealed. In each case their conductivities were lowered to less than 10^{-10} $(\Omega\text{-cm})^{-1}$. At this point resonance-antiresonance measurements were carried out resulting in the determination of their respective piezoelectric coefficients. The surprising conclusion was that both ZnO and CdS proved more piezoelectrically active than quartz. Armed with this information, the next development came from A.R. Hutson and D.L. White (Hu-62) who carried out an extensive theoretical analysis of elastic wave propagation in piezoelectric semiconductors.

Shortly thereafter it occurred to D.L. White that the same interaction mechanism responsible for ultrasonic attenuation in piezoelectric semiconductors could, by the inclusion of a D.C. electric field, be exploited to bring about ultrasonic gain. The basic criterion was that the component of the resultant drift velocity in the direction of wave propagation must be greater than the corresponding velocity of sound. Using CdS, this idea was subsequently tested and varified (Hu-61). Folowing the initial theoretical analysis of ultrasonic gain in piezoelectric semiconductors by D.L. White (Wh-62), extensive theoretical and experimental interest was aroused: (Sp-62), (MF-63), (Sp-63), (Ec-63), (Sp-68), and (Gu-68). [Two good review papers on the topic are: (MF-66) and (Gu-69).]

It was pointed out in White's original paper (Wh-62) that although gain existed only for those waves travelling parallel to the electron flow, the attenuation of the reverse going wave was such that net round trip acoustical gain existed for a band of frequencies. Having thus identified the medium as acoustically active one has, in analogy with the optical laser, the possibility of structuring a piezo-acoustoelectrical oscillator, or more aptly a Phonon Maser. The analysis of such a device was first formulated by V.L. Gurevich and B.D. Laikhtman (Gu-66) and successfully constructed from CdS by D.L. White and W. Wang (Wh-66) at the Bell Telephone Laboratories, New Jersey. Subsequent to this work a group at the Royal Radar Establishment have undertaken a further study of the phenomenum using both CdS and ZnO: (Ma-67), (Ma-69), (Mr-69), (Mr-70), and (Hu-70). In addition some work was initiated in the Soviet Union by V.I. Baibakov (Ba-68).

1-2 Contributions of This Thesis

Throughout virtually all of the Phonon Maser work cited above no extensive effort has been made to develop a satisfactory theoretical formulation of the phenomenon nor to carry out any exhaustive evaluation of the experimental response in terms of such a model. Furthermore, in virtually all of the systems studied to date a pulsed, rather than

continuous, mode of operation has been used (in an effort to reduce the thermal duty cycle). In addition, it has been noted that in many of the systems studied the resulting signals possessed a large degree of unrelated harmonic content, serving only to complicate the theoretical interpretation.

With these deficiencies in mind the objectives of this work have been:

(i) to design a system capable of continuous operation at room temperature,

(ii) to improve the performance of the system by eliminating the unrelated harmonic content,

(iii) to carry out a thorough experimental evaluation of the system,

(iv) to develop a satisfactory and comprehensive theoretical formulation representative of the system, and

(v) to compare the experimental response with the theoretical formulation.

In achieving objectives (i) and (ii) special consideration was given to the design of the crystal holder and to the preparation of the CdS crystals themselves. Specifically, in achieving objection (ii) the alignment and polishing of the crystals were carried out under conditions of high precision and great care was taken to minimize any

inhomogeneity in either the Ohmic contacts to the crystal or the bulk conductivity. The relevant details of these considerations are given in conjunction with section 4-2 and Appendix I.

In relation to the remaining objectives the discussion of the text to follow is, hopefully, so structured to be of some pedagogical merit. The sequence of topics begins with the theoretical considerations. These are introduced by a novel development and discussion of the standard linear gain and dispersion conditions for a single travelling wave in a piezoelectric semiconductor. Adopting a linear phenomenological point of view the analysis is then extended to a multi-transit, reflecting wave system characteristic of an active acoustical cavity (a Phonon Maser). From such an analysis the threshold conditions for the onset of sustained acoustical oscillation are established and the tuning, conductivity, temperature, and electric field dependence of the threshold frequency are developed. A detailed design analysis of both shear and longitudinal maser structures is then carried out on the three piezoelectric semiconductors: ZnO, CdS, and CdSe.

To this point in the discussion the analysis is based upon a linear representation of a Phonon Maser. Subsequently a limited discussion of two of its non-linear features is then given, viz: the D.C. acoustoelectric current and

harmonic generation. Experimental data on the threshold response of a Phonon Maser are then presented and compared with the predictions of the linear, theoretical formulation. Specifically, the functional dependence of the threshold frequency and threshold drift velocity are analyzed in addition to the threshold frequency tuning response. In all cases outstanding agreement is obtained.

Conclusions are then drawn and areas of future investigation are outlined.

CHAPTER II

Phonon Maser Theory: Linear Analysis

2-1 Introduction

This chapter will be devoted to developing a theoretical model of a Phonon Maser based upon the acousto-electric interaction in piezoelectric semiconductors. In the discussion to be given all non-linear interactions have been neglected. Furthermore, the analysis is restricted to those frequencies for which $q\ell<1$, where q is the acoustical wave vector and ℓ is the thermal mean free path of the charge carriers. (For CdS this corresponds to an upper frequency of about 40 GHz at room temperature.) Within this limit we are justified in treating the medium as a continuum and in assuming local thermodynamic equilibrium.

Attention is given first to an analysis of piezo-electric insulators and then generalized to piezoelectric semiconductors. The results of this generalization are then used, in a phenomenological fashion, to formulate a model of a Phonon Maser.

2-2 Plane Wave Propagation in a Piezoelectric Semiconductor

The equations of state for a piezoelectric crystal follow rigorously from a thermodynamic analysis of anisotropic matter (Ny-60). The results of such an analysis are summarized in Fig. 2-1. Here all possible interactions between the mechanical, electrical, and thermal variables of the system are accounted for. The bold lines indicate those interactions which dominate, while the lighter lines identify those of secondary strength. The representative symbols are as defined under the List of Symbols and the bracketed numbers specify the rank of the corresponding tensor quantity.

In what is to follow all thermal contributions will be ignored. Thus, with the aid of Fig. 2-1 (noting the direction of the arrows) one can write down representative equations of state for any variable in terms of a mechanical and electrical contribution. The two equations of interest are:

$$T_{ij} = c_{ijk\ell}\, S_{k\ell} - \beta_{\ell ij}\, E_{\ell} \qquad (2\text{-}1)$$

$$D_k = 4\pi\beta_{k\ell m}\, S_{\ell m} + \varepsilon_{ki}\, E_i \qquad (2\text{-}2)^*$$

---

*The factor 4π comes from the use of c.g.s. units

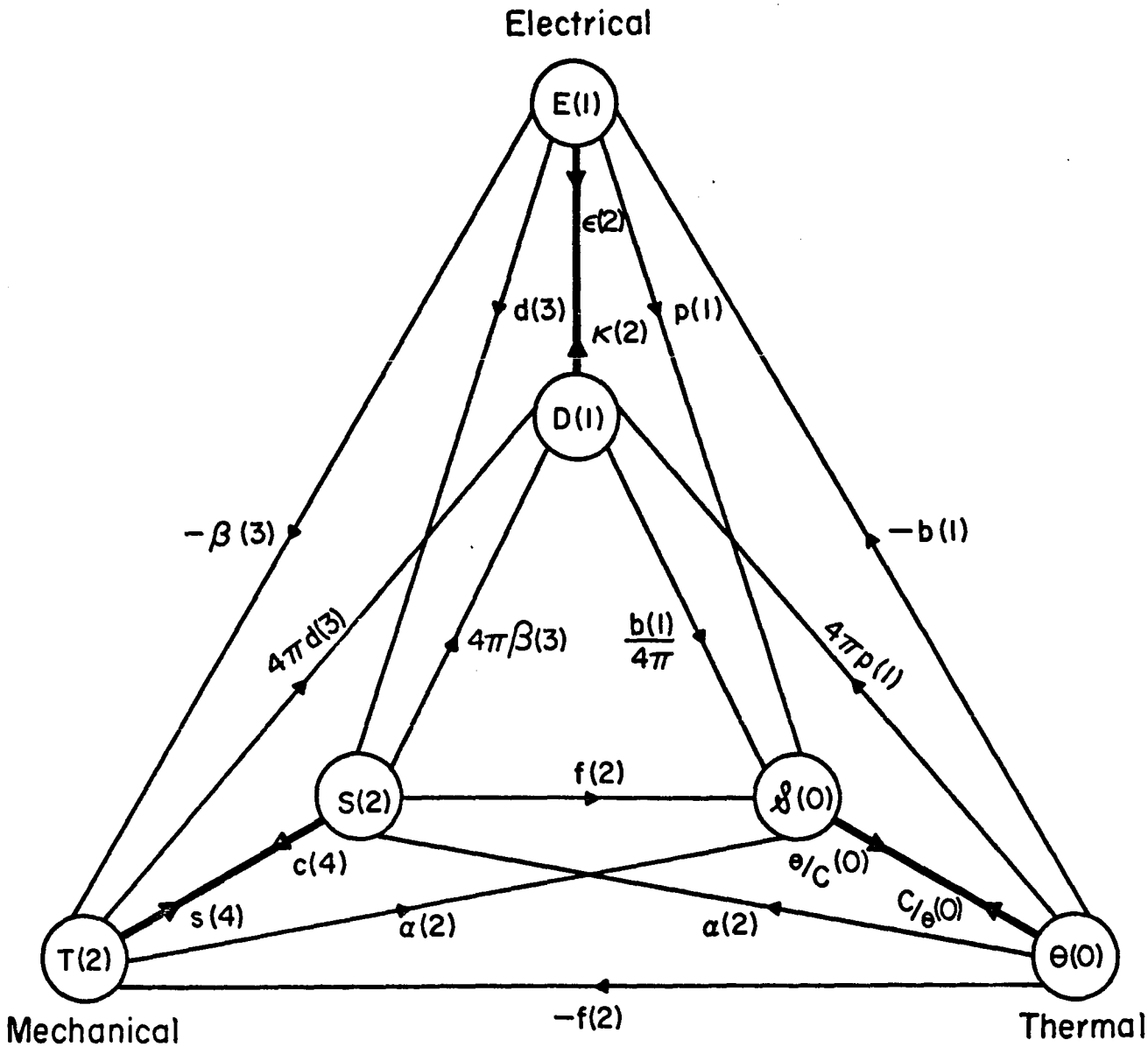

Fig. 2-1: Electrical, Mechanical and Thermal Interactions Within a Solid

Here, and in the text to follow, the adiabiatic value of the tensor components is assumed and the convention of summation over common indices is implied. In addition c.g.s. units are used throughout.

The format of these equations can be simplified somewhat by appealing to a standard convention of index contraction, viz: 11 → 1; 22 → 2; 33 → 3; 23 = 32 → 4; 31 = 13 → 5; and 12 = 21 → 6. In this way equations (2-1) and (2-2) reduce to the characteristic matrix form:

$$T_i = c_{ij} S_j - \beta_{\ell i} E_\ell \tag{2-3}$$

$$D_k = 4\pi\beta_{kj} S_j + \varepsilon_{ki} E_i \tag{2-4}$$

For the hexagonal, wurtzite (6 mm) class of crystals, of which CdS is a member, the constraints of symmetry further reduce the format of equations (2-3) and (2-4) to the following explicit form (where 3 refers to the c-axis):

$$\begin{bmatrix} T_1 \\ T_2 \\ T_3 \\ T_4 \\ T_5 \\ T_6 \\ \\ D_1 \\ D_2 \\ D_3 \end{bmatrix} = \begin{bmatrix} c_{11} & c_{12} & c_{13} & 0 & 0 & 0 & 0 & 0 & -\beta_{31} \\ c_{12} & c_{11} & c_{13} & 0 & 0 & 0 & 0 & 0 & -\beta_{31} \\ c_{13} & c_{13} & c_{33} & 0 & 0 & 0 & 0 & 0 & -\beta_{33} \\ 0 & 0 & 0 & c_{44} & 0 & 0 & 0 & -\beta_{15} & 0 \\ 0 & 0 & 0 & 0 & c_{44} & 0 & -\beta_{15} & 0 & 0 \\ 0 & 0 & 0 & 0 & 0 & c_{66} & 0 & 0 & 0 \\ \\ 0 & 0 & 0 & 0 & 4\pi\beta_{15} & 0 & \varepsilon_{11} & 0 & 0 \\ 0 & 0 & 0 & 4\pi\beta_{15} & 0 & 0 & 0 & \varepsilon_{11} & 0 \\ 4\pi\beta_{31} & 4\pi\beta_{31} & 4\pi\beta_{33} & 0 & 0 & 0 & 0 & 0 & \varepsilon_{33} \end{bmatrix} \begin{bmatrix} S_1 \\ S_2 \\ S_3 \\ S_4 \\ S_5 \\ S_6 \\ \\ E_1 \\ E_2 \\ E_3 \end{bmatrix}$$

(2-5)*

Attention now will be given to the equations of motion and the dispersion relationships for plane waves propagating along the threeorthogonal symmetry axis of a wurtzite crystal. In incorporating Maxwell's equations into this analysis we will invoke the quasi-static approximation: $\nabla X\vec{E} = o$. This action serves to decouple the acoustoelectric wave solutions (which travel at the velocity of sound, s) from the purely electromagnetic solutions (which travel at the velocity of light, c). And as has been shown by A.R. Hutson and D.L. White (Hu-62), the corresponding error introduced into the acoustoelectric dispersion relationships is only of the order of $s^2/c^2 \sim 10^{-10}$.

---

* The explicit value of the tensor components for CdS are given in Appendix I, with $c_{66} = \frac{1}{2}(c_{11} - c_{12})$

For each of the propagation directions there are three possible polarizations: two shear and one longitudinal. The resulting nine waves constitute the principal axis normal modes.

If, for the moment, we restrict our attention to insulating piezoelectrics, then from Poisson's equation, $\nabla \cdot \vec{D} = 0$, and equation (2-5) we are able to generate the following useful identities (realizing that, $\frac{\partial^2}{\partial x_i \partial x_j} = 0$, $i \neq j$ for plane waves).

$$\frac{\partial E_1}{\partial x_1} = - \frac{4\pi\beta_{15}}{\varepsilon_{11}} \frac{\partial^2 u_3}{\partial x_1^2} \tag{2-6}$$

$$\frac{\partial E_2}{\partial x_2} = - \frac{4\pi\beta_{15}}{\varepsilon_{11}} \frac{\partial^2 u_3}{\partial x_2^2} \tag{2-7}$$

$$\frac{\partial E_3}{\partial x_3} = - \frac{4\pi\beta_{33}}{\varepsilon_{33}} \frac{\partial^2 u_3}{\partial x_3^2} \tag{2-8}$$

Now from Newton's second law we have,

$$\rho \frac{\partial^2 u_i}{\partial t^2} = \frac{\partial T_{ji}}{\partial x_j} \tag{2-9}$$

which when coupled with equations (2-5) through (2-8) give the principal axis, normal mode wave equations, as tabulated by Table 2-1.

From Table 2-1 it can be seen that for most polarizations the velocity of sound is determined by the characteristic mechanical factors:

$$s_o^2 = c/\rho \tag{2-12}$$

However, for the three polarizations for which the displacement, u_i, is along the polar c-axis the velocity of sound is given by,

$$s^2 = s_o^2 \ (1+\chi) \tag{2-13}$$

where the parameter,

$$\chi = \frac{4\pi\beta^2}{\varepsilon c} \tag{2-14}$$

Table 2-1

Normal Mode Wave Equations

Polarization	Propagation Direction		
	$\vec{q}$ // to $\vec{x}_1 = \vec{a}$	$\vec{q}$ // to $\vec{x}_2 = \vec{b}$	$\vec{q}$ // to $\vec{x}_3 = \vec{c}$
Long	$\rho \frac{\partial^2 u_1}{\partial t^2} = c_{11} \frac{\partial^2 u_1}{\partial x_1^2}$	$\rho \frac{\partial^2 u_2}{\partial t^2} = c_{11} \frac{\partial^2 u_2}{\partial x_2^2}$	$\rho \frac{\partial^2 u_3}{\partial t^2} = c'_{33} \frac{\partial^2 u_3}{\partial x_3^2}$
Shear	$\rho \frac{\partial^2 u_2}{\partial t^2} = c_{66} \frac{\partial^2 u_2}{\partial x_1^2}$	$\rho \frac{\partial^2 u_3}{\partial t^2} = c'_{44} \frac{\partial^2 u_3}{\partial x_2^2}$	$\rho \frac{\partial^2 u_1}{\partial t^2} = c_{44} \frac{\partial^2 u_1}{\partial x_3^2}$
Shear	$\rho \frac{\partial^2 u_3}{\partial t^2} = c'_{44} \frac{\partial^2 u_3 c}{\partial x_1^2}$	$\rho \frac{\partial^2 u_1}{\partial t^2} = c_{66} \frac{\partial^2 u_1}{\partial x_2^2}$	$\rho \frac{\partial^2 u_2}{\partial t^2} = c_{44} \frac{\partial^2 u_2}{\partial x_3^2}$

$$c'_{44} = c_{44}\left[1 + \frac{4\pi\beta_{15}^2}{\varepsilon_{11}c_{44}}\right] \quad (2\text{-}10); \qquad c'_{33} = c_{33}\left[1 + \frac{4\pi\beta_{33}^2}{\varepsilon_{33}c_{33}}\right] \quad (2\text{-}11)$$

and is known as the piezoelectric coupling coefficient. It is to be noted from equations (2-6) through (2-8) that these three "piezoelectrically active" modes are also accompanied by a longitudinal electric field:

$$E = \frac{-4\pi\beta}{\epsilon} S \tag{2-15}$$

Indeed, it is the polarization induced by this longitudinal field that brings about a stiffening in the crystal lattice and the noted increase in the velocity of sound.

In making the transition to conducting piezoelectrics an additional longitudinal field is introduced via the non-zero source term of Poisson's equation:

$$\nabla \cdot \vec{D} = -4\pi en \tag{2-16}$$

This in turn influences the dispersion relationship for the active modes of the crystal. However, the dispersion relationships for the non-active modes, which are insensitive to longitudinal fields, remain unaffected. Thus, only the active modes are now of interest to us.

In analyzing the active modes of a piezoelectric semiconductor, the effects of equation (2-16) must be incor-

porated in a self consistent manner. This is achieved by the inclusion of Ohm's law and the continuity equation for electric charge. For plane wave motion along the x_i-axis (for which: $\frac{\partial}{\partial x_j} = 0$, $i \neq j$) we then obtain the following set of one dimensional equations.

$$\rho \frac{\partial^2 u}{\partial t^2} = c \frac{\partial^2 u}{\partial x^2} - \beta \frac{\partial E}{\partial x} \tag{2-17}$$

$$D = 4\pi\beta \frac{\partial u}{\partial x} + \varepsilon E \tag{2-18}$$

$$\frac{\partial D}{\partial x} = -4\pi e n \tag{2-19}$$

$$J = \mu e (n_o + n)(E - E_o) + \frac{1}{4\pi} \frac{\partial D}{\partial t} + \mu K T \frac{\partial n}{\partial x} \tag{2-20}$$

$$\frac{\partial J}{\partial x} = 0 \tag{2-21}$$

Here, u, is a generalized displacement representative of one of the active modes, with c, β, and ε chosen accordingly. In addition an extrinsic N-type semiconductor has been assumed with: n representing the variation in

charge density about the equilibrium value n_0; e the magnitude of electric charge; μ the electron drift mobility; K Boltzman's constant; and T the absolute temperature. Ohm's law, equation (2-20), has been generalized to accommodate diffusion currents and the presence of an externally applied D.C. field, E_0, directed in the negative x-direction (this accounts for the negative sign).

It will be noted that the complete set of equations is linear except for the product, nE, that appears in equation (2-20). In the analysis to follow this non-linear term will be ignored on the assumption that it is small in comparison to the linear terms. Combining equations (2-17) through (2-21) we are able to reduce the set of equations to the following coupled pair in u and n:

$$\frac{\partial^2 u}{\partial x^2} - \frac{1}{(1+\chi)s_o^2}\frac{\partial^2 u}{\partial t^2} = -\frac{e}{\beta}\frac{\chi}{1+\chi}n \qquad (2\text{-}22)$$

$$R^2\frac{\partial^2 n}{\partial x^2} - \tau v\frac{\partial n}{\partial x} - \tau\frac{\partial n}{\partial t} - n = \frac{\beta}{e}\frac{\partial^2 u}{\partial x^2} \qquad (2\text{-}23)$$

where,

$$\chi = \frac{4\pi\beta^2}{\varepsilon c} \qquad (2\text{-}24)$$

$$R^2 = \frac{\varepsilon KT}{4\pi n_o e^2} \tag{2-25}$$

$$\tau = \frac{\varepsilon}{4\pi\mu e n_o} \tag{2-26}$$

$$v = \mu E_o \tag{2-27}$$

and correspond, respectively, to the piezoelectric coupling coefficient, the Debye screening radius (squared), the dielectric relaxation time, and the electron drift velocity.

For the plane wave analysis under consideration we have,

$$u \rightarrow ue^{i(kx-\omega t)} \tag{2-28}$$

$$n \rightarrow ne^{i(kx-\omega t)} \tag{2-29}$$

which when substituted into equations (2-22) and (2-23), give:

$$\begin{bmatrix} k^2 - \frac{q_o^2}{1+\chi} & -\frac{e}{\beta}\frac{\chi}{1+\chi} \\ \frac{-k^2\beta}{e} & 1 + k^2R^2 - i\tau\omega(1-\frac{kv}{\omega}) \end{bmatrix} \begin{bmatrix} u \\ n \end{bmatrix} = 0 \qquad (2\text{-}30)$$

where, $q_o = \omega/s_o$.

The resulting secular determinant,

$$k^2 - \frac{1}{1+\chi}q_o^2 = \frac{k \quad (\chi/1+\chi)}{1 + k^2R^2 - i\tau\omega(1-kv/\omega)} \qquad (2\text{-}31)$$

gives a second order polynomial in k^2. To terms linear in χ we can approximate all values of k on the right of equation (2-31) by q_o, giving:

$$k^2 = q_o^2 \left[1 - \chi \frac{q_o^2 R^2(1+q_o^2R^2) + (\delta\tau\omega)^2 - i\gamma\tau\omega}{(1+q_o^2R^2)^2 + (\gamma\tau\omega)^2}\right] \qquad (2\text{-}32)$$

where,

$$\gamma = 1 - v/s_o \qquad (2\text{-}33)$$

Separating out real and imaginary parts according to,

$$k = \frac{\omega}{s} + i\Gamma \tag{2-34}$$

we get to terms linear in χ,

$$s = s_o \left[1 + \frac{\chi}{2} \frac{q_o^2 R^2 (1+q_o^2 R^2) + (\gamma\tau\omega)^2}{(1+q_o^2 R^2)^2 + (\gamma\tau\omega)^2} \right] \tag{2-35}$$

$$\Gamma = \frac{\chi\gamma\tau\omega q_o}{2 \left[(1+q_o^2 R^2)^2 + (\gamma\tau\omega)^2 \right]} \tag{2-36}$$

Equations (2-35) and (2-36) summarize the influence that free charge carriers have on the active modes of a piezoelectric semiconductor and compare directly with the corresponding equations reported by V.L. Gurevich (Gu-69) [aside from an error of ½ in his expression for Γ]. A comparison with the original work by D.L. White (Wh-62) is complicated, however, by the use of a different formulation and the use of M.K.S. units. The results are nevertheless equivalent. As noted, the influence of charge carriers brings about an attenuation in the wave in addition to velocity dispersion.

In each case the respective parameters are a function of: frequency, charge density, drift velocity, temperature, and D.C. electric field [as monitored by equations (2-24) - (2-27)].

The unique feature to note is that the attenuation coefficient, being linearly dependent on, $\gamma = 1 - v/s_o$, undergoes a change in sign when the drift velocity, v, exceeds the velocity of sound, s_o. The net result is a transformation from acoustical attenuation to acoustical gain. In short, when $v > s_o$ the drifting electrons are so phase matched with respect to the travelling acoustical wave that they expend energy on the wave in interacting with the piezoelectric field. This results in a transfer of momentum from the drifting electrons to the acoustical wave, and thus acoustical gain. For values of $v < s_o$ the phase match is such that momentum is transferred from the acoustical wave to the drifitng electrons, and thus acoustical attenuation. It is interesting to note, from equation (2-36), that Γ is symmetrical (aside from a change in sign) about the value, $\gamma = 0$.

From the functional form of equation (2-36) it follows that for fixed γ the frequency for which the gain or attenuation is maximized is given by:

$$\omega_o = \frac{s_o}{R} \qquad (2\text{-}37)$$

At this frequency the functional dependence of Γ takes the form,

$$\Gamma(\omega_o,\gamma) = \frac{\chi\gamma\omega_D\omega_o^2}{2s_o\,[4\omega_o^2 + \gamma^2\omega_D^2]} \tag{2-38}$$

where ω_D, the "diffusion frequency" is:

$$\omega_D = \frac{e s_o^2}{\mu K T} \tag{2-39}$$

Maximizing now equation (2-38) with respect to γ we obtain, for the respective drift velocities

$$v_E = s_o\left[1 \pm 2\ \frac{\omega_o}{\omega_D}\right] \tag{2-40}$$

the following extrema values of Γ:

$$\Gamma_E(\omega_o) = \pm\ \frac{\chi}{8s_o}\ \omega_o \tag{2-41}$$

Figure 2-2 illustrates the functional dependence of

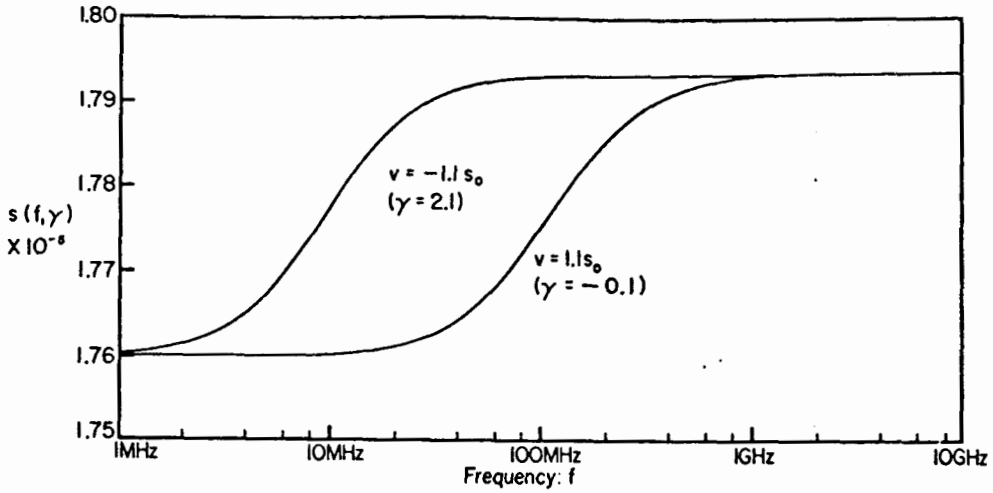

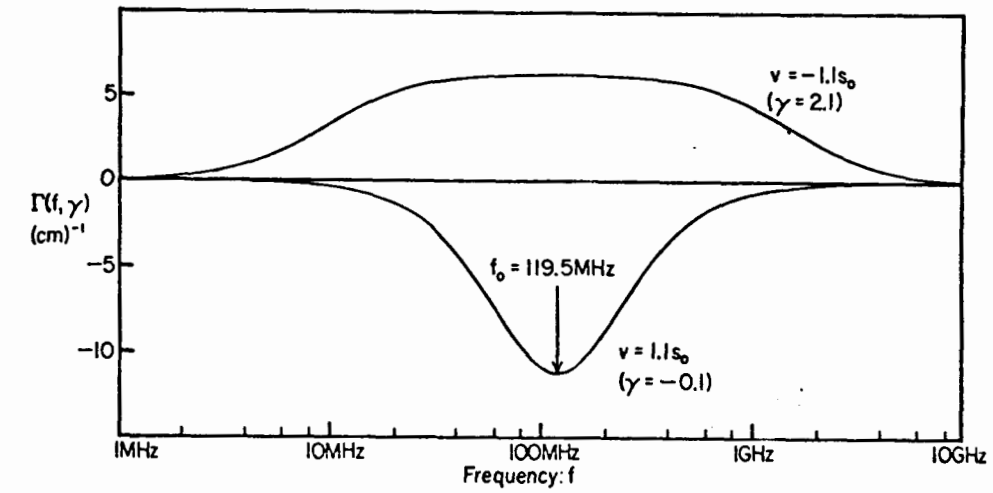

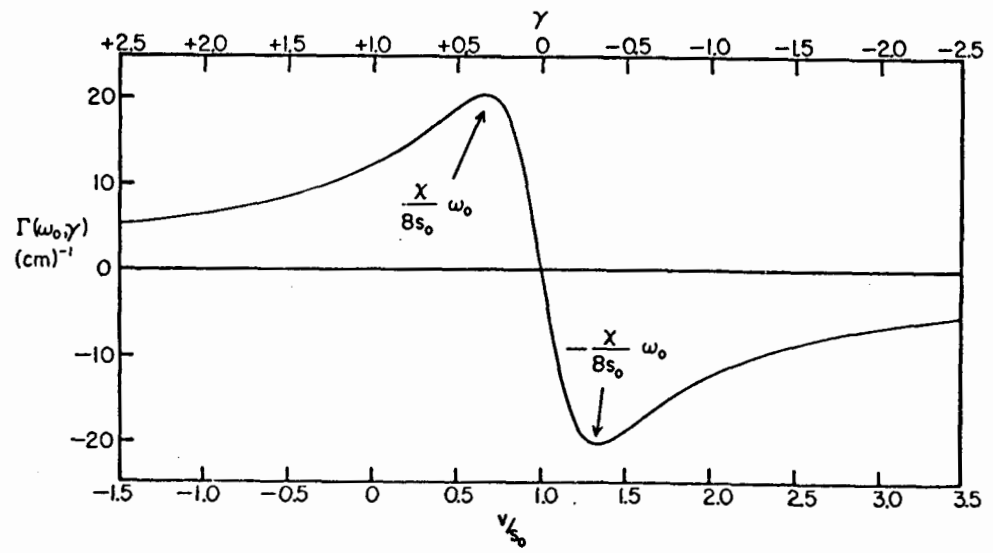

Fig. 2-2: Functional Dependence of $s(f,\gamma)$ and $\Gamma(f,\gamma)$ ($\sigma = 10^{-4}$ $(\Omega\text{-cm})^{-1}$, $\mu = 280$ $(cm^2/V\text{-sec})$, $T = 10°C$)

$\Gamma(\gamma,\omega)$ and $s(\gamma,\omega)$ for shear waves in CdS (characterized by a temperature of 10°C, a conductivity of 10^{-4} $(\Omega\text{-cm})^{-1}$, and a drift mobility of 280 $(cm^2/V\text{-sec})$. The respective values of γ chosen in the upper two figures correspond to two waves; one travelling parallel and the other antiparallel to a common electric field. From the center plot it is important to note that, for a band of frequencies around the frequency of maximum gain, the gain exceeds the attenuation. Thus, in spite of the fact that gain is achieved in only one direction, the system nevertheless possesses net round trip gain. This is a consequence of the asymmetry of the gain curve about $v = 0$ (as noted by the bottom plot). Without this necessarily unique feature piezoelectric semiconductors would not undergo phonon maser action.

2-3 Phenomenological Model of a Phonon Maser

The transition from an acoustical amplifier, as discussed in the previous section, to that of an acoustical oscillator corresponds to introducing regenerative acoustical feed back into the system. In practice this is achieved by structuring the active medium into a one dimensional cavity. The analysis then proceeds in a manner suggested by the following sketch.

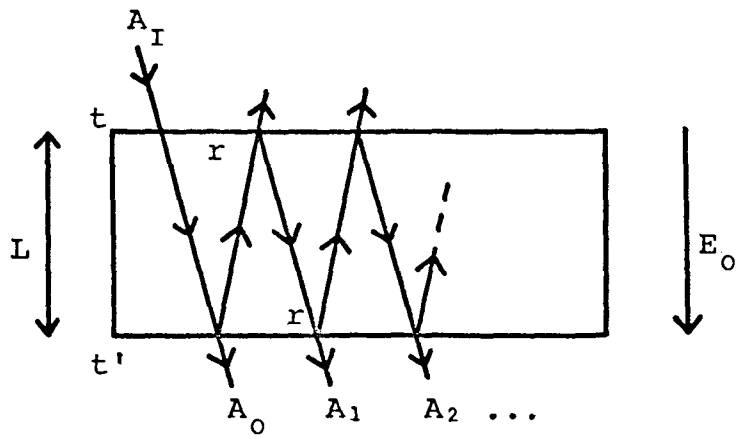

Here we consider an acoustical signal, A_I, normally incident upon a biased cavity of length, L, (the canted rays are for the purposes of diagramatic clarity only). At the boundaries the signal is subject to complex transmission and reflection coefficients t, t' and r. The resultant transmitted signal in then made up of the linear superposition:

$$A_T = \sum_{n=0}^{\infty} A_n \qquad (2\text{-}42)$$

Upon accounting for the relative phase change, the acoustoelectric and lattice attenuation, and the influence of the boundaries, equation (2-42) becomes,

$$A_T = A_I tt' e^{iq_+ L} e^{-(\Gamma_+ + \Gamma_L)L} \sum_{n=0}^{\infty} \left[r^2 e^{iqL} e^{-(\Gamma_N + 2\Gamma_L)L} \right]^n \qquad (2\text{-}43)$$

where

$$q = q_+ + q_- \tag{2-44}$$

$$\Gamma_N = \Gamma_+ + \Gamma_- \tag{2-45}$$

and Γ_L is the intrinsic lattice attenuation coefficient. The notation adopted here is: (+) designates those waves travelling parallel to the electric field, E_o (for which there is acoustical attenuation) and (-) designates those waves travelling antiparallel to the D.C. field (for which there is acoustical gain).

If we restrict our analysis to those values of drift field for which:

$$|r^2 e^{iqL} e^{-(\Gamma_N+2\Gamma_L)L}| \leq 1 \tag{2-46}$$

then equation (2-42) forms a simple harmonic series that converges to,

$$A_T = \frac{A_I tt' e^{iq_+L} e^{-(\Gamma_+ + \Gamma_L)L}}{1 - r^2 e^{iqL} e^{-(\Gamma_N+2\Gamma_L)L}} \tag{2-47}$$

Realizing that the source of the acoustical signal in a Phonon Maser is the thermal noise of the system and not some external signal, we define an "internal gain function",

$$Ge^{i\phi} = \frac{A_T}{A_I tt' e^{iq_+ L} e^{-(\Gamma_+ + \Gamma_L)L}} \tag{2-48}$$

corresponding to the feedback gain of the system. For the explicit complex structure of r,

$$r \to re^{i\theta} \tag{2-49}$$

(where θ is the phase change at the boundary) we obtain

$$G = \frac{1}{\left[1-2r^2 e^{-(\Gamma_N+2\Gamma_L)L}\cos(qL+2\theta) + r^4 e^{-2(\Gamma_N+2\Gamma_L)L}\right]^{\frac{1}{2}}} \tag{2-50}$$

and

$$\tan\phi = \frac{\sin(qL+2\theta)}{e^{(\Gamma_N+2\Gamma_L)L-2\ln r} - \cos(qL+2\theta)} \tag{2-51}$$

The transition now to an acoustical oscillator corresponds to: $G \to \infty$. From equation (2-50) this generates the following threshold condition for the onset of oscillation:

$$\cos(qL+2\theta) = \cosh[(\Gamma_N+2\Gamma_L)L - 2\ln r] \tag{2-52}$$

Realizing that $-1 \leq \cos\theta \leq 1$ and that $1 \leq \cosh\theta$ we are able to decouple equation (2-52) into the following two equations:

$$\Gamma_N(\omega,v) + 2\Gamma_L(\omega) - \frac{2\ln r}{L} = 0 \qquad (2\text{-}53)$$

$$\omega L\left(\frac{1}{s_+} + \frac{1}{s_-}\right) + 2\theta = 2\pi n \qquad (2\text{-}54)$$

Equations (2-53) and (2-54) form the basis of the analysis to follow and are essentially the same as those reported by V.L. Gurevich and B.D. Laikhtman (Gu-66).

If we attempt to substitute the threshold conditions into equation (2-51) we obtain an indeterminate result for tan ϕ. However, realizing that $\Gamma_N(\omega)$ and $\Gamma_L(\omega)$ are slowly varying functions of frequency in comparison to the trigonometric terms of equation (2-51) one can evaluate the indeterminate form, to a good approximation, by:

$$\phi \sim -(2n+1)\frac{\pi}{2} \qquad (2\text{-}55)$$

In contrast to the previous section, where only the one way attenuation coefficient was considered, we see that for the Phonon Maser the parameter of interest is the net round trip attenuation coefficient:

$$\Gamma_N = \frac{\chi\tau\omega q_o}{2}\left[\frac{\gamma_-}{(1+q_o^2R^2)^2+(\gamma_-\tau\omega)^2} + \frac{\gamma_+}{(1+q_o^2R^2)^2+(\gamma_+\tau\omega)^2}\right] \qquad (2\text{-}56)$$

where,

$$\gamma_- = 1 - v/s_o \qquad (2\text{-}57)$$

$$\gamma_+ = 1 + v/s_o \qquad (2\text{-}58)$$

As in the case of the one way coefficient, Γ, the net round trip coefficient, Γ_N, takes on an extrema value (for fixed γ) at,

$$\omega = \omega_o = \frac{s_o}{R} \qquad (2\text{-}59)$$

At this frequency equation (2-56) reduces to:

$$\Gamma_N(\omega_o, v) = \frac{\chi \omega_D \omega_o^2}{2 s_o} \left[\frac{\gamma_-}{4\omega_o^2 + \gamma_-^2 \omega_D^2} + \frac{\gamma_+}{4\omega_o^2 + \gamma_+^2 \omega_D^2} \right] \tag{2-60}$$

where once again ω_D is the "diffusion frequency" given by

$$\omega_D = \frac{e s_o^2}{\mu K T} \tag{2-61}$$

If we now seek the extrema values of equation (2-60) with respect to v, we obtain (for the root corresponding to the maximum net round trip gain) the expression:

$$\Gamma_N^{(M)}(\omega_o) = - \frac{\chi}{8 s_o} \left[\frac{\omega_o \omega_D}{2\omega_o + \sqrt{\omega_D^2 + 4\omega_o^2}} \right] \tag{2-62}$$

which occurs at a drift velocity given by:

$$v_M = s_o \left[1 + 4 \left(\frac{\omega_o}{\omega_D} \right)^2 + 4 \frac{\omega_o}{\omega_D} \sqrt{1 + 4 \left(\frac{\omega_o}{\omega_D} \right)^2} \right]^{\frac{1}{2}} \tag{2-63}$$

It will be noted from equation (2-62) that in the limit, $\omega_o \to \infty$, the maximum net round trip gain takes on the saturation

value:

$$\Gamma_N^{(M)}(\omega_o \to \infty) = -\frac{\chi}{32 s_o}\omega_D \qquad (2\text{-}64)$$

As will be discussed in section 2-4 this saturation limit restricts the maximum attainable operating frequency of the Phonon Maser.

Let us now return to a physical interpretation of the threshold conditions for spontaneous acoustical oscillation, as established by equations (2-53) and (2-54). The first of these is just a statement relating to the energy requirements for spontaneous oscillation, viz: that the net round trip gain, $\Gamma_N(\omega,v)$, be sufficient to overcome the internal, $2\Gamma_L(\omega)$, and end losses, $\frac{-2\ln r}{L}$, of the system. The second is the requirement that the threshold frequency be one of the normal modes of the cavity. It follows that the Phonon Maser will go into spontaneous acoustical oscillation at that normal mode of the system nearest the frequency of maximum gain. To elucidate this point let us look at the status of the system just below threshold.

For this we have chosen a shear wave system structured from CdS and characterized by a temperature of 10°C, a conductivity of 10^{-4} $(\Omega\text{-cm})^{-1}$, a drift mobility of 280 cm^2/V-sec, a thickness of 150 μ , a reflection coefficient of

0.918, and a drift velocity given by $v = 1.2\ s_o$. Fig. 2-3(a) is the resulting frequency plot of the total attenuation coefficient.

$$\Gamma_T(\omega,v) = \Gamma_N(\omega,v) + 2\Gamma_L(\omega) \qquad (2\text{-}65)$$

The dashed line corresponds to the end loss term, $\frac{2\ln r}{L}$, and is taken as frequency independent. Since the net gain, at all frequencies, is less than the end losses encountered the system remains subcritical with respect to spontaneous oscillation.

In evaluating Fig. 2-3(a) an empirical lattice loss term of the form,

$$\Gamma_L = \alpha\omega^{\beta} \qquad (2\text{-}66)$$

has been employed, with: $\alpha = 1.11 \times 10^{-14}$ and $\beta = 1.51$, for shear modes (Ma-69). The net influence of Γ_L on the total round trip attenuation profile is to intensify the attenuation at the high frequency end and to lower the frequency of maximum gain from, ω_o to:

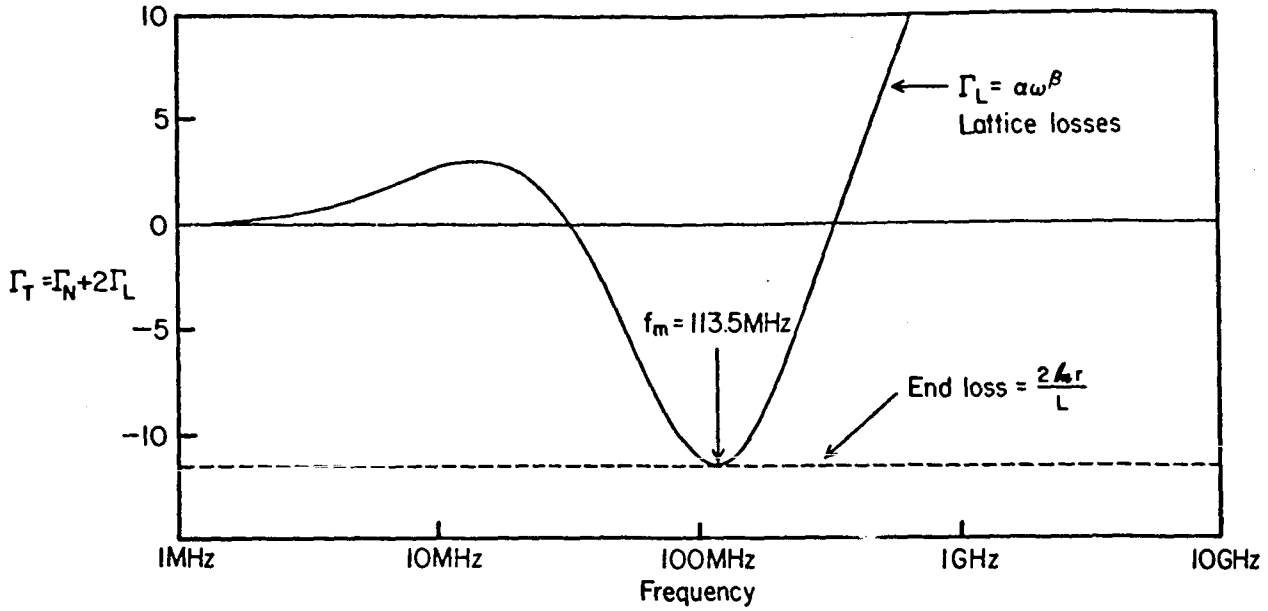

Fig. 2-3(a): Total Attenuation Coefficient Versus Frequency

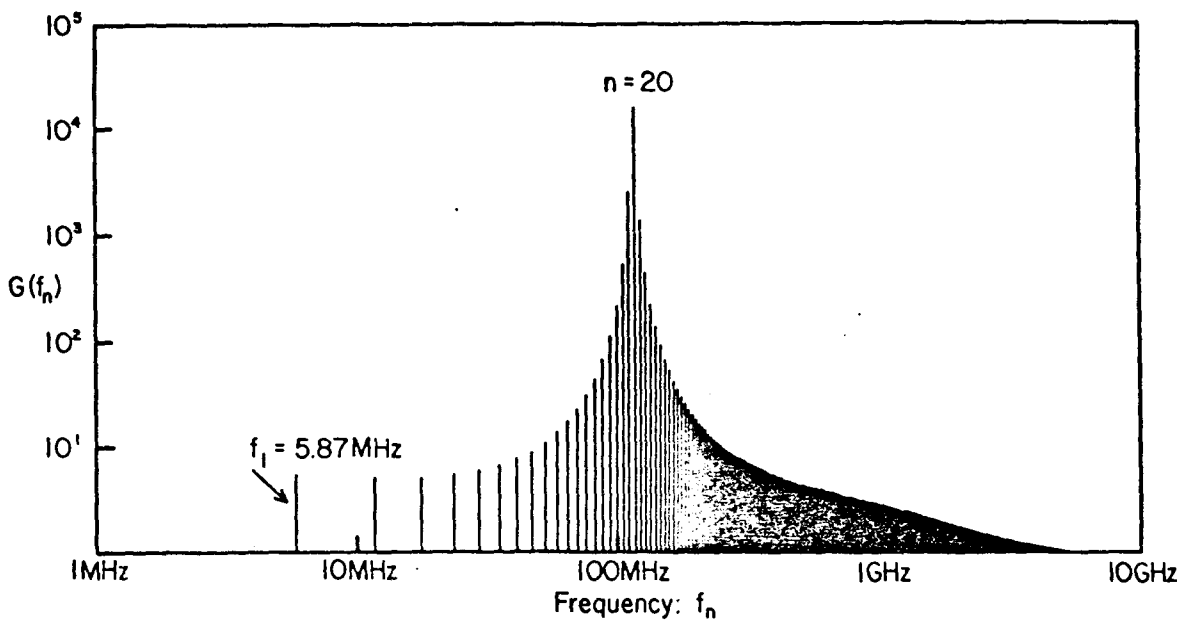

Fig. 2-3(b): Normal Mode Round Trip Gain

$$\omega_m = \omega_o(1+\delta) \tag{2-67}$$

A first order approximation of the correction factor can be obtained by solving, to terms linear in δ, the equation:

$$\frac{\partial \Gamma_T}{\partial \omega}\Big|_{\omega_m} = 0 \tag{2-68}$$

Such an analysis gives:

$$\delta_1(\omega_o, v) = \left[\frac{2\chi\omega_D\omega_o{}^{4-\beta}}{\alpha\beta s_o} \left(\frac{\gamma_-}{[4\omega_o^2+\gamma_-^2\omega_D^2]^2} + \frac{\gamma_+}{[4\omega_o^2+\gamma_+^2\omega_D^2]^2} \right) - (\beta-1) \right]^{-1} \tag{2-69}$$

where: γ_-, γ_+, ω_o, and ω_D are given by equations (2-57), (2-58), (2-59) and (2-61) respectively.

Fig. 2-3(b) is a logarithmic histogram plot of the feedback gain function $G(f_n)$, evaluated at the normal modes of the system. As illustrated, the principal effect (introduced by virtue of acoustical feedback) is the transformation from a system possessing very poor frequency discrimination,

as indicated by the broad minimum of Fig. 2-3(a), to one possessing a very high degree of spectral resolution. Thus in spite of the dense mode spacing only one mode, namely the one nearest the frequency of maximum gain, ω_m, breaks into spontaneous oscillation once the drift velocity is increased to its threshold value: v_{th}.

The drift velocity dependence of, $\Gamma_T(\omega_{max},v)$, is illustrated by Fig. 2-4(a) for both the corrected and uncorrected frequency of maximum gain (i.e. $\omega_{max} = \omega_m$; $\omega_{max} = \omega_o$). Fig. 2-4(b) gives the corresponding dependence of the frequency correction factor, $\delta(v)$, that appears in equation (2-67). As indicated by Fig. 2-4(a) not only is there a threshold drift velocity, v_{th}, but also a cut-off value, v_{co}, above which oscillation should cease.

It will be noted from Fig. 2-4(b) that, $\delta_1(v)$, as given by equation (2-69), is a good approximation to δ for values of the drift velocity near v_{th}. It will also be noted from Fig. 2-4(a) that $\Gamma_T(\omega_{max},v)$ is markedly insensitive to δ. As a consequence we are able to derive a reasonable analytical expression for v_{th}, by forming a Taylor expansion of $\Gamma_T(\omega_o,v)$ about $v = s_o$, keeping only the linear terms, and solving for the corresponding intercept with the end loss term, $\frac{2\ln r}{L}$. Upon appealing to equations (2-60) and (2-66) we obtain the result:

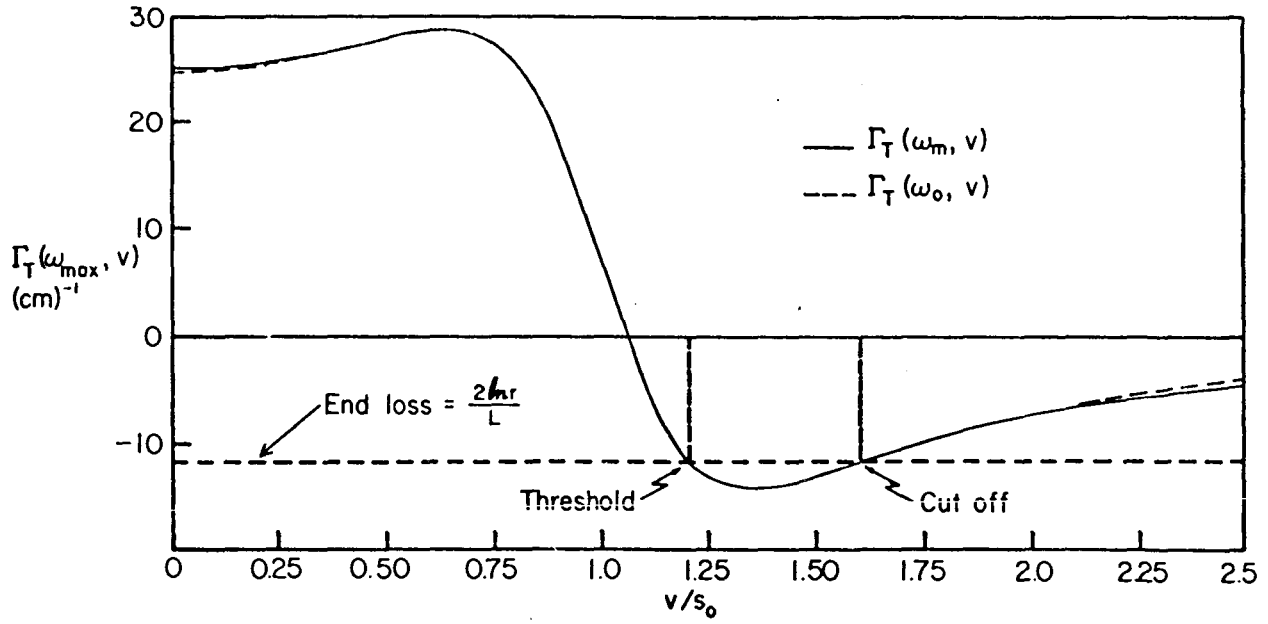

Fig. 2-4(a): Maximized Total Attenuation Versus Drift Velocity

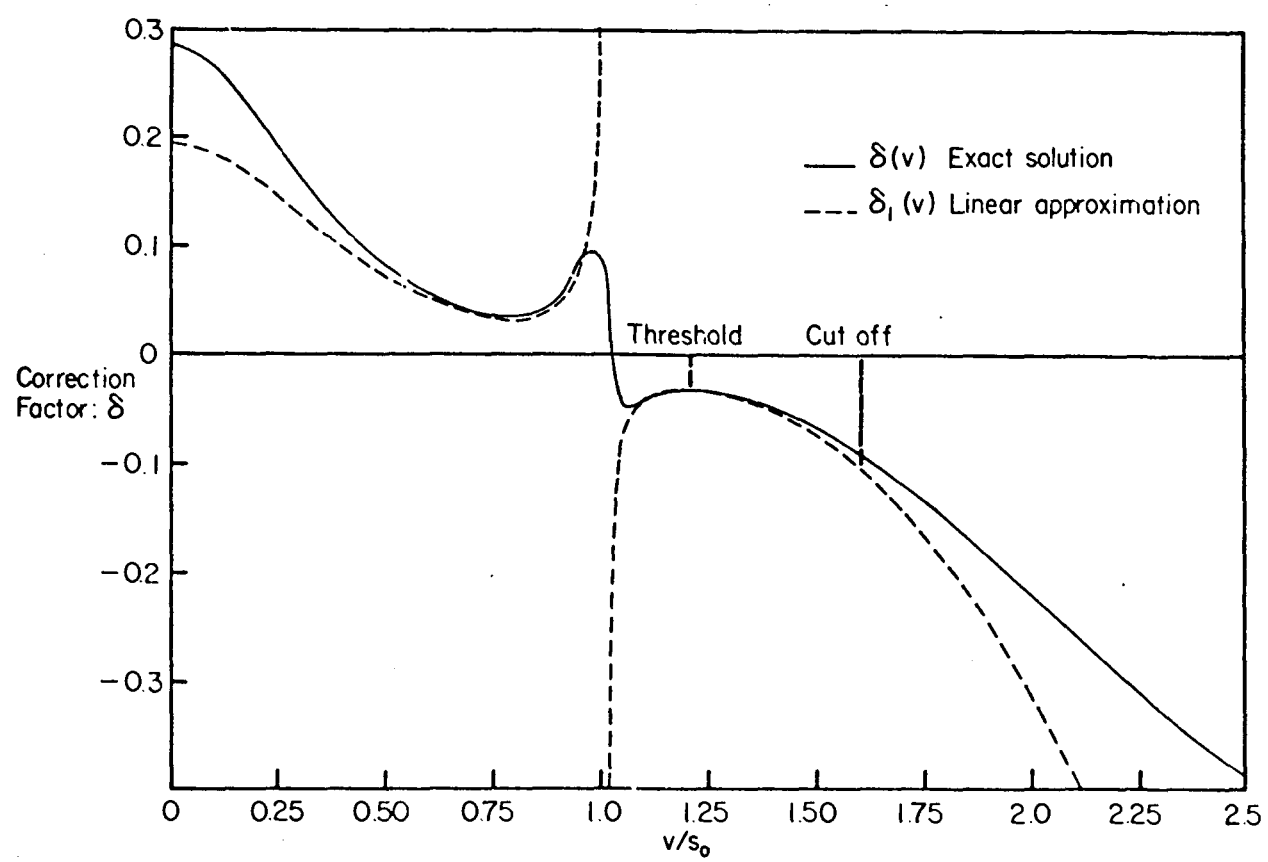

Fig. 2-4(b): Threshold Frequency Correction Factor Versus Drift Velocity

$$v_{th} = s_o \left[1 + \frac{2(\omega_o^4+\omega_o^2\omega_D^2)}{3\omega_o^2\omega_D^2+\omega_D^4} + \frac{16 s_o}{\chi\omega_D} \frac{(\omega_o^2+\omega_D^2)^2}{3\omega_o^2\omega_D^2+\omega_D^4} \left(\alpha\omega_o^\beta - \frac{\ln r}{L}\right) \right] \qquad (2\text{-}70)$$

2-4 Design Analysis of a Phonon Maser

In the design analysis of a Phonon Maser the parameters of interest are:

(i) the operating band width

(ii) the D.C. power dissipation, and

(iii) the conductivity and drift field requirements.

Each of these parameters will now be investigated for both shear and longitudinal modes of maser action in ZnO, CdS, and CdSe. Throughout this analysis the operating (threshold) frequency, ω_m, will be approximated by ω_o.

In establishing the upper and lower frequency limits of the operating band width we seek the roots of the maximized threshold equation:

$$\Gamma_N^{(M)}(\omega_o) + 2\alpha\omega_o^\beta - 2\frac{\ln r}{L} = 0 \qquad (2\text{-}71)$$

For the upper frequency limit we obtain, to a good approximation:

$$\omega_u \simeq \left[\frac{\chi\omega_D}{64\alpha s_o} + \frac{\ln r}{\alpha L}\right]^{1/\beta} \qquad (2\text{-}72)$$

where we have made the substitution:

$$\Gamma_N^{(M)}(\omega_u) \rightarrow \Gamma_N^{M}(\infty) = -\frac{\chi}{32 s_o}\omega_D \qquad (2\text{-}73)$$

For the lower frequency limit we obtain, to a good approximation:

$$\omega_L \simeq \frac{\omega_D}{2}\left[\left(1 + \frac{\chi\omega_D L}{32 s_o \ln r}\right)^2 - 1\right]^{-\frac{1}{2}} \qquad (2\text{-}74)$$

where we have utilized equation (2-62) and have ignored the lattice loss term, $2\alpha\omega_o^{\beta}$.

In evaluating the D.C. power dissipation per unit volume, at threshold, we make use of Ohm's law and the threshold field conditions,

$$\mu E_{th} = v_{th} \qquad (2\text{-}75)$$

The resulting equation is;

$$P/V = \frac{n_o e}{\mu} v_{th}^2 \tag{2-76}$$

Upon employing the results of equations (2-25) and (2-70), equation (2-76) takes the following explicit form:

$$P/V = \frac{\varepsilon KT}{4\pi e\mu}\,\omega_o^2 \left[1 + \frac{2(\omega_o^4+\omega_o^2\omega_D^2)}{3\omega_o^2\omega_D^2+\omega_D^4} + \frac{16 s_o}{\chi\omega_D} \frac{(\omega_o^2+\omega_D^2)^2}{3\omega_o^2\omega_D^2+\omega_D^4} \left(\alpha\omega_o^{\beta} - \frac{\ln r}{L} \right) \right]^2 \tag{2-77}$$

The heat generated by the D.C. power dissipation within the crystal imposes an additional constraint on the system. Namely, a temperature profile is set up within the crystal in accordance with the thermal properties of the material and its associated heat sink. The toleration of a given temperature differential implies a maximum allowable power dissipation, and thus a thermally limited upper frequency.

For the thermal aspects of the design analysis we will consider the Phonon Maser to have adiabatic edges and to be in contact with an infinite heat sink at each face. Upon solving the steady state diffusion equation with a homogenous source term Q (Power/unit volume) one obtains a

solution corresponding to a parabolic temperature profile across the crystal, with a maximum temperature differential given by:

$$\Delta T = \frac{QL^2}{8\kappa} \qquad (2\text{-}78)$$

where L is the thickness of the crystal and κ the corresponding thermal conductance.

From equation (2-78) we are able to calculate, for a given temperature differential ΔT, the corresponding power dissipation per unit volume, Q. Upon equating this with equation (2-77) we are able to determine the corresponding thermally limited frequency, $f_u(\Delta T)$.

With the aid of equations (2-62), (2-64), (2-66), (2-70), (2-72), (2-74), (2-77) and (2-78) a design analysis has been carried out on the three materials: ZnO, CdS and CdSe. The relative material parameters are given in Table 2-2. Table 2-3 gives values for the corresponding principal maser parameters while Figures (2-5) through (2-10) give the detailed frequency dependence of the various functions.

If one takes the point of view that the most desired feature is a wide operating range, then the thermally limited band width (for a given temperature differential) serves as a good figure of merit in evaluating the various systems.

Table 2-2

Material Parameters†

X'tal	Mode	χ	s_o	ε	μ	κ	α	β
			$\times 10^5$ cm/sec		$\frac{cm^2}{V\text{-}sec}$	$\frac{watts}{cm\text{-}°C}$	$\frac{(sec)^\beta}{cm}$	
ZnO	long	0.152	6.10	11.7	150	0.025	5.03×10^{-20}	1.989
		(Ne-69)	(Hi-69)	(Ko-64)	(Ne-69)	(In-29)	(Ma-50)	(Ma-50)
ZnO	shear	0.0567	2.74	8.1	150	0.025	4.61×10^{-16}	1.566
		(Ne-69)	(Hi-69)	(Ko-64)	(Ne-69)	(In-29)	(Ma-50)	(Ma-50)
CdS	long	0.0296	4.41	9.53	280	0.2	1.11×10^{-14}	1.51
		(MC-69)	(MC-69)	(MC-69)	(Ne-69)	(Ne-69)	(*)	(*)
CdS	shear	0.0378	1.76	9.02	280	0.2	1.11×10^{-14}	1.51
		(MC-69)	(MC-69)	(MC-69)	(Ne-69)	(Ne-69)	(Ma-69)	(Ma-69)
CdSe	long	0.0160	3.85	10.20	600	0.063	1.11×10^{-14}	1.51
		(MC-69)	(MC-69)	(MC-69)	(Ne-69)	(Ne-69)	(*)	(*)
CdSe	shear	0.0176	1.52	9.33	600	0.063	1.11×10^{-14}	1.51
		(MC-69)	(MC-69)	(MC-69)	(Ne-69)	(Ne-69)	(*)	(*)

† Throughout we have used: T = 10°C, r = 0.96, L = 300μ.

* For lack of published data; taken the same as CdS - shear.

Table 2-3

Phonon Maser Parameters

X'tal	Mode	$-\Gamma_N^{(M)}(\infty)$	f_D	f_L	f_u/B.W.	$f_u(1)$/B.W.	$f_u(5)$/B.W.	$f_u(10)$/B.W.
		cm^{-1}	GHz	MHz	GHz/GHz	MHz/MHz	MHz/MHz	MHz/MHz
ZnO	long	792	16.2	13.9	16.2	180	404	571
					16.2	166	390	557
ZnO	shear	133	3.27	16.9	14.2	219	472	643
					14.2	202	455	626
CdS	long	59.7	4.53	52.8	2.45	710	1366	1788
					2.40	657	1313	1735
CdS	shear	30.4	0.722	16.9	1.58	490	809	943
					1.56	473	792	926
CdSe	long	13.2	1.61	93.6	0.829	481	-	-
					0.735	387	-	-
CdSe	shear	5.71	0.251	41.4	0.362	278	-	-
					0.321	237	-	-

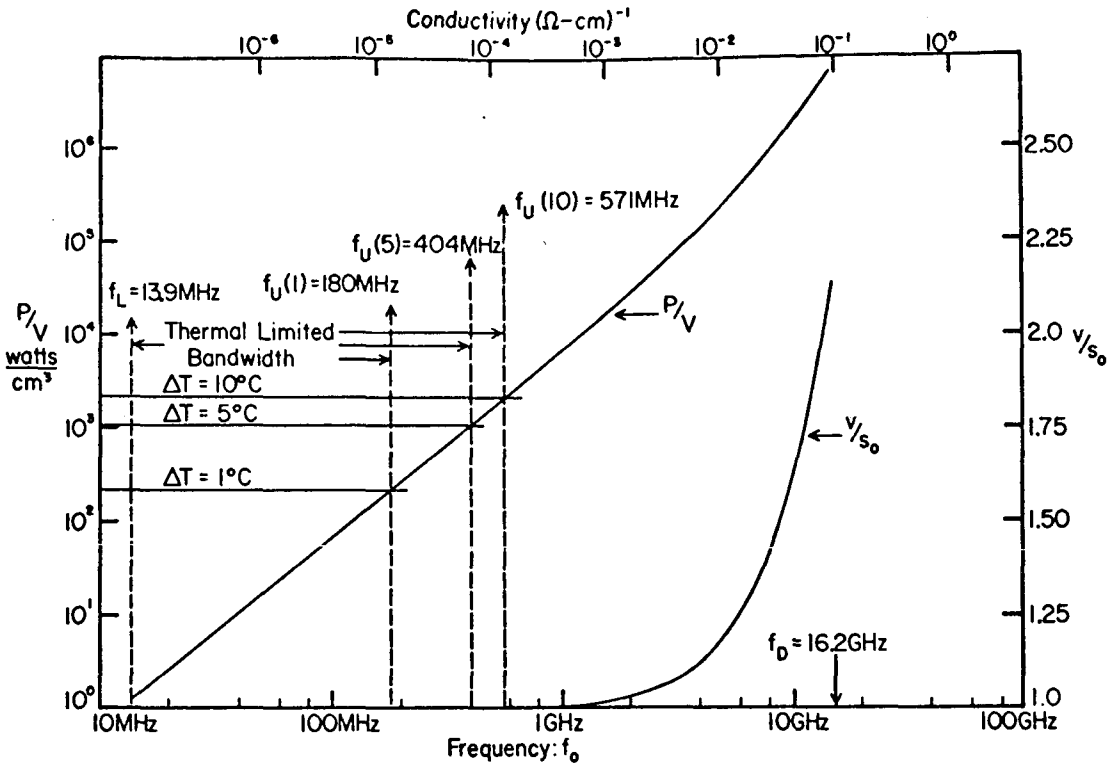

Fig. 2-5(a): ZnO-Long; Threshold Power & Drift Velocity

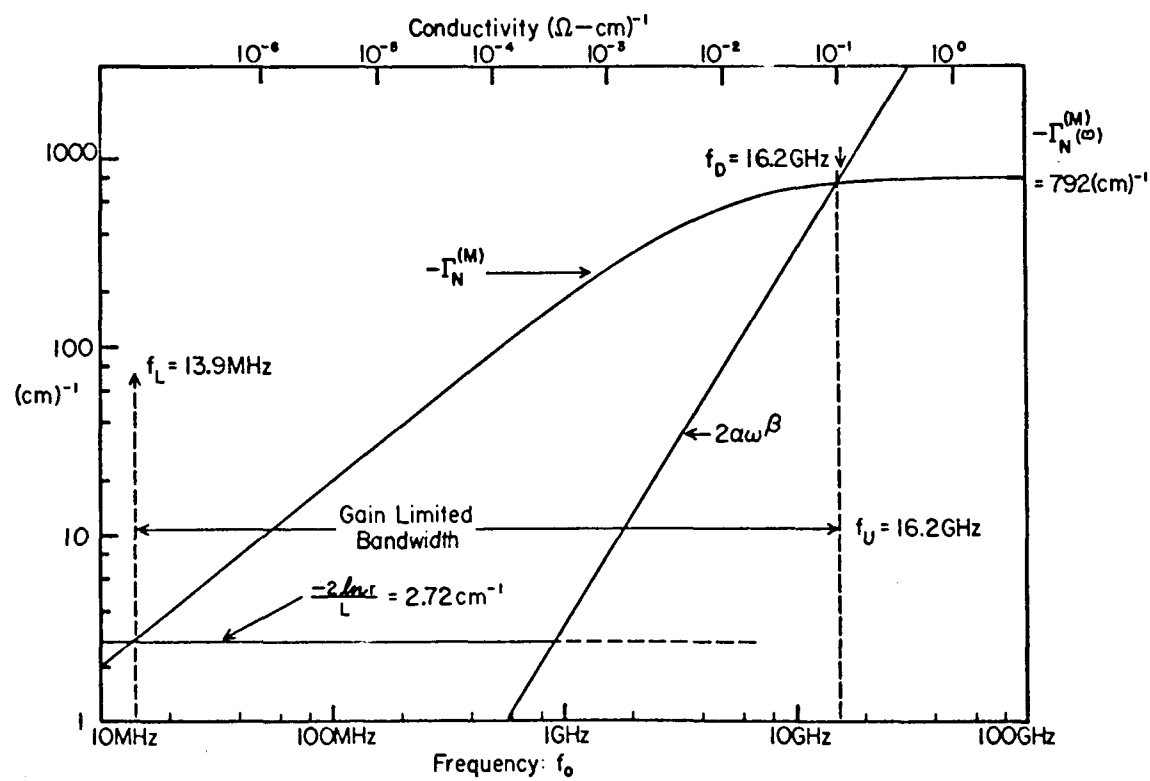

Fig. 2-5(b): ZnO-Long; Maximized Gain Response

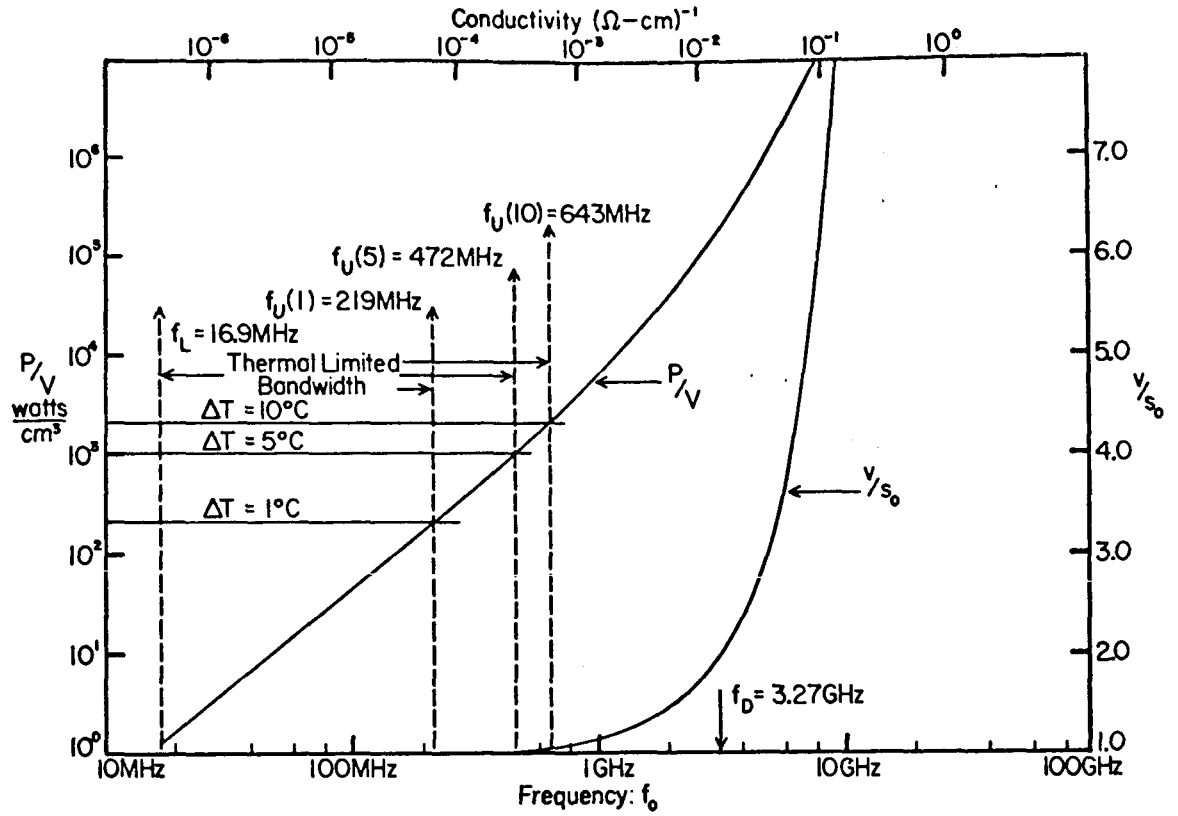

Fig. 2-6(a): ZnO-Shear; Threshold Power & Drift Velocity

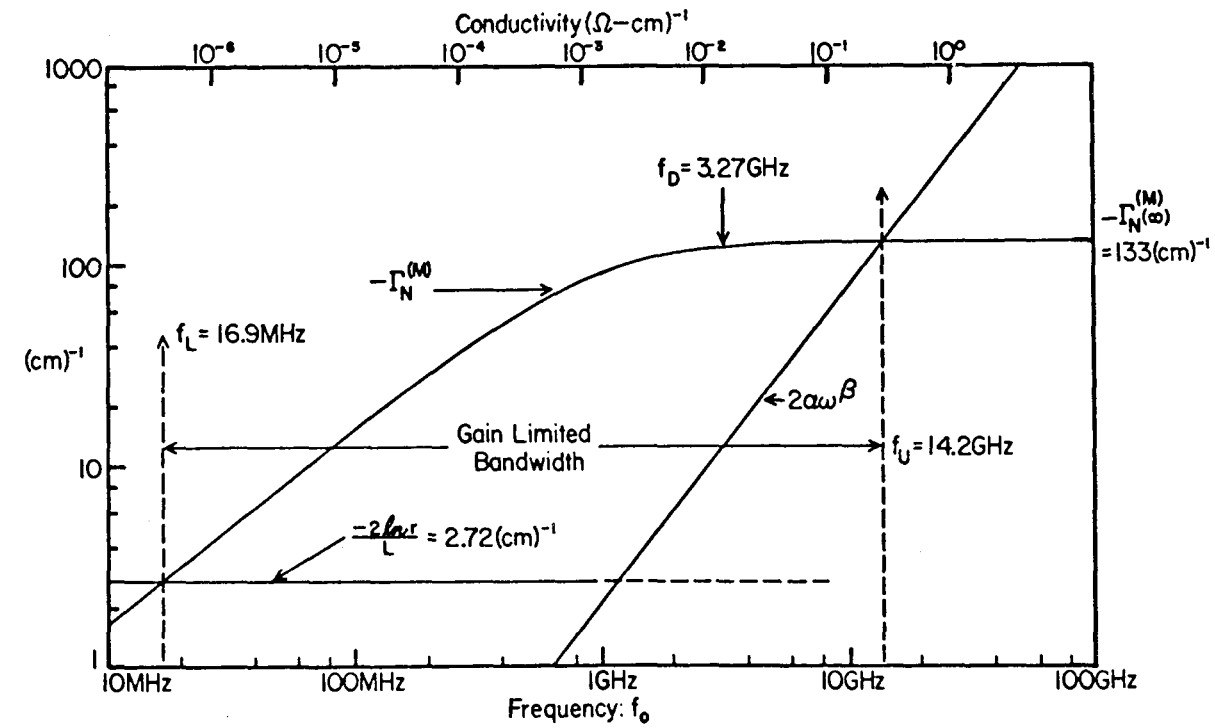

Fig. 2-6(b): ZnO-Shear; Maximized Gain Response

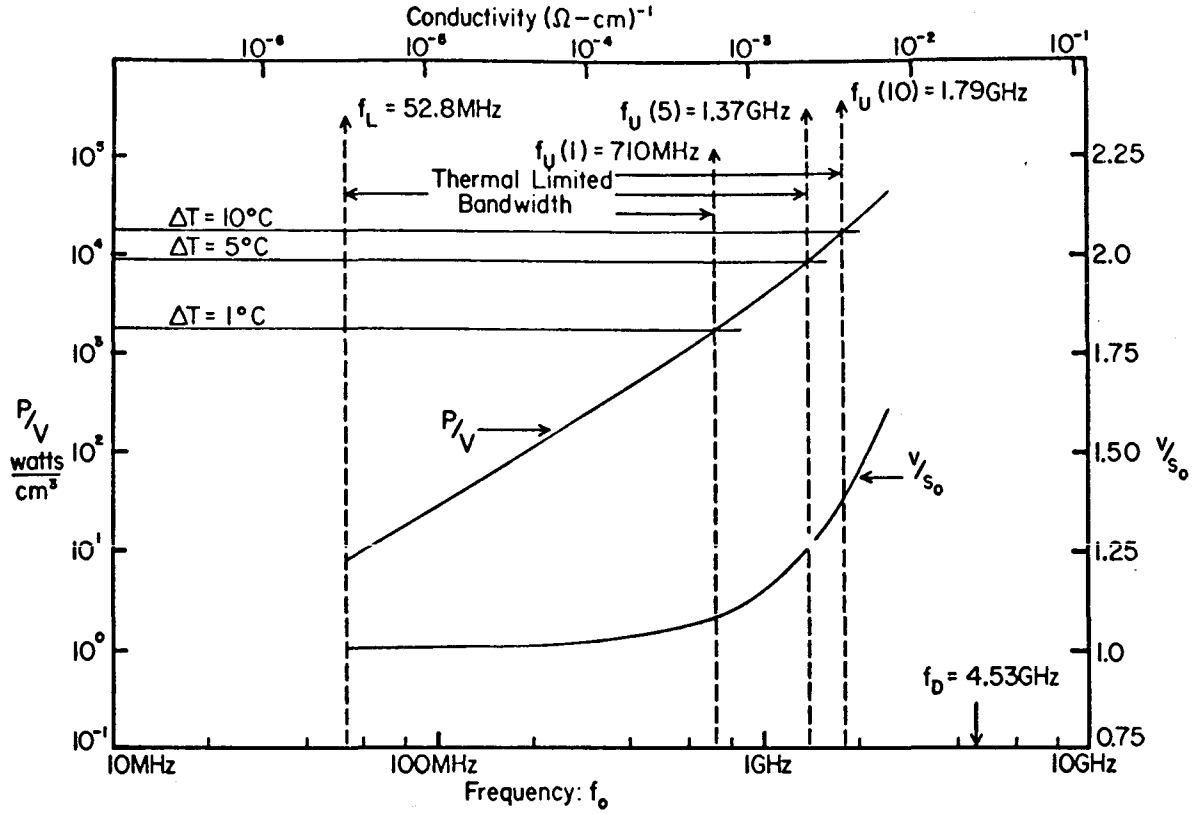

Fig. 2-7(a): CdS-Long; Threshold Power & Drift Velocity

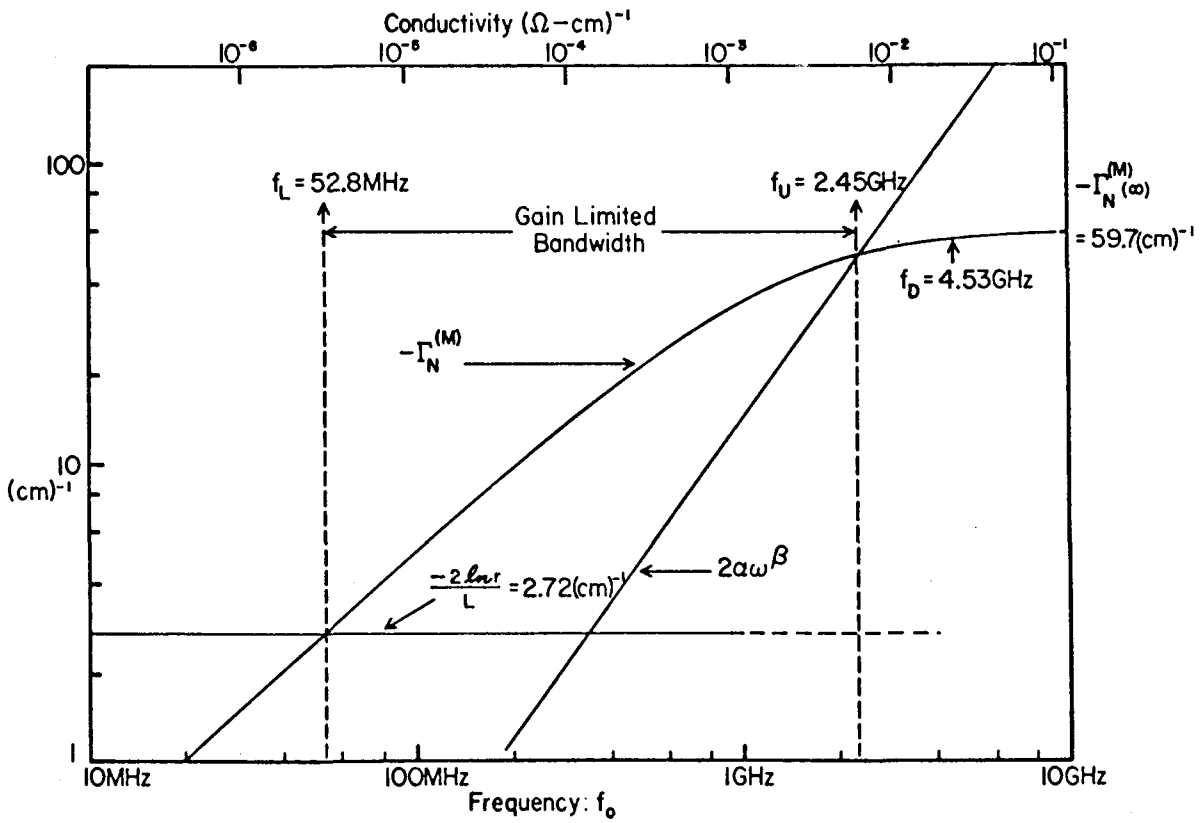

Fig. 2-7(b): CdS-Long; Maximized Gain Response

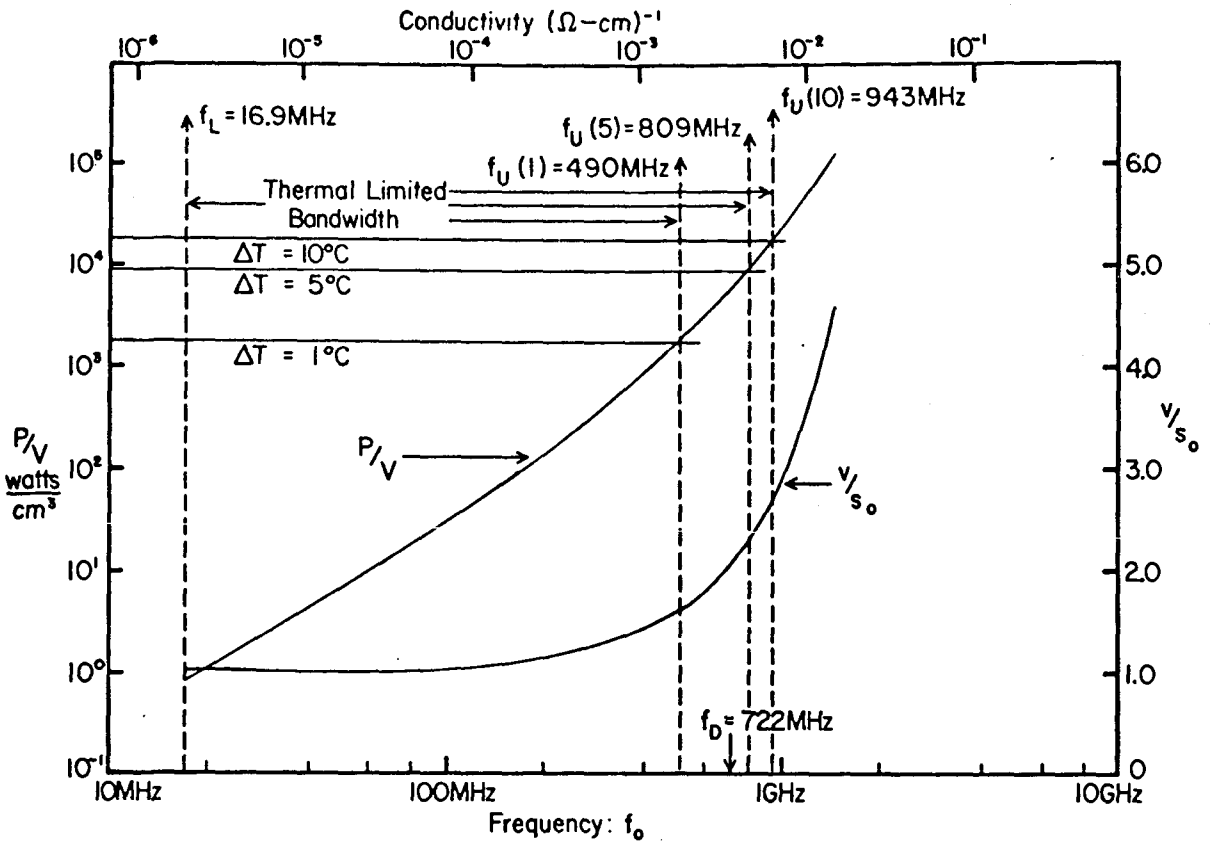

Fig. 2-8(a): CdS-Shear; Threshold Power & Drift Velocity

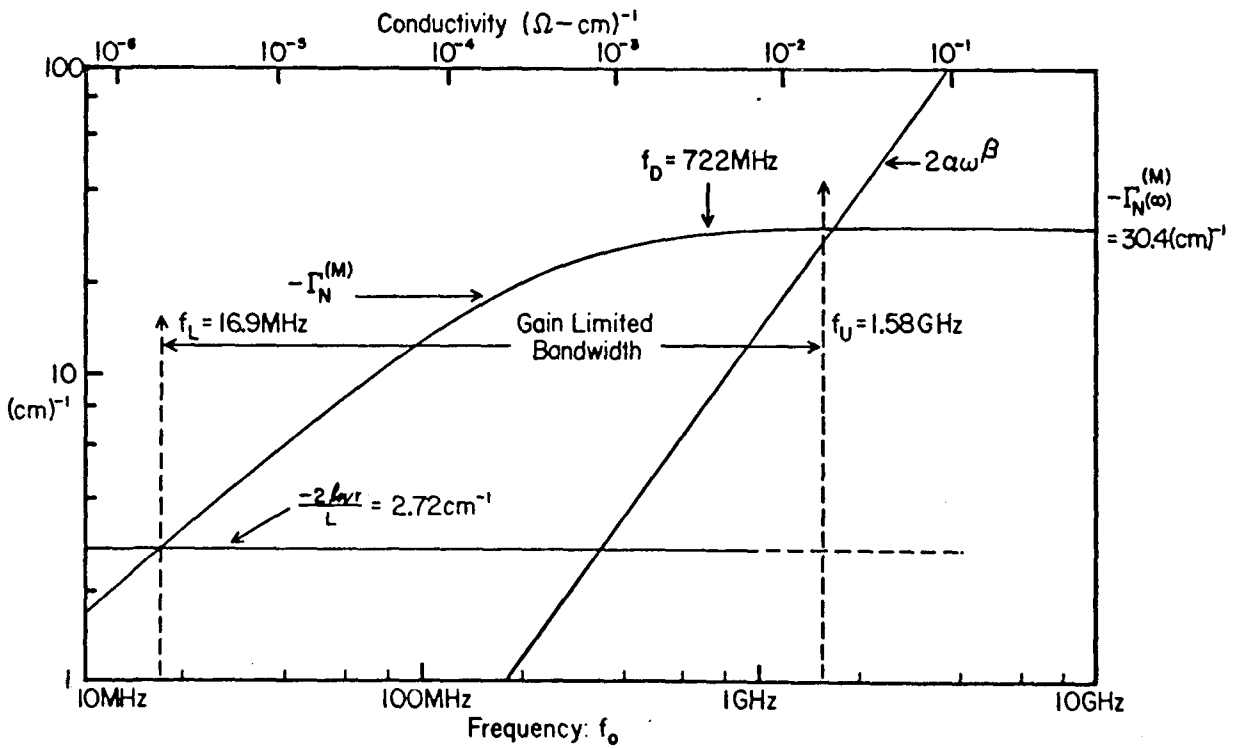

Fig. 2-8(b): CdS-Shear; Maximized Gain Response

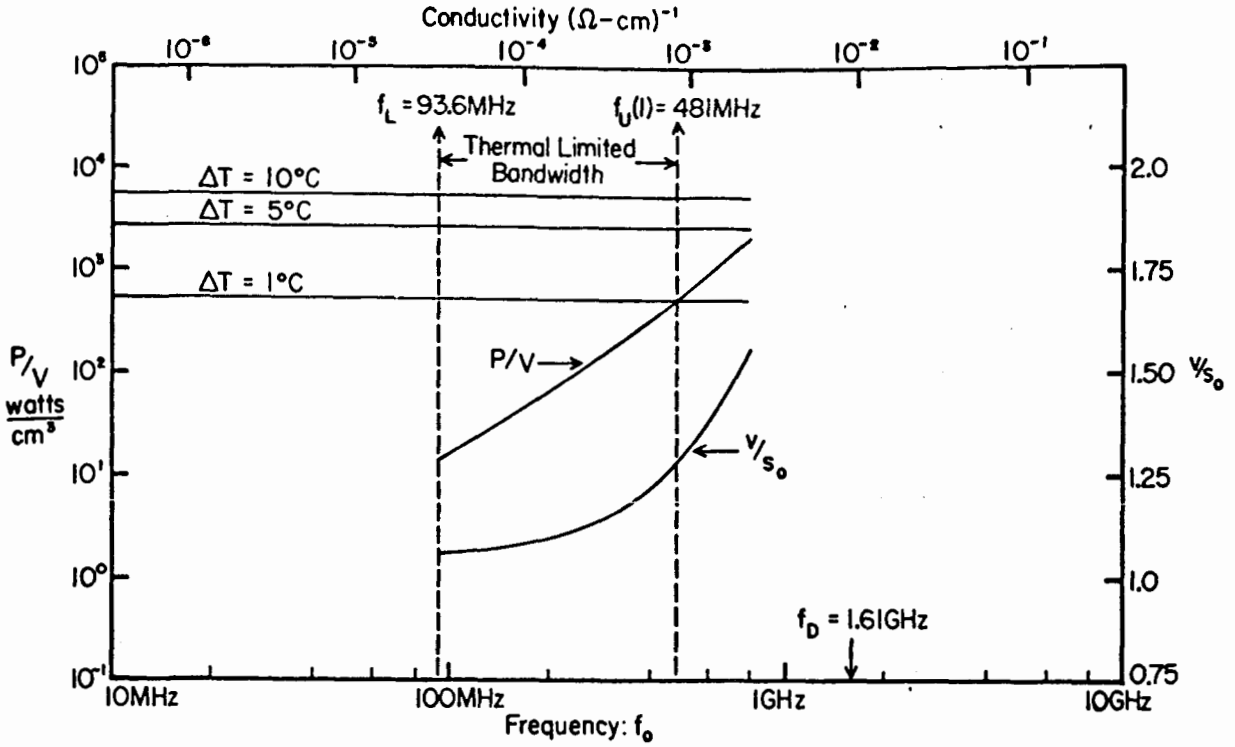

Fig. 2-9(a): CdSe-Long; Threshold Power & Drift Velocity

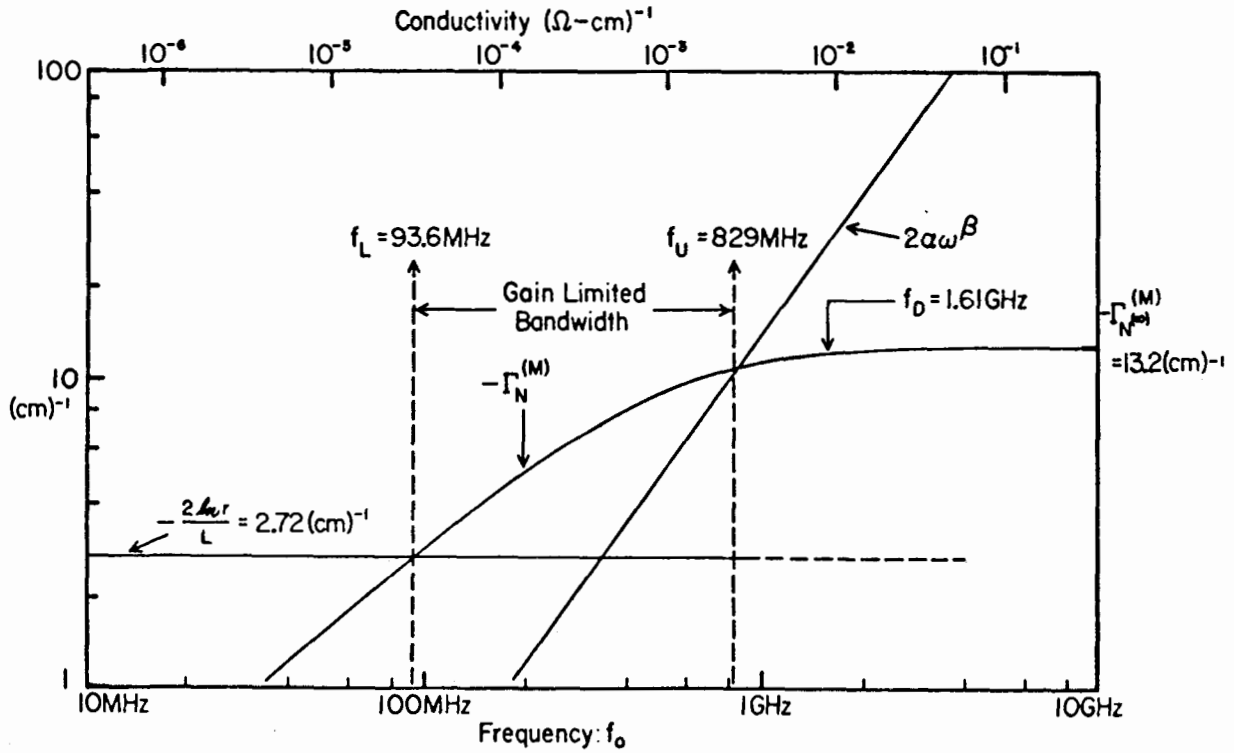

Fig. 2-9(b): CdSe-Long; Maximized Gain Response

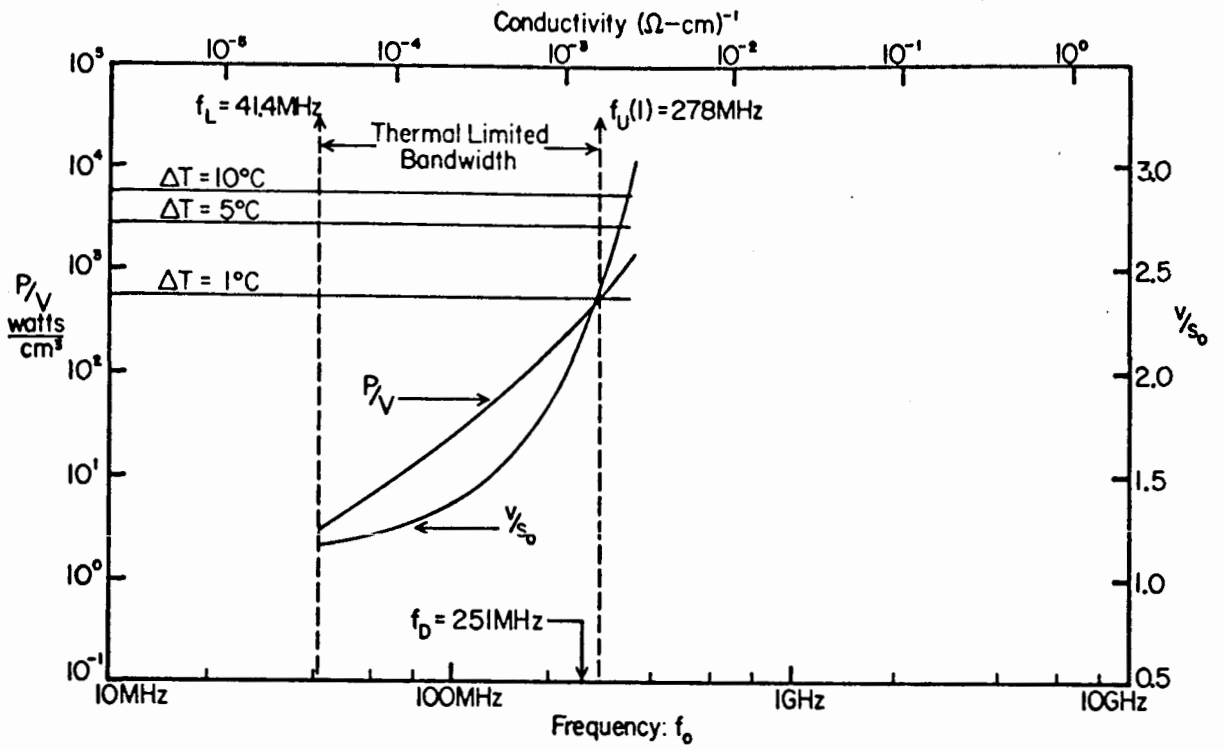

Fig. 2-10(a): CdSe-Shear; Threshold Power & Drift Velocity

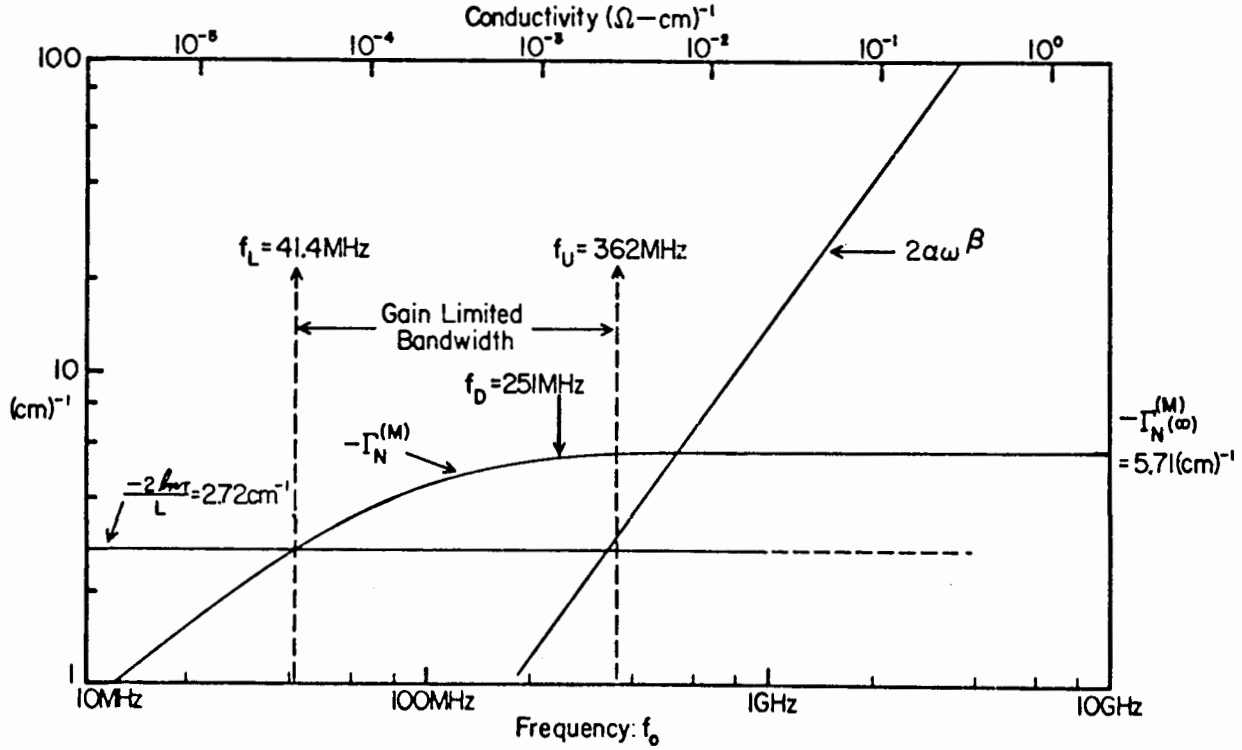

Fig. 2-10(b): CdSe-Shear; Maximized Gain Response

In viewing the results of this analysis we conclude that, of the six systems considered, the CdS longitudinal structure is the one most preferred. (The data for the thermal conductivity of ZnO is, however, very old (1929) and in light of new data this conclusion may be altered.)

2-5 Tuning Features of a Phonon Maser

In this section we will examine some of the secondary operational features of the Phonon Maser that are associated with the normal mode constraint:

$$\omega_n L(T,P)\left[\frac{1}{s_+[\sigma(T,I);\ \gamma_+(E);\ T]} + \frac{1}{s_-[\sigma(T,I);\ \gamma_-(E);\ T]}\right] + 2\theta(P) = 2\pi n \qquad (2\text{-}79)$$

As written, we have explicitly shown the functional dependence of the various terms, viz: temperature T; pressure P; light intensityI; and electric field E.

As acknowledged in the previous section the Maser goes into spontaneous oscillation at that normal mode, ω_n, nearest the frequency of maximum gain, ω_m. However, once oscillation is established slight variations in any of the independent variables (T,P,I, or E) produce a shift in the normal mode frequency, ω_n, in such a manner that equation

(2-79) continues to be satisfied. The specific meaning of the term, "slight variations", rests upon the restriction that,

$$\Delta\omega < \frac{\omega_1}{2} = \frac{\pi s_o}{2L} \qquad (2\text{-}80)$$

where $\Delta\omega$ is the shift in frequency and ω_1 is the fundamental frequency of the acoustical cavity. This restriction quarantees that the oscillator is not driven to either of the adjacent modes (a transition that takes place in a discontinuous fashion). Within this limit the Phonon Maser can be continuously tuned by any of the stated independent variables.

With the aid of equations (2-35) and (2-79) we will now undertake an analysis of the fractional tuning characteristics of a Phonon Maser. Specifically we will be interested in the following quantities:

(i) Conductivity Tuning (at constant voltage)

$$\frac{d(\ln\omega)}{d(\ln\sigma)} = \frac{\sigma}{\omega}\left[\frac{\partial\omega}{\partial s_+}\frac{\partial s_+}{\partial\sigma} + \frac{\partial\omega}{\partial s_-}\frac{\partial s_-}{\partial\sigma}\right] \qquad (2\text{-}81)$$

(ii) Voltage Tuning (at constant conductivity)

$$\frac{d(\ln\omega)}{d(\ln V)} = \frac{V}{\omega}\left[\frac{\partial\omega}{\partial s_+}\frac{\partial s_+}{\partial\gamma_+}\frac{\partial\gamma_+}{\partial V} + \frac{\partial\omega}{\partial s_-}\frac{\partial s_-}{\partial\gamma_-}\frac{\partial\gamma_-}{\partial V}\right] \qquad (2\text{-}82)$$

From the form of equation (2-79) it is evident that temperature and pressure tuning are also possible, viz:

(iii) Temperature Tuning (at constant voltage)

$$\frac{d(\ln\omega)}{d(\ln T)} = \frac{T}{\omega}\left[\frac{\partial\omega}{\partial L}\frac{\partial L}{\partial T} + \frac{\partial\omega}{\partial s_+}\frac{\partial s_+}{\partial T} + \frac{\partial\omega}{\partial s_-}\frac{\partial s_-}{\partial T} + \frac{\partial\omega}{\partial s_+}\frac{\partial s_+}{\partial\sigma}\frac{\partial\sigma}{\partial T} + \frac{\partial\omega}{\partial s_-}\frac{\partial s_-}{\partial\sigma}\frac{\partial\sigma}{\partial T}\right] \qquad (2\text{-}83)$$

(iv) Pressure Tuning

$$\frac{d(\ln\omega)}{d(\ln P)} = \frac{P}{\omega}\left[\frac{\partial\omega}{\partial L}\frac{\partial L}{\partial P} + \frac{\partial\omega}{\partial\theta}\frac{\partial\theta}{\partial P}\right] \qquad (2\text{-}84)$$

Our interest will lie, however, in (i) and (ii).

If we restrict our analysis to terms linear in χ and approximate the operating (threshold) frequency by ω_o, we obtain the following results for (i) and (ii).

(i) Conductivity Tuning (at constant voltage)

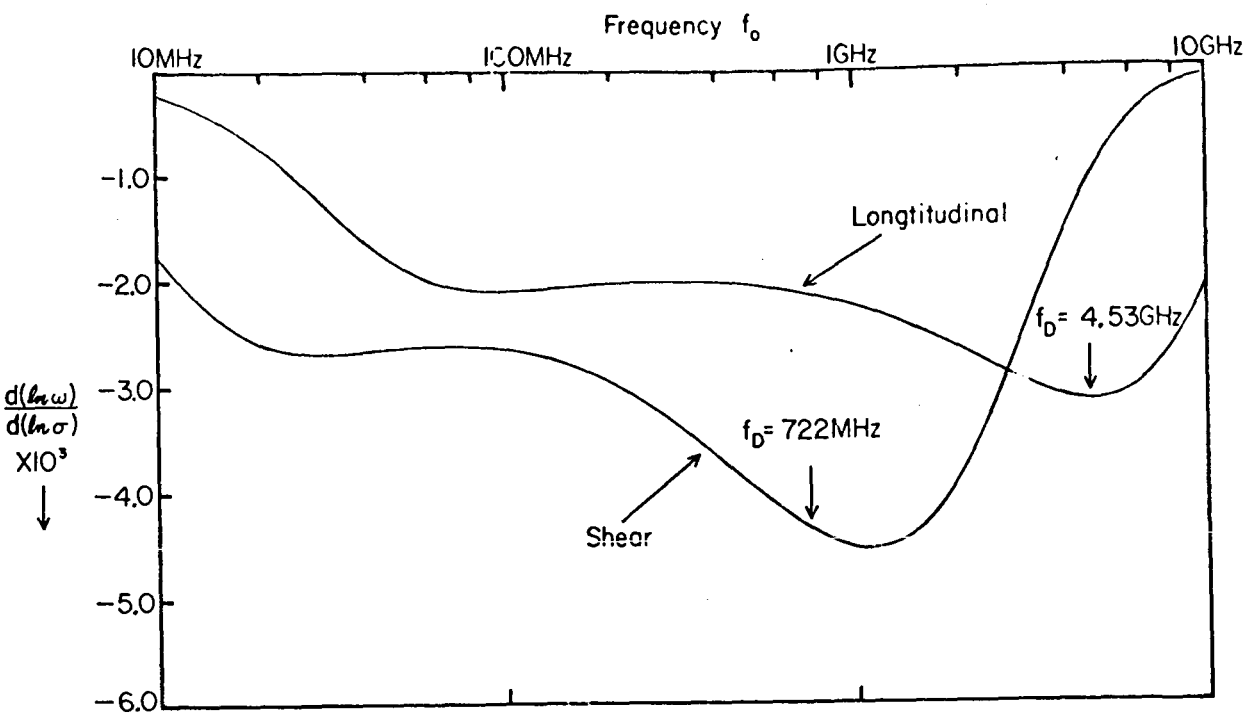

Fig. 2-11(a): Conductivity Tuning Versus Threshold Frequency

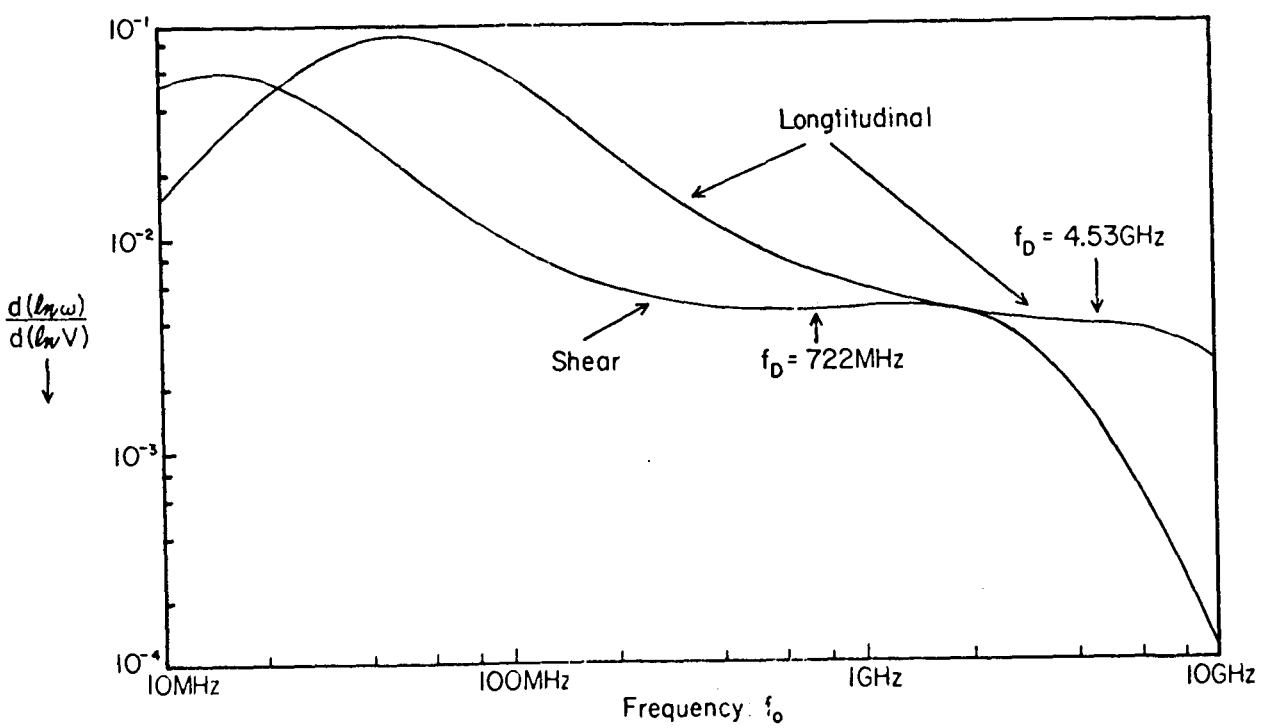

Fig. 2-11(b): Voltage Tuning Versus Threshold Frequency

$$\frac{d(\ln\omega)}{d(\ln\sigma)} = -\frac{\chi}{4}\left[\frac{4\omega_o^4+3\gamma_+^2\omega_o^2\omega_D^2}{(4\omega_o^2+\gamma_+^2\omega_D^2)^2} + \frac{4\omega_o^4+3\gamma_-^2\omega_o^2\omega_D^2}{(4\omega_o^2+\gamma_-^2\omega_D^2)^2}\right] \tag{2-85}$$

(ii) Voltage Tuning (at constant conductivity)

$$\frac{d(\ln\omega)}{d(\ln V)} = \frac{\chi\omega_o^2\omega_D^2}{2}(\gamma_+-\gamma_-)\left[\frac{\gamma_+}{(4\omega_o^2+\gamma_+^2\omega_D^2)^2} - \frac{\gamma_-}{(4\omega_o^2+\gamma_-^2\omega_D^2)^2}\right] \tag{2-86}$$

Figures 2-11(a) and (b) illustrate the corresponding detailed functional form of equations (2-85) and (2-86) for both shear and longitudinal structures in CdS, with: T = 10°C μ = 280 $cm^2/V\text{-}sec$, $\alpha = 1.11 \times 10^{-14}$, $\beta = 1.51$, $\frac{-\ln r}{L} = 2.5\ cm^{-1}$; and with γ_+ and γ_- calculated with the aid of equation (2-70).

2-6 The Open Circuit Acoustoelectric Voltage

Due to the intrinsic piezoelectric nature of the Phonon Maser there is associated with each acoustical signal a corresponding phase locked electromagnetic signal. The intent of this section is to derive the relationship between the two signals.

In the analysis to follow we will neglect any influence the external circuit may have on the operation of the Phonon Maser. This point of view is reasonable provided

the A.C. power dissipated in the external circuit is a small fraction of the total A.C. power (electrical plus acoustical) generated by the maser. [An analysis of this problem is treated in part by E.L. Adler and G.W. Farnell (Ad-66).] Within this approximation we may view the open circuit voltage as made up of two parts:

$$V = V_- + V_+ = \int_0^L [E_-(x) + E_+(x)]dx \qquad (2\text{-}87)$$

where E_- and E_+ are respectively the acoustoelectric fields associated with the forward and reverse going waves. Upon appealing to the defining set of equations for the system, equations (2-17) through (2-21), we are able to deduce the following expressions for the acoustoelectric field E accompanying a travelling wave of strain S:

$$E(x,t) = \frac{-4\pi\beta}{\varepsilon}\left[\frac{\gamma\tau\omega + iq_o^2R^2}{\gamma\tau\omega + i(1+q_o^2R^2)}\right] S(x,t) \qquad (2\text{-}88)$$

Realizing that $S = \partial u/\partial x$, the integral of equation (2-89) becomes,

$$V = A_-[u_-(L) - u_-(0)] + A_+[u_+(L) - u_+(0)] \qquad (2\text{-}89)$$

where

$$A_- = -\frac{4\pi\beta}{\varepsilon}\left[\frac{\gamma_-\tau\omega + iq_o^2R^2}{\gamma_-\tau\omega + i(1+q_o^2R^2)}\right] \rightarrow \frac{-2\pi\beta}{\varepsilon} \tag{2-90}$$

and

$$A_+ = \frac{-4\pi\beta}{\varepsilon}\left[\frac{\gamma_+\tau\omega + iq_o^2R^2}{\gamma_+\tau\omega + i(1+q_o^2R^2)}\right] \rightarrow \frac{-2\pi\beta}{\varepsilon}\left[1 + \frac{\omega_D}{\omega_D+i\omega_o}\right] \tag{2-91}$$

The limiting expression in each case corresponds to the approximate threshold conditions: $\omega_m = \omega_o$, $\gamma_- = 0$, $\gamma_+ = 2$.

Now in terms of the phenomenological model that we have adopted for the Phonon Maser, we have:

$$u_-(L) = e^{ik_-L}\, u_-(0) \tag{2-92}$$

$$u_+(L) = re^{i(k_-L+\theta)}\, u_-(0) \tag{2-93}$$

$$u_+(0) = re^{i(kL+\theta)}\, u_-(0) \tag{2-94}$$

where $k = k_- + k_+$. Substituting these results into equation (2-89) we obtain as our generalized expression:

$$V = A_- \left[(-1)^n e^{-\Gamma_- L} e^{i(\Delta qL - \theta)} - 1\right] u_-(0) + A_+ \left[(-1)^n e^{\Gamma_+ L} e^{i(\Delta qL + \theta)} - 1\right] \frac{u_-(0) e^{-i\theta}}{r} \qquad (2\text{-}95)$$

In carrying out this substitution we have made use of the normal mode condition, equation (2-54), and the explicit wave vector decomposition: $k = q + i\Gamma$. In addition we have neglected the lattice loss term, $2\Gamma_L$, and have introduced the wave vector difference parameter:

$$\Delta q = \frac{q_- - q_+}{2} \rightarrow \frac{\chi \omega_o}{8 s_o} \left[\frac{\omega_D^2}{\omega_D^2 + \omega_o^2}\right] \qquad (2\text{-}96)$$

(Once again the limiting value corresponds to the approximate threshold conditions: $\omega_m = \omega_o$, $\gamma_- = 0$, $\gamma_+ = 2$.) From the form of equation (2-95) it follows that in general both even and odd normal mode values of n give rise to an acoustoelectric voltage. We will look specifically at two limiting cases.

(i) Fixed Boundary Conditions

This corresponds to the situation: $r = 1$, $\theta = \pi$. Using the results of equations (2-90), (2-91) and (2-96) in equation (2-95) we obtain the following results.

$$|V| \simeq \frac{4\pi\beta}{\varepsilon}\left(\frac{s_o}{\omega_o}\right)\left[\frac{\omega_D^2}{\omega_o^2 + \omega_D^2}\right]^{\frac{1}{2}} |S_-(0)| \qquad (2\text{-}97)$$

(n - even)

$$|V| \simeq \frac{\pi\beta\chi_L}{4\varepsilon}\left[\frac{\omega_D^4(\omega_D^2+\omega_o^2)}{(\omega_o^2+\omega_D^2)^3}\right]^{\frac{1}{2}} |S_-(0)| \qquad (2\text{-}98)$$

(n - odd)

In carrying out the substitution a linear expansion of the exponential functions has been used (since their arguments are less than unity) and the appropriate expressions have been evaluated according to the approximate threshold conditions: $\omega_m = \omega_o$, $\gamma_- = 0$, $\gamma_+ = 2$. And as indicated the magnitude of the open circuit voltage has been evaluated in terms of the magnitude of the strain at the boundary $|S_-(0)|$, via the approximation: $S \simeq iq_o u$.

It will be noted that the effective integration

length for the even modes is the acoustical wavelength, $\lambda = {}^{s}o/f_o$, whereas, for the odd modes it is the scaled sample length, $\frac{\pi\chi L}{8}$.

(ii) Free Boundary Conditions

This corresponds to the situation: $r = 1$, $\theta = 0$. Within the same approximations as used for the fixed boundary conditions we obtain the following results.

$$|V| \simeq \frac{\pi\beta\chi}{4\varepsilon} L \left[\frac{(4\omega_o+3\omega_D)^2\omega_D^4 + 4(\omega_o+\omega_D)^2\omega_o^2\omega_D^2}{(\omega_o^2 + \omega_D^2)^3}\right]^{\frac{1}{2}} |S_-(o)| \qquad (2\text{-}99)$$

(n - even)

$$|V| \simeq \frac{4\pi\beta}{\varepsilon}\left(\frac{s_o}{\omega_o}\right)\left[\frac{4\omega_o^2 + 9\omega_D^2}{\omega_o^2 + \omega_D^2}\right]^{\frac{1}{2}} |S_-(0)| \qquad (2\text{-}100)$$

(n - odd)

Here we see that the role of the effective integrating length has been interchanged with respect to the fixed boundary conditions.

For purpose of comparison Fig. 3-12 illustrates the specific relative magnitude and frequency dependence of the four limiting cases (for a CdS shear mode structure characterized by a mobility of 280 $cm^2/V\text{-}sec$ and length of 582μ).

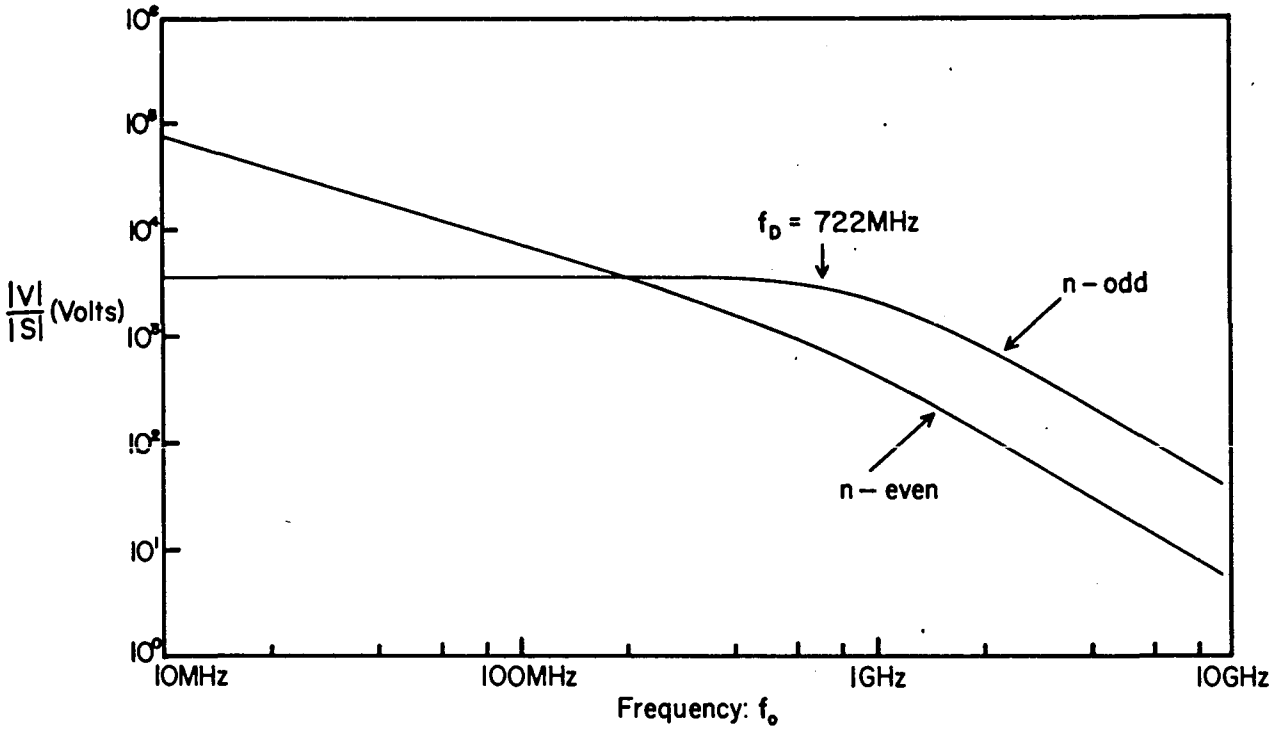

Fig. 2-12(a): Fixed Boundary Conditions; Open Circuit Voltage

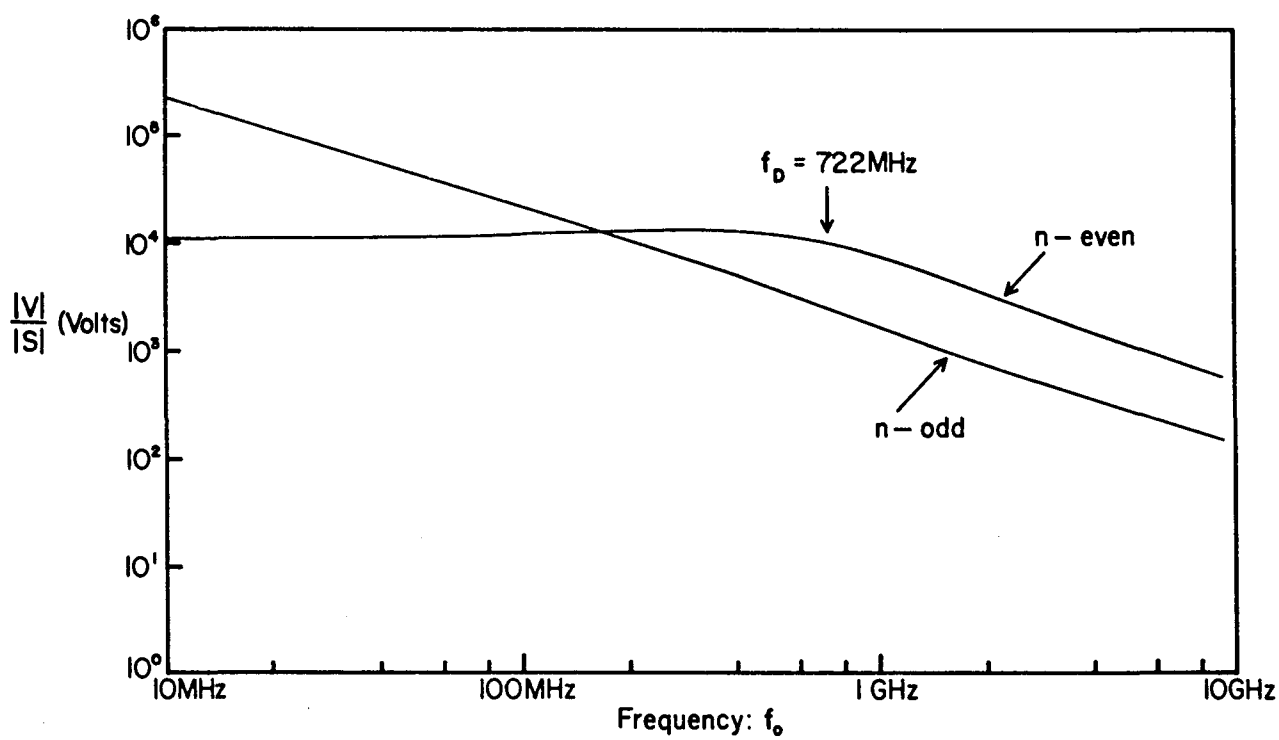

Fig. 2-12(b): Free Boundary Conditions; Open Circuit Voltage

CHAPTER III

Phonon Maser Theory: Some Non-Linear Features

3-1 Introduction

In this chapter a limited analysis of some of the non-linear features of the Phonon Maser system will be investigated. Of the possible sources of non-linearity attention will be restricted to the quadratic current density term arising out of the generalized expression for Ohm's Law, equation 2-20. Specifically, we have:

$$J = J_0 + J_L + J_{N.L.} \tag{3-1}$$

where

$$J_0 = -\mu e n_0 E_0 \tag{3-2}$$

$$J_L = \mu e(n_0 E - E_0 n) + \frac{1}{4\pi}\frac{\partial D}{\partial t} + \mu K t \frac{\partial n}{\partial x} \tag{3-3}$$

$$J_{N.L.} = \mu e n E \tag{3-4}$$

In the linear analysis of the preceeding chapter $J_{N.L.}$ was set equal to zero. In attempting now to incorporate this term an iteration point of view will be taken. A similar point of view has been taken by R. Mauro and W.C. Wang (Ma-70) in a colinear wave discussion of harmonic generation. In the zero iteration we set $J_{N.L.}$ equal to zero and obtain the linear results already considered. In the first order iteration we use the zero order travelling wave solutions to evaluate the non-linear term $J_{N.L.}$, i.e.:

$$n = n_- e^{i(k_- x - \omega t)} + n_+ e^{i(k_+ x + \omega t)} + c.c. \qquad (3\text{-}5)$$

$$E = E_- e^{i(k_- x - \omega t)} + E_+ e^{i(k_+ x + \omega t)} + c.c. \qquad (3\text{-}6)$$

In this way the set of non-linear equations transform to a linear, inhomogeneous set (of known inhomogeneity). In principle this procedure could be extended to an n^{th} level iteration, however, in the analysis to follow only a first order iteration will be considered.

Upon substituting the right and left travelling wave solutions of equations (3-5) and (3-6) into equation

(3-4) we obtain for the inhomogeneous term the following decomposition:

$$J_{N.L.} = J_1 + J_2 + J_3 + J_4 + J_5 + J_6 + J_7 + J_8 \qquad (3\text{-}7)$$

where

$$J_1 = \mu e n_- E_- e^{2i(k_- x - \omega t)} + c.c. \qquad (3\text{-}8)$$

$$J_2 = \mu e n_+ E_+ e^{2i(k_+ x + \omega t)} + c.c. \qquad (3\text{-}9)$$

$$J_3 = e n_- E_+^* e^{i[(k_- - k_+^*)x - 2\omega t]} + c.c. \qquad (3\text{-}10)$$

$$J_4 = \mu e n_+ E_-^* e^{i[(k_+ - k_-^*)x + 2\omega t]} + c.c. \qquad (3\text{-}11)$$

$$J_5 = \mu e n_- E_-^* e^{i(k_- - k_-^*)x} + c.c. \qquad (3\text{-}12)$$

$$J_6 = \mu e n_+ E_+^* e^{i(k_+ - k_+^*)x} + c.c. \qquad (3\text{-}13)$$

$$J_7 = \mu e n_- E_+ e^{i(k_- + k_+)x} + c.c. \qquad (3\text{-}14)$$

$$J_8 = \mu e n_+ E_- e^{i(k_+ + k_-)x} + c.c. \qquad (3\text{-}15)$$

3-2 Second Harmonic Generation

As indicated by equations (3-8) through (3-11) the first four terms of equation (3-7) correspond to source terms at twice the threshold frequency. In evaluating the corresponding strain, electric field, and self consistent current density one seeks the particular solution to the inhomogeneous set of equations. (The general solution to the homogeneous set corresponds to the linear analysis already considered.) When this is done one obtains the following generalized relationships with respect to the various source terms.

$$J = \sum_{n=1}^{4} \frac{-i\tau\omega_n}{k_n^2R^2 - i\tau\omega_n\left(\dfrac{1-\mu E_o k_n}{\omega_n}\right) + \dfrac{q_n^2 - k_n^2}{q_n^2-(1+\chi)k_n^2}} J_n \tag{3-16}$$

$$E = \frac{1}{\sigma}\sum_{n=1}^{4} \frac{-1}{\left(1 + \dfrac{q_n^2-(1+\chi)k_n^2}{q_n^2 - k_n^2}\right)\left[k_n^2R^2 - i\tau\omega_n\left(1-\dfrac{\mu E_o k_n}{\omega_n}\right)\right]} J_n \tag{3-17}$$

$$S = \frac{\beta}{\sigma c}\sum_{n=1}^{4} \frac{k_n^2}{q_n^2-k_n^2+[q_n^2-(1+\chi)k_n^2]\left[k_n^2R^2 - i\tau\omega_n\left(1-\dfrac{\mu E_o k_n}{\omega_n}\right)\right]} J_n \tag{3-18}$$

In deriving these results we have utilized the representative travelling wave form:

$$e^{i(k_n x - \omega_n t)} \tag{3-19}$$

for which

$$q_n = \frac{\omega_n}{s_o} \tag{3-20}$$

Without carrying out an explicit evaluation of equations (3-16) through (3-18) one can nevertheless appreciate the following generalizations.

(i) All second harmonic signals correspond to forced waves and are thus phase locked to their fundamental counterparts.

(ii) The principal contributions to the second harmonic strain, equation (3-18), come from the source terms J_1 and J_2 (since $|k_3| = |k_4| \simeq 0$).

(iii) In evaluating the second harmonic, open circuit voltage the contributions from J_3 and J_4 dominate. This conclusion is based on the realization that, aside from the influence of boundary conditions, the respective

integrals of equation (3-17) are approximately equal to the coefficient of the harmonic terms times the wave length of the corresponding signal. And since $\lambda_3, \lambda_4 >> \lambda_1, \lambda_2$ the contributions from J_3 and J_4 dominate.

3-3 The D. C. Acoustoelectric Current

Returning now to equation (3-7) we see that the last four terms constitute D.C. components. Specifically, upon combining equations (3-12) through (3-15) we obtain:

$$J_{D.C.} = 2\mu e \Big[\mathrm{Re}(n_- E_-^*) e^{-2\Gamma_- x} + \mathrm{Re}(n_+ E_+^*) e^{-2\Gamma_+ x} + e^{-\Gamma_N x} \{\mathrm{Re}(n_- E_+) + \mathrm{Re}(n_+ E_-)\} \cos (q_- + q_+) x - e^{-\Gamma_N x} \{\mathrm{Im}(n_- E_+) + \mathrm{Im}(n_+ E_-)\} \sin (q_- + q_+) x \Big] \qquad (3\text{-}21)$$

where we have used the decomposition,

$$k_- = q_- + i\Gamma_- \qquad (3\text{-}22)$$

$$k_+ = q_+ + i\Gamma_+ \qquad (3\text{-}23)$$

$$\Gamma_N = \Gamma_- + \Gamma_+ \qquad (3\text{-}24)$$

To obtain the average D.C. current density we now carry out a phase average over the length of the crystal, i.e.

$$\frac{1}{L}\int_{0}^{L}[J_{D.C.}]dx \tag{3-25}$$

In doing so we generate terms of the form,

$$e^{-2\Gamma L} \tag{3-26}$$

which, to a good approximation, can be expanded to terms linear in ΓL. If in addition we exploit the threshold conditions:

$$\Gamma_N \simeq 0 \tag{3-27}$$

and

$$(q_- + q_+)L = 2\pi n - 2\theta\,, \tag{3-28}$$

we generate the following expression for the D.C. acousto-

electric current density.

$$J_{D.C.} = 2\mu e[\mathrm{Re}(n_- E_-^*) + \mathrm{Re}(n_+ E_+^*)]$$
$$\frac{-2\mu e \sin\theta}{\pi n - \theta}\left[\{\mathrm{Re}(n_- E_+) + \mathrm{Re}(n_+ E_-)\}\cos\theta\right.$$
$$\left.+\{\mathrm{Im}(n_- E_+) + \mathrm{Im}(n_+ E_-)\}\sin\theta\right] \qquad (3\text{-}29)$$

In this form the first term corresponds to the quadratic self interaction of the right and left going components of the standing wave within the Maser, while the second term corresponds to the cross interaction of the two waves. Now for a real system, $\theta \simeq 0$ (free boundary conditions) and $n >> 1$. Thus the first term of equation (3-29) dominates, i.e.

$$J_{D.C.} \simeq 2\mu e[\mathrm{Re}(n_- E_-^*) + \mathrm{Re}(n_+ E_+^*)] \qquad (3\text{-}30)$$

Appealing now to the linear expressions for n_-, E_-^*, etc., we obtain to terms linear in χ:

$$n_- = q_{oe}^2 \frac{\beta}{}\left(\frac{1}{1+q_o^2R^2 - i\gamma_-\tau\omega}\right)u_- \qquad (3\text{-}31)$$

$$E_- = q_o \frac{c\chi}{\beta} \left(\frac{\gamma_- \tau\omega + iq_o^2 R^2}{i\gamma_- \tau\omega - q_o^2 R^2 - 1} \right) u_- \qquad (3\text{-}32)$$

$$n_+ = n_-(\omega \to -\omega) \qquad (3\text{-}33)$$

$$E_+ = E_-(\omega \to -\omega) \qquad)3\text{-}34)$$

When the appropriate substitutions are made we obtain the following result for the D.C. acoustoelectric current density:

$$J_{D.C.} = 4\mu c \ (\Gamma_+ - \Gamma_-) \ |S|^2 \qquad (3\text{-}35)$$

where we have used the identity,

$$q_o^2 |u|^2 = |S|^2 \qquad (3\text{-}36)$$

and the explicit expressions for Γ given by equation (2-36). Equation (3-35) is the standing wave generalization of the familiar Weinreich relationship for the D.C. acoustoelectric current associated with a travelling wave: (We-56), (MF-66).

As pointed out the influence of the cross interaction of the two waves is negligible, resulting in an expression corresponding to the simple superposition of two oppositely directed travelling waves. Coupling now equation (3-35) with the linear D.C. term, J_0, we obtain the following expression for the total D.C. current density within a Phonon Maser.

$$J = -\mu e n_0 E_0 + 4\mu c \, (\Gamma_+ - \Gamma_-) \, |S|^2 \qquad (3\text{-}37)$$

The physical origin of the D.C. acoustoelectric current stems from the conservation of linear momentum within the system. Specifically, the drifting electrons lose momentum at the expense of the growing acoustical signal (i.e., the right travelling wave). This loss in momentum translates itself into a D.C. current parallel to the growing wave (noting the negative sign of the charge carriers). For the acoustical signal undergoing attenuation, however, (i.e., the left travelling wave) momentum is transferred from the acoustical signal to the conduction electrons resulting in a D.C. current antiparallel to the attenuating wave (noting the sign of the carriers once again). Since the growing and attenuating waves are antiparallel to each other the two acoustoelectric currents add together and are directed antiparallel to the Ohmic term associated with the external bias field. All these features are reflected in equation (3-37).

From equation (3-37) we can draw the following conclusions about the I-V response of a Phonon Maser.

(i) Below threshold the system should behave in an Ohmic fashion since $|S| = 0$.

(ii) At and above threshold, $\Gamma_+ > 0$, $\Gamma_- < 0$, and $|S| > 0$, resulting in a decrease in the current density from its Ohmic response.

(iii) In principle the slope of the I-V curve at and above threshold can be either positive or negative depending upon the value of the field derivative of the second term with respect to the first.

(iv) Changes in mode structure, resulting in changes in $|S|$, will be reflected by discontinuous variations in J.

CHAPTER IV

Experimental Apparatus and Data Presentation

4-1 Introduction

In this chapter an experimental study of a Phonon Maser is presented and correlated with the theoretical developments of the preceding pages. The principal objective is a verification of the threshold response of the system in terms of the linear formulation of Chapter II. In short, this corresponds to a verification of the two equations constituting the threshold criteria:

$$\Gamma_N(\omega,v,\sigma,T) + 2\Gamma_L(\omega) - 2\frac{\ln r}{L} = 0 \qquad (4\text{-}1)$$

$$\omega L\left[\frac{1}{s_+(\omega,v,\sigma,T)} + \frac{1}{s_-(\omega,v,\sigma,T)}\right] + 2\theta = 2\pi n \qquad (4\text{-}2)$$

Specifically, a study of the threshold frequency versus conductivity, drift velocity and temperature is presented and compared with those expressions resulting from equation (4-1). In addition conductivity and voltage tuning data is

presented and compared with the corresponding expressions resulting from equation (4-2). Further to this, some data is presented on the incubation time of the system and the temperature dependence of the drift mobility and threshold frequency line width. The principal non-linear features to be presented relate to harmonic generation and to the I-V response of the system.

All the data to be presented correspond to a shear mode system fabricated from photoconductive CdS. (And for the sake of completeness the data can be found in tabular form in Appendix III.)

4-2 Experimental Apparatus

As indicated by the analysis of section 2-6 most of the features of the threshold acoustical signal are mirrored by a corresponding phase locked acoustoelectric voltage. Because of its more tractable character the latter was used exclusively in collecting the data at hand. The specific experimental arrangement employed is illustrated by the schematic representation of Figure 4-1, and will now be discussed.

The CdS crystal, having been prepared in accordance with the prescription of Appendix I, was clamped between two optically flat electrodes. The anode consisted of a copper disc and the cathode of transparent conducting glass (Nesa

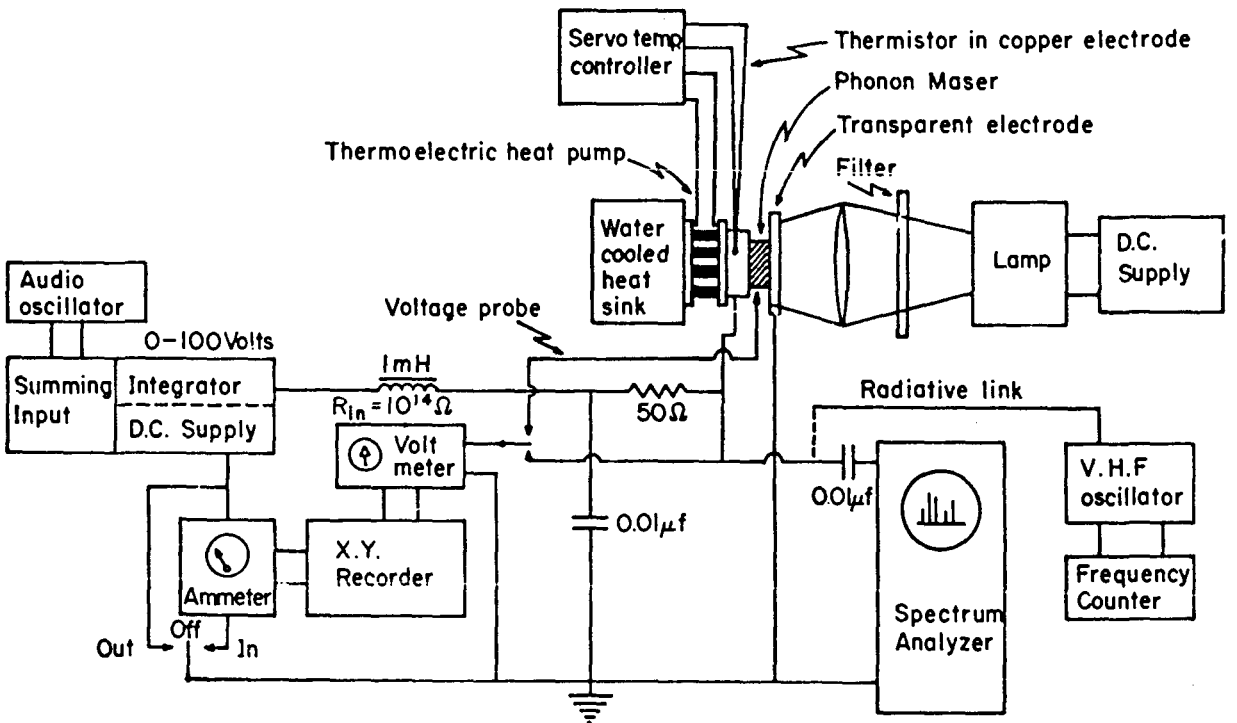

Fig. 4-1: Schematic Representation of Experimental System

glass). To control the temperature of the crystal the copper electrode was soldered to a thermoelectric heat pump which was in turn servo-stabilized by a thermistor feedback system. An effective temperature stability of under 1°C was maintained for a corresponding 3 watt variation in the power dissipated by the Phonon Maser. In addition it was possible to manually vary the stabilized temperature by as much as ±30°C about the ambient value.

The conductivity of the crystal was determined by the amount of light incident on the crystal face through the transparent electrode and could be varied through 4 orders of magnitude [10^{-6} to 10^{-2} $(\Omega\text{-cm})^{-1}$]. The light source itself consisted of a D.C. powered filament projection lamp. A low pass filter ($\lambda \geq 5400$ Å) was inserted in the beam to restrict the incident illumination to less than band gap energy. Due to the resultant low optical absorption coefficient (1 - 10 cm^{-1}) a fairly homogeneous conductivity existed throughout the crystal.

The D.C. bias voltage was supplied by a multi-function unit which could be used alternately as an integrator, a fixed supply, or a summer. The particular function employed depended on the measurement being made. For example the summing function was employed in measuring the voltage tuning characteristics of the Maser and the fixed supply for the threshold measurements. In obtaining the I-V response of the

Maser the integrating mode was employed resulting in a slow uniform sweep from zero to 100 volts. As the voltage sweep took place the corresponding I-V dependence was plotted by the X-Y recorder. The electrical circuit was completed by a series inductor and a shunting capacitor (designed to isolate the A.C. and D.C. signals) and a series 50 Ω resistor. The series resistor provided the appropriate impedance match to the spectrum analyzer and resulted in a signal level given by:

$$V_{S.A.} = \frac{Z_S}{Z_S + Z_X} V_{O.C.} \qquad (4\text{-}3)$$

Here $V_{o.c.}$ is the open circuit voltage discussed under section 2-6 and Z_x and Z_s are the crystal and series resistor impedance respectively.

To obtain an accurate frequency determination of the Phonon Maser signal the following scheme was employed. Having identified the signal of interest with the spectrum analyzer a second signal from a V.H.F. oscillator was introduced and tuned until it coincided exactly with the Maser signal. The V.H.F. oscillator was simultaneously fed to a frequency counter from which the frequency data was obtained. With the spectrum analyzer set to high resolution an accuracy of ± 1 kHz could be obtained in this way.

The remaining feature of the experimental arrangement was a voltage probe at the edge of the crystal. This consisted of a sharp (<10μ) stainless steel point mechanically mounted to a high resolution micromanipulator. By positioning the point on the edge of the crystal at measured intervals (typically 25μ) a profile of the voltage across the crystal was obtained. It was mandatory in making this measurement to use a high impedance ($\sim 10^{14}$ Ω) electrometer. In this way the influence of the blocking contact, associated with the CdS-stainless steel interface, could be neglected. (The ammeter was disconnected from the X-Y recorder in making this measurement and the position axis of the recorder was manually advanced in proportion to the advancement of the micromanipulator.) The voltage profile thus obtained gave one information relevant to the diffusion depth of the indium contacts and helped identify any blocking contacts. But most important, the non-uniform fields associated with the profile could be quantitatively integrated into an analysis of the threshold data.

4-3 Data Presentation

(i) Voltage Profile, I-V Response and Incubation Time

Figure 4-2(a) and 4-2(b) are respectively examples of the I-V response and voltage profile of a Phonon Maser. In reference to the voltage profile of Figure 4-2(b) the low

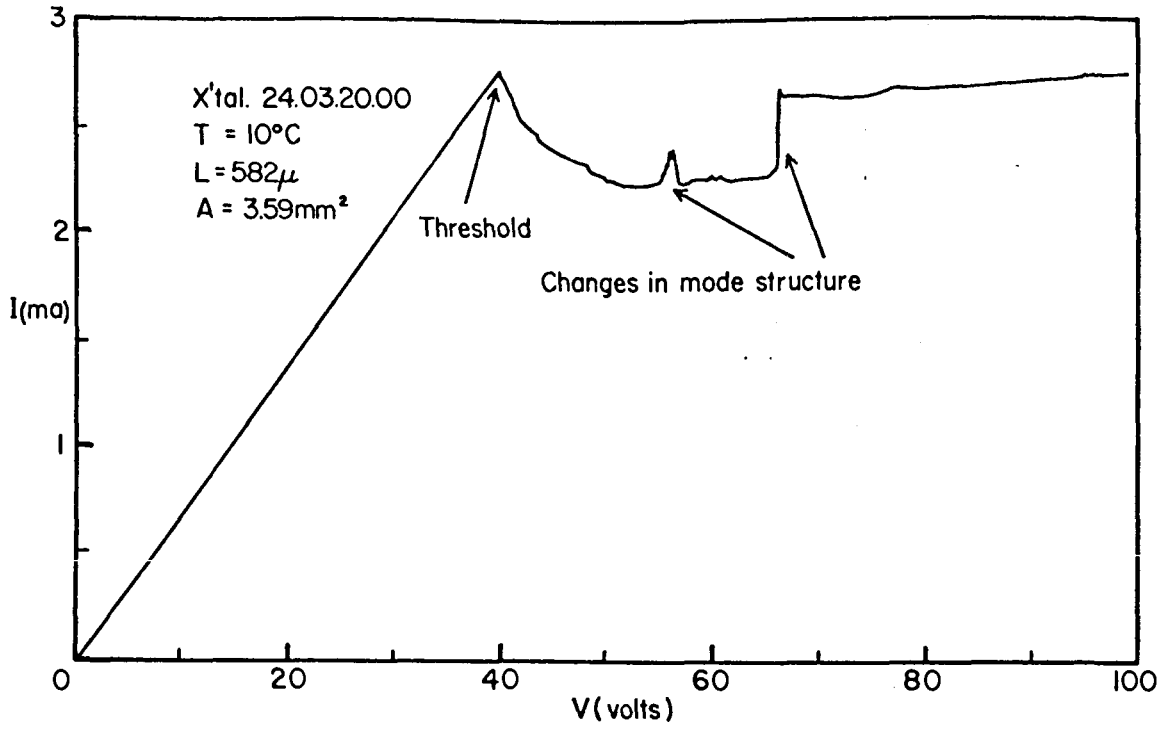

Fig. 4-2(a): Phonon Maser I-V Response

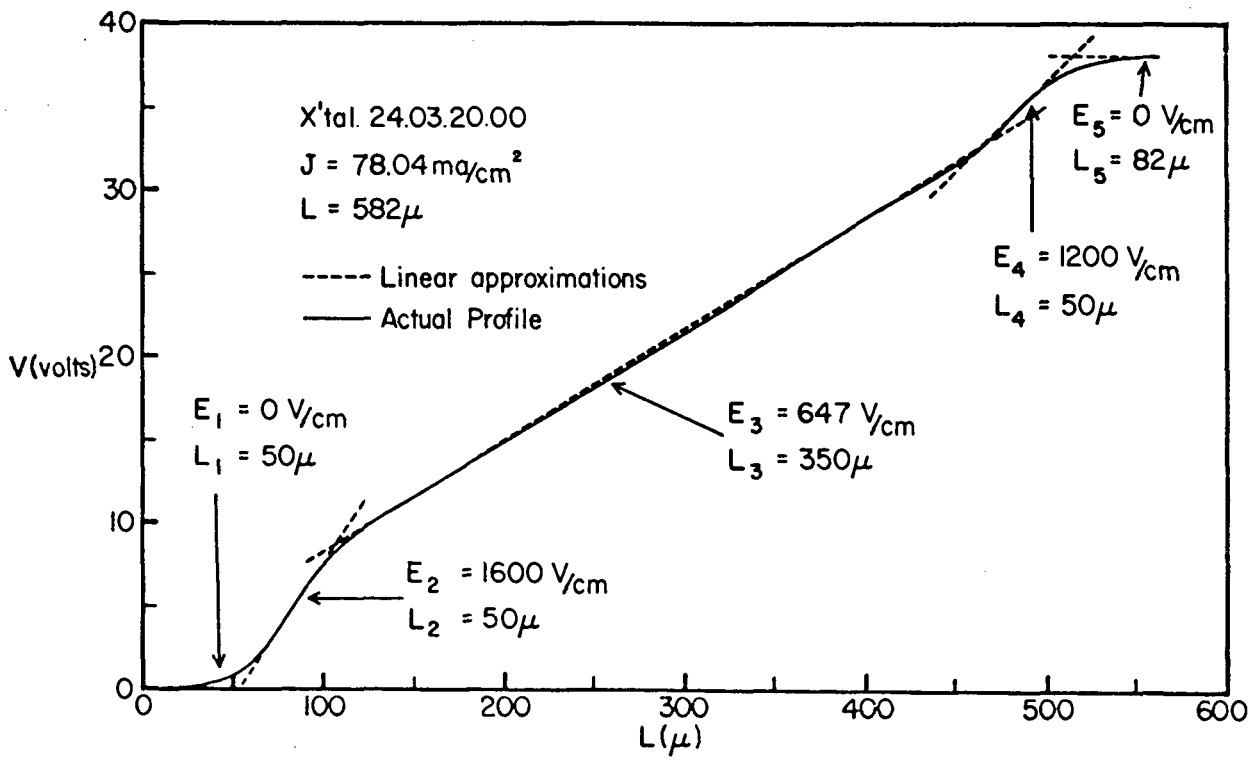

Fig. 4-2(b): Phonon Maser Voltage Profile

field regions at the faces of the crystal are associated with the indium diffusion process employed in forming the ohmic contacts. As indicated, for the time (10 min.) and temperature (500°C) used, an effective depth of 50 μ is obtained. One is cautioned in identifying this distance as the diffusion depth of Indium into CdS, for in addition to the diffusion of indium into CdS there exists the possibility of the diffusion of compensating impurities and indeed sulfur itself out of CdS. The latter feature, in part, helps explain the existence of the high field regions adjacent to the low field contact regions. In any event the effective diffusion depth becomes an important consideration as one attempts to make progressively thinner devices. This follows from the realization that both the low field contact regions and the adjacent high field regions correspond to domains of net acoustical attenuation for the threshold frequency defined now by the generalized threshold equations:

$$\int_0^L \Gamma_N[\omega,\sigma(x),\, v(x)]dx + 2L\Gamma_L(\omega) - 2\ln r = 0 \qquad (4\text{-}4)$$

$$\omega \int_0^L \left[\frac{1}{s_+(x)} + \frac{1}{s_-(x)}\right] dx + 2\Theta = 2\pi n \qquad (4\text{-}5)$$

Since an additional loss mechanism has been introduced the principal effect is an increase in the threshold velocity (of the active region) over that given by the uniform field assumption.

For the two samples employed in this analysis the influence of the central active region dominated the systems. However, for optimum agreement between experiment and theory the influence of the field profile had to be considered. The dashed lines of Figure 4-2(b) represent a typical decomposition of the profile in carrying out a series approximation to the integrals of equations (4-4) and (4-5).

The linearity of the zero intercept of the I-V curve of Figure 4-2(a) identifies the contacts as ohmic and as can be seen, the system itself responds in a linear (ohmic) fashion for sub-threshold fields. At threshold the criteria of equations (4-4) and (4-5) are met, resulting in the spontaneous generation (from the thermal background) of a sustained acoustical signal. As discussed in Chapter III a corresponding D.C. acoustoelectric current is produced which in turn is responsible for the non-linear behavior of the I-V curve. Indeed, the deviation from linearity serves as a measure of the strength of the corresponding acoustical signal as indicated by equation (3-37). Although we shall be primarily concerned with the behavior of the system at threshold it is interesting to note that in spite of a

seemingly strong self locking action the frequency of operation undergoes discontinuous changes as the drift field is driven beyond the threshold value. Correspondingly there are discontinuous variations in the I-V response of the system, as indicated by Figure 4-2(a). The general tendency is for the system to shift to lower frequencies and to take upon a more complex harmonic structure as the field is increased beyond threshold.

At threshold the acoustoelectric signal, as monitored by the system of Figure 4-1, generally consists of two components: the threshold frequency, f_m, and its first harmonic, $2f_m$. Figure 4-3(a) and 4-3(b) are respectively a time and frequency display of a characteristic threshold signal. Figure 4-3(d) is in turn a high resolution display of the threshold frequency and illustrates the high spectral purity of a Maser signal. Figure 4-3(c) is a time envelope display corresponding to the onset and extinction of oscillation and was obtained by first biasing the Maser just below threshold and then applying a square pulse (through the summing input of the power supply) of sufficient amplitude to drive the system slightly beyond threshold. To obtain the real time display the resulting acoustoelectric signal was first mixed with a signal from the V.H.F. oscillator (which differed slightly in frequency) producing a difference frequency (~10 MHz) that fell within the band width of the

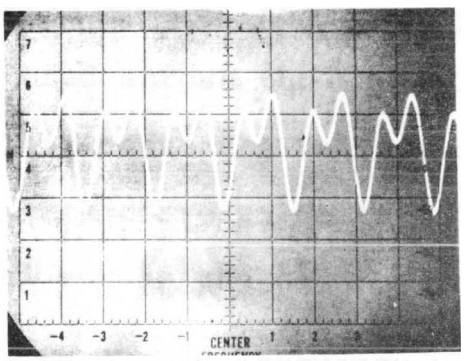

10nsec/div

FIG. 4-3 (A): TIME DISPLAY OF THRESHOLD SIGNAL

Zero freq. marker

$2f_m$ = 128.772MHz

f_m = 64.386MHz

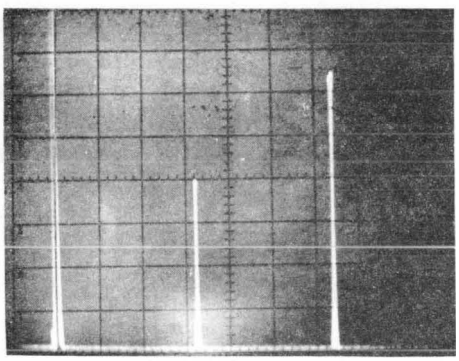

20MHz/div

FIG. 4-3 (B): FREQUENCY DISPLAY OF THRESHOLD SIGNAL

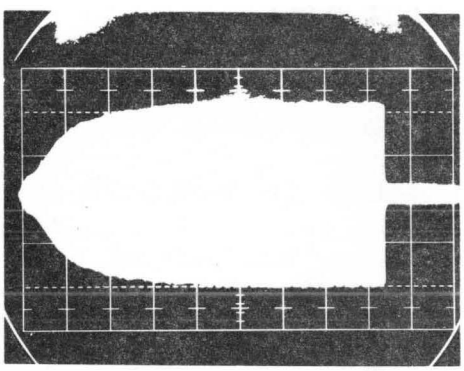

50msec/div

FIG. 4-3 (C): INCUBATION AND EXTINCTION RESPONSE

f_m = 64.386MHz

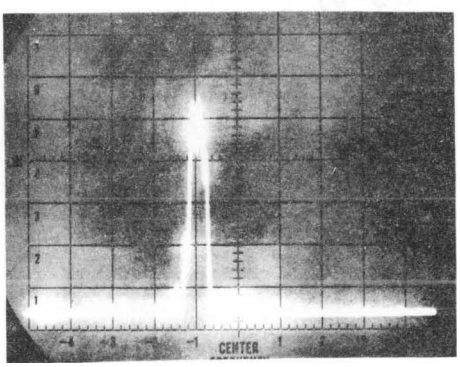

20 Hz/div

FIG. 4-3 (D): LINE WIDTH OF THRESHOLD SIGNAL

observing oscilloscope. As indicated by the diagram a characteristic incubation time of 50 msecs was observed. The rise time of the corresponding square wave pulse, as monitored across the crystal, was less than 1 msec, giving credibility to the measurement. The observed 50 msec incubation time corresponds to 1.52×10^5 transits of the acoustical signal across the cavity (for the 582μ thick crystal employed).

(ii) Threshold Frequency Versus Current Density (Conductivity)

According to the linear analysis of section 2-3 a unique relationship exists between the frequency of maximum gain (threshold frequency) and the conductivity of the crystal, viz:

$$f_m = f_o(1 + \delta) \tag{4-6}$$

where

$$f_o = \frac{\omega_o}{2\pi} = \left[\frac{\omega_D}{\pi\epsilon}\,\sigma\right]^{\frac{1}{2}} \tag{4-7}$$

and

$$\delta \simeq \delta_1 = \left[\frac{2\chi\omega_D\omega_o^{4-\beta}}{\alpha\beta s_o} \left(\frac{\gamma_-}{[4\omega_o^2+\gamma_-^2\omega_D^2]^2} + \frac{\gamma_+}{[4\omega_o^2+\gamma_+^2\omega_D^2]^2} \right) - \beta+1 \right]^{-1} \tag{4-8}$$

with γ_+ and γ_- evaluated with the aid of,

$$v_{th} = s_o \left[1 + \frac{2(\omega_o^4+\omega_o^2\omega_D^2)}{3\omega_o^2\omega_D^2+\omega_D^4} + \frac{16 s_o}{\chi\omega_D} \frac{(\omega_o^2+\omega_D^2)^2}{3\omega_o^2\omega_D^2+\omega_D^4} \left(\alpha\omega_o^\beta - \frac{\ln r}{L} \right) \right] \tag{4-9}$$

Thus for a given mobility, temperature, thickness and reflection coefficient the threshold frequency can be calculated as a function of conductivity. Implicit in the set of equations (4-6) through (4-9), is the underlying assumption that a uniform field exists across the crystal which in turn implies a homogeneous conductivity. However, as already noted this is not the case. To be rigorous then, one must carry out the integral of equation (4-4). In doing so the lattice loss term of equation (2-66) was used with $\alpha = 1.11 \times 10^{-14}$ and $\beta = 1.51$ (Ma-69). Further, since a unique conductivity can no longer be assigned to the crystal we are forced to choose the current density as our independent variable.

Figure 4-4(a) and 4-4(b) display the threshold frequency - current density relationship as obtained from two separate crystals of differing thickness, temperature, mobility and reflection coefficient. In collecting this data the following procedures were employed. The desired current density was first determined by controlling the light level incident on the crystal (with the bias voltage held just below threshold). With this established the bias voltage was returned to zero and then slowly increased to threshold (defined by the appearance of an acoustoelectric signal). The corresponding current, voltage, threshold frequency, field profile, and voltage and conductivity tuning characteristics were then recorded.

In carrying out a profile compensated, theoretical analysis of a threshold frequency - current density data point the threshold condition, equation (4-4), (less the end loss term, $-2\frac{\ln r}{L}$) was first plotted as a function of frequency for varying values of mobility. In doing so a summation approximation to the integral was used, with the field profile measurement providing the necessary input data. For each mobility value the minimum point of the curve suggested a specific value for the end loss term, as dictated by equation (4-4), and the corresponding frequency represented the theoretical, field compensated threshold frequency. This procedure was repeated for all data points.

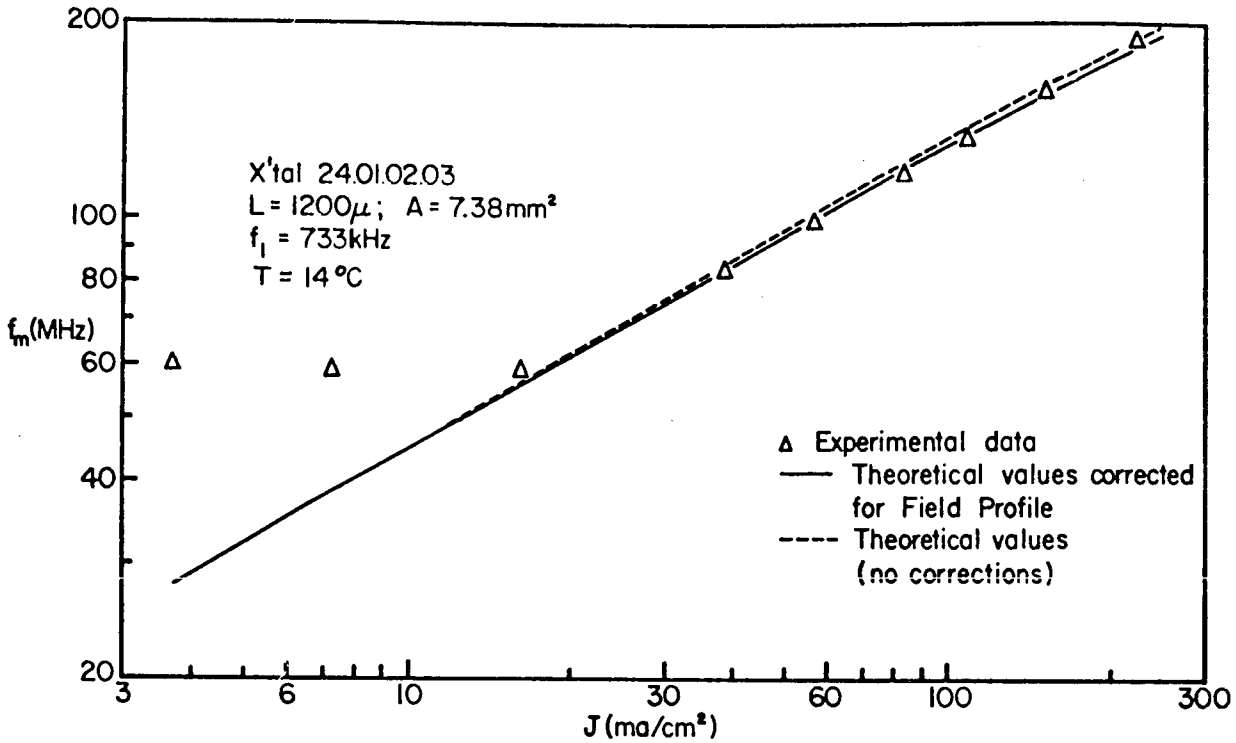

Fig. 4-4(a): X'tal 24.01.02.03; Threshold Frequency Versus Current Density

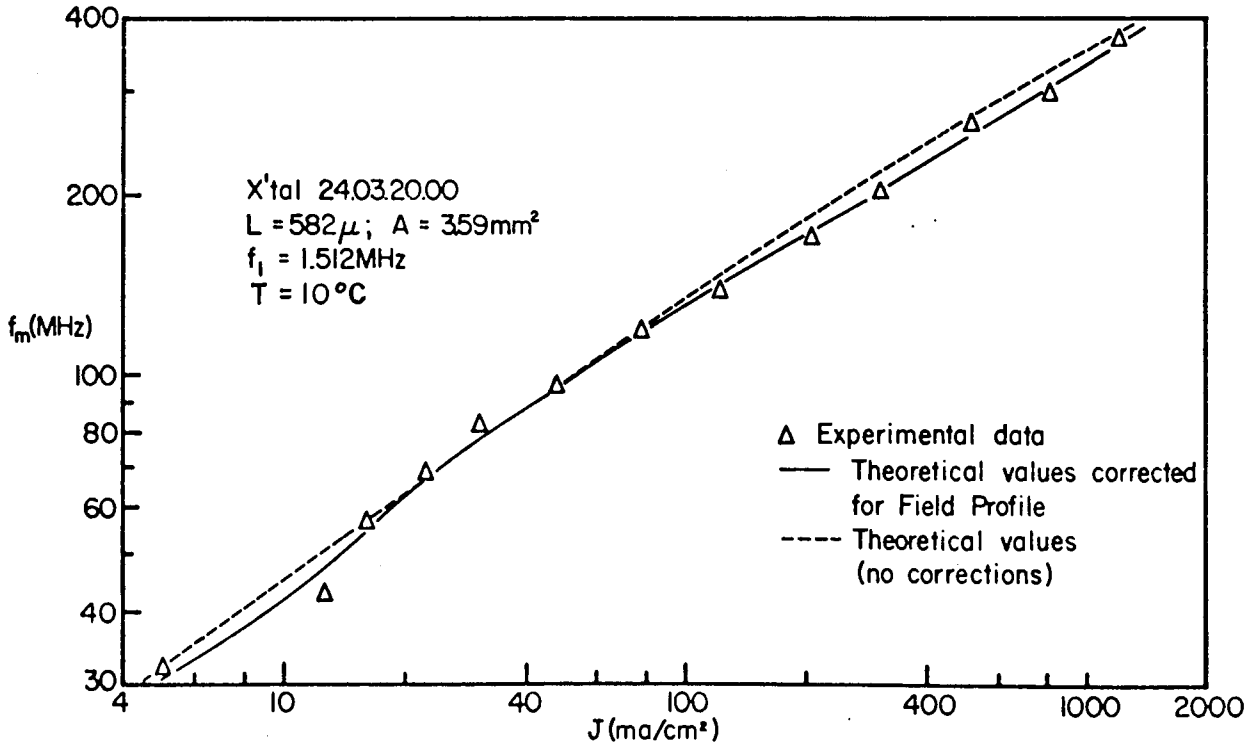

Fig. 4-4(b): X'tal 24.03.20.00; Threshold Frequency Versus Current Density

With the mobility and end loss term left as floating parameters, optimum agreement was then sought between the experimentally observed threshold frequencies and the various mobility dependent, theoretical values (subject, however, to the constraint that a common end loss value apply to all data points). The solid lines of Figure 4-4(a) and 4-4(b) are smooth curves joining the corresponding optimum fit, profile compensated theoretical points.

On the assumption now that each crystal can be characterized by a unique mobility (independent of conductivity), the credibility of the theoretical formulation can then be tested by the variance data of the mobilities as deduced by the above analysis; namely, the credibility will vary inversely as the variance: $<(\mu-\bar{\mu})^2>^{\frac{1}{2}}$.

As indicated by the variance data of the following table, the theoretical formulation is strongly endorsed. In addition it is important to note that the deduced mobilities, $\bar{\mu}$, are consistent with those values generally associated with CdS (as enumerated by Appendix II).

Table 4-1

Deduced Maser Parameter

X'tal	T	L	$-2\frac{\ln r}{L}$	r	$\bar{\mu}$	$<(\mu-\bar{\mu})^2>^{\frac{1}{2}}$
	(°C)	(μ)	(cm^{-1})		(cm^2/V-sec)	cm^2/V-sec
24.01.02.03	14	1200	5.0	~0.7	370	2.9
24.03.20.00	10	582	6.0	~0.8	310	8.2

Having established a mean mobility and end loss value for the two crystals, these values were then used in the uniform field formulation of equations (4-6) through (4-9) to generate the dashed curves of Figures 4-4(a) and 4-4(b). Here again the credibility of the theoretical formulation is reinforced by the relatively good agreement with the experimental data.

To this point there has been no comment on the seemingly anomalous, low current density behavior of crystal 24.01.02.03. Of a number of possible explanations, the one that is judged most likely is that as the conductivity (current density) is lowered the intrinsic dark conductivity begins to play a dominant role. And should there be any

inhomogeniety in the intrinsic conductivity (say a relatively high conductivity region over a small fraction of the cross sectional area) then that region will dominate the acousto-electric behavior of the system, resulting in a signal frequency representative of the corresponding conductivity and independent of the overall current density.

(iii) Threshold Velocity Versus Threshold Frequency

As indicated previously, one is unable to assign a unique conductivity to crystals possessing a non-uniform field profile. In like manner the concept of a unique threshold velocity loses its meaning. However, this concept can be retained in the following context.

With reference to the characteristic voltage profile of Figure 4-2(b) it has been acknowledged that (for the frequency of operation) only the uniform central region possesses net gain at threshold. The concept of a threshold velocity can then be applied to this region and corresponds to that value, within the central region, for which the corresponding net gain is sufficient to compensate all the characteristic losses (lattice and end losses) in addition to those incurred by the contact profiles.

Figures 4-5(a) and 4-5(b) represent the relevant data for the two crystals employed. In establishing the data points, those mobility values obtained by the optimum

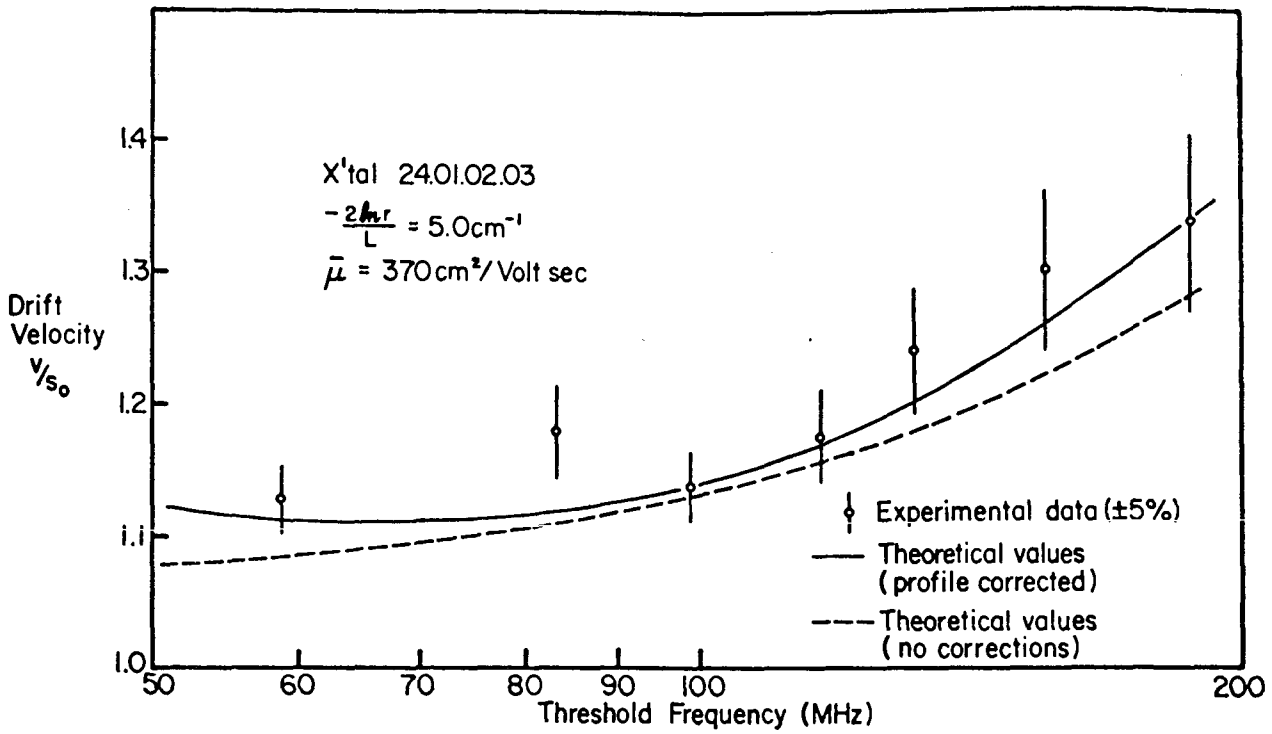

Fig. 4-5(a): X'tal 24.01.02.03; Threshold Drift Velocity Versus Threshold Frequency

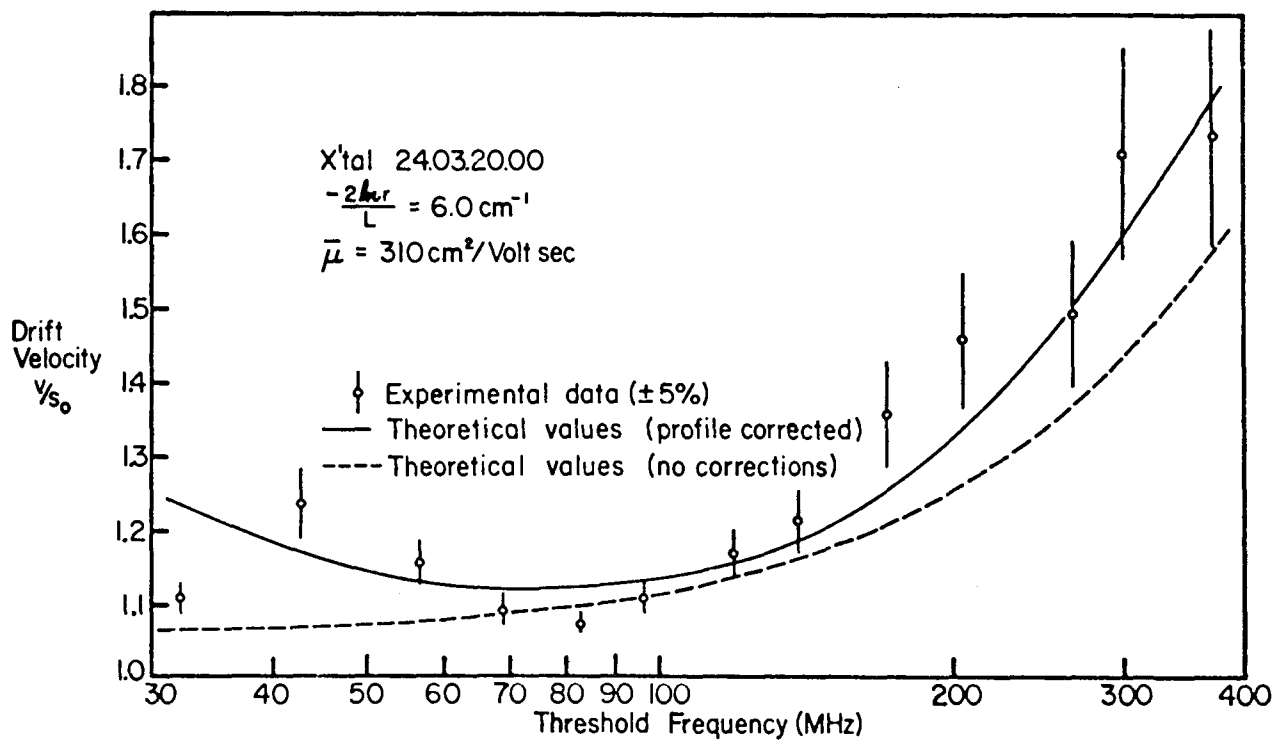

Fig. 4-5(b): X'tal 24.03.20.00; Threshold Drift Velocity Versus Threshold Frequency

fit procedure of the previous section and the electric fields corresponding to the uniform region of the measured voltage profiles were used in evaluating the corresponding central region threshold velocities:

$$v/s_o = \frac{\mu E}{s_o} \qquad (4\text{-}10)$$

The solid line is a smooth curve through a set of points corresponding to a theoretical determination of the central threshold velocities. The values were calculated via equation (4-4) in a manner similar to the optimum fit procedure of the last section. However, in this case the drift velocity of the central region served as the unknown parameter, with the measured contact profiles, the measured threshold frequency, and the mean mobility and end loss values of Table 4-1 serving as input data. In this way unique values for the corresponding central threshold velocities were obtained. The dashed curves of Figures 4-5(a) and 4-5(b) correspond to the uniform field expression given by equation (4-9). Again the mean mobility and end loss values of Table 4-1 were used.

As indicated by the relative agreement of Figures 4-5(a) and 4-5(b) the theoretical formulation is once again substantiated. In addition we see the inadequacy of the linear intercept approximation, that has gone into equation

(4-9), at the low and high frequency ends of the curve.

(iv) Threshold Frequency and Line Width Versus Temperature

As an alternate test of the theoretical formulation the role of the temperature and current density (conductivity) variables were interchanged. That is, with the current density now held constant the temperature dependence of the threshold frequency was monitored and compared with the theoretical results of equation (4-4). Figure 4-6(a) illustrates the relevant data.

In collecting this data a constant current density was maintained (for varying temperature and threshold fields) by adjusting the light level incident on the crystal. Once again the voltage profile at threshold was monitored for each data point and used as input data in the evaluation of equation (4-4). The optimum fit procedure of section (ii) was again employed but with only the mobility left as a floating parameter. The end loss value of Table 4-1 was used throughout. As indicated by Figure 4-6(a) substantial agreement was obtained between experiment and theory, leading once again to an endorsement of the theoretical formulation.

In executing the optimum fit procedure the temperature dependence of the drift mobility is deduced. The results of this analysis are illustrated by Figure 4-6(b). This data agrees qualitatively with that obtained by Kikuchi

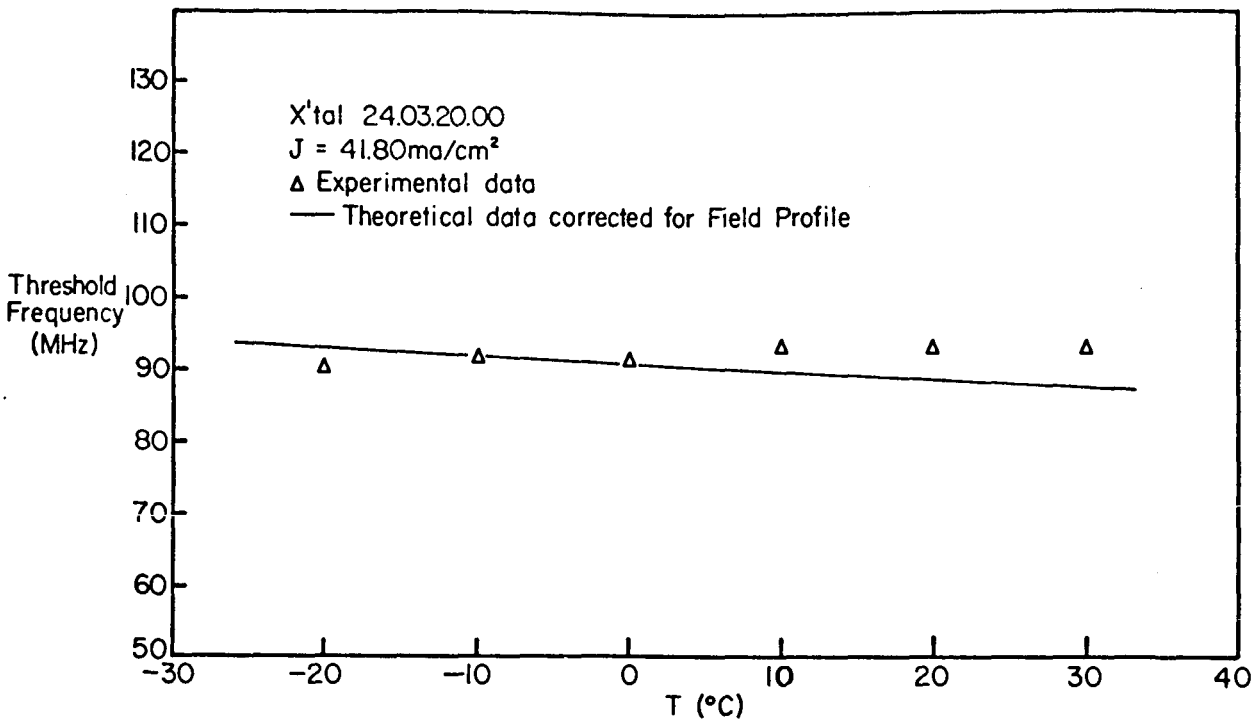

Fig. 4-6(a): X'tal 24.03.20.00; Threshold Frequency Versus Temperature

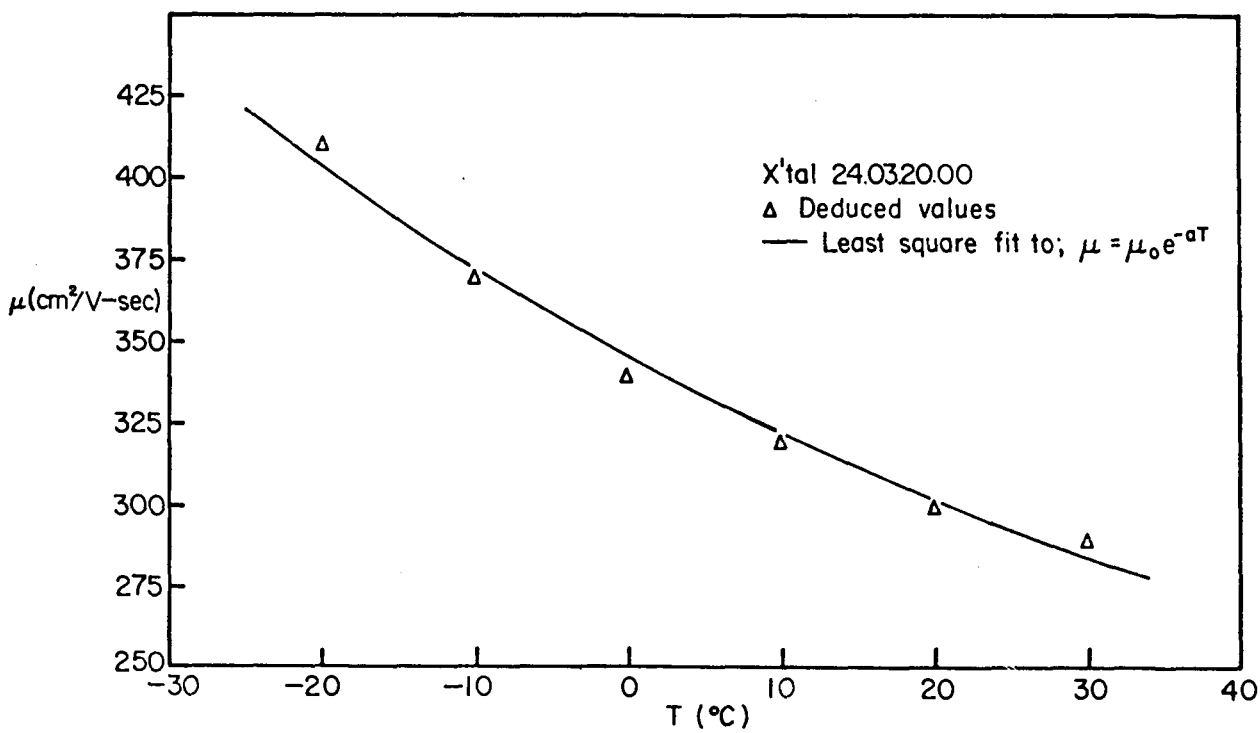

Fig. 4-6(b): X'tal 24.03.20.00; Drift Mobility Versus Temperature

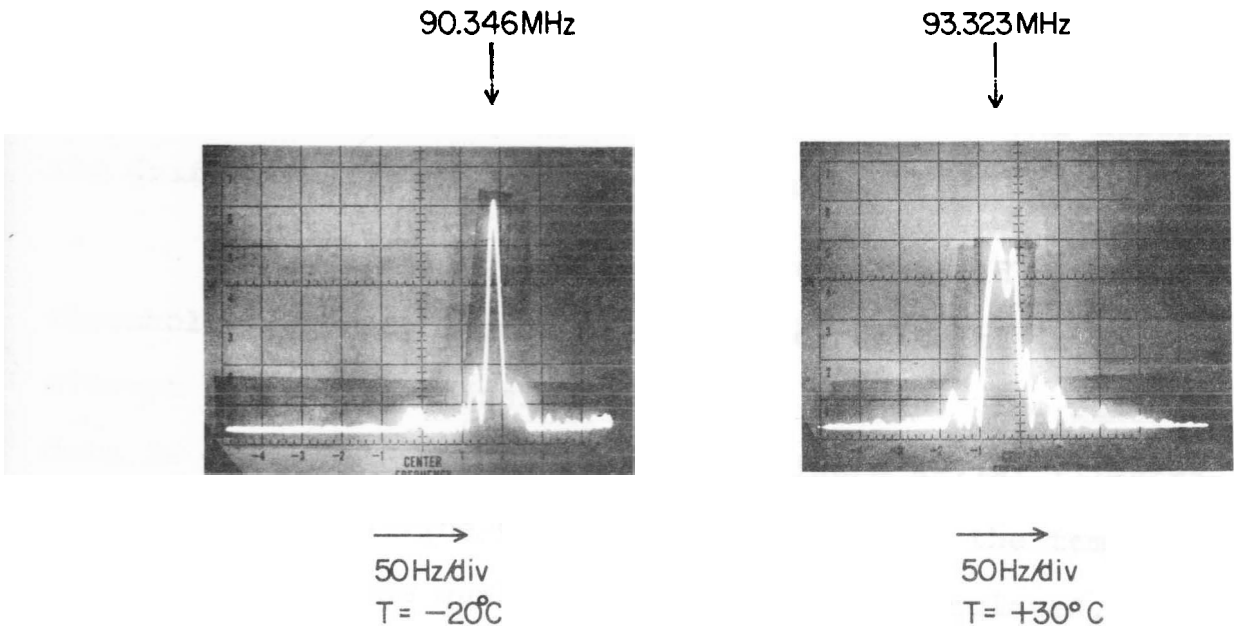

FIG. 4-7 (A): LINE WIDTHS AT T = -20°C AND T = +30°C.

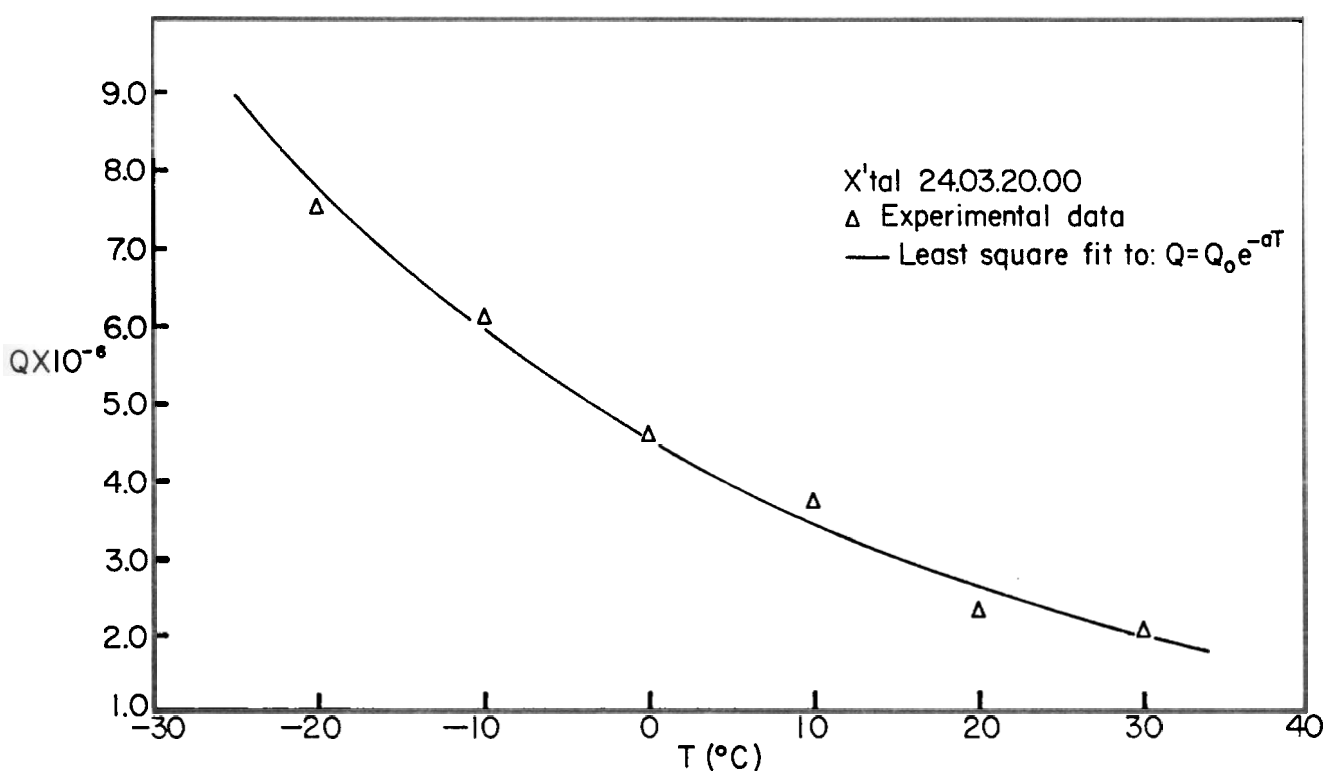

FIG. 4-7 (B): TEMPERATURE DEPENDENCE OF QUALITY FACTOR

and Tinuma (Ki-67), who carried out a temperature analysis of one way acoustical gain in CdS and in like manner deduced the drift mobility-temperature dependence.

In collecting the temperature-threshold data the threshold frequency line width was also monitored in an attempt to gain some insight as to its origin. The relevant data is given by Figure 4-7(b), with Figure 4-7(a) illustrating the observed line widths at the limits of the temperature range covered. The quality factor, Q, was calculated, in each case, on the basis of the simple formula,

$$Q = \frac{f}{\Delta f} \tag{4-11}$$

with Δf corresponding to the measured line width. It is strongly suggested by this data that the line width is related in some way to the inherent thermal fluctuations of the system.

(v) Voltage and Conductivity Tuning Response Versus Threshold Frequency

To this point in the analysis only the gain requirements of threshold, equation (4-1) or (4-4), have been tested against experimental data. In testing the remaining normal mode criterion, equation (4-2) or (4-5), one seeks to substantiate the velocity dispersion inherent in these equations.

This is most definitively achieved via the conductivity and voltage tuning response of the system, since a knowledge of the phase angle, θ, and the harmonic number, n, are not required, as indicated by the following uniform field expressions (as derived earlier in section 2-5):

$$\frac{d(\ln\omega)}{d(\ln\sigma)} = -\frac{\chi}{4}\left[\frac{4\omega_o^4+3\gamma_+^2\omega_o^2\omega_D^2}{(4\omega_o^2+\gamma_+^2\omega_D^2)^2} + \frac{4\omega_o^4+3\gamma_-^2\omega_o^2\omega_D^2}{(4\omega_o^2+\gamma_-^2\omega_D^2)^2}\right] \tag{4-12}$$

$$\frac{d(\ln\omega)}{d(\ln V)} = \frac{\chi\omega_o^2\omega_D^2}{2}(\gamma_+-\gamma_-)\left[\frac{\gamma_+}{(4\omega_o^2+\gamma_+^2\omega_D^2)^2} - \frac{\gamma_-}{(4\omega_o^2+\gamma_-^2\omega_D^2)^2}\right] \tag{4-13}$$

The relevant data is given by Figures 4-8(a) and 4-8(b), where the experimental points were obtained by first establishing a threshold signal and then carrying out, respectively, small variations in the light intensity and then in the bias voltage.

The changes in light intensity (at fixed bias voltage) introduced variations in the conductivity of the crystal and corresponding frequency shifts in the threshold signal. The magnitude of the latter was measured by the spectrum analyzer in its high resolution mode. In carrying out a rigorous theoretical analysis of the conductivity tuning data a correction for the measured voltage profile

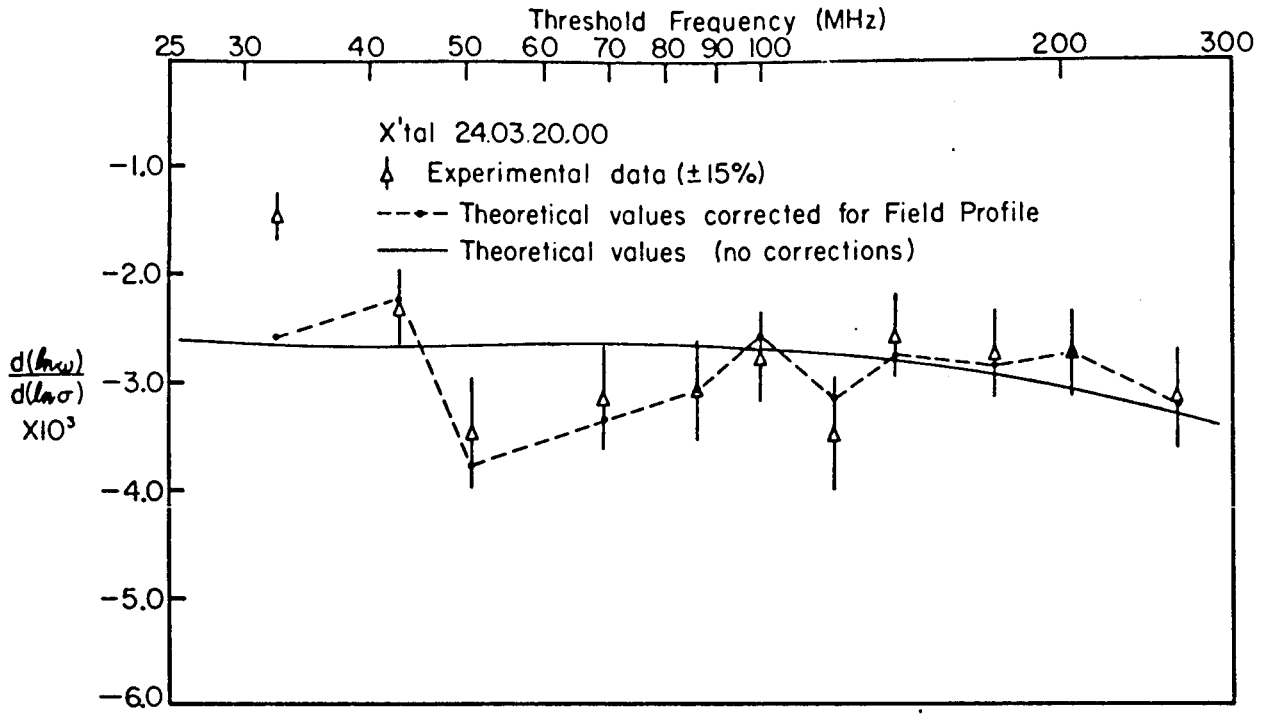

Fig. 4-8(a): X'tal 24.03.20.00; Conductivity Tuning Versus Threshold Frequency

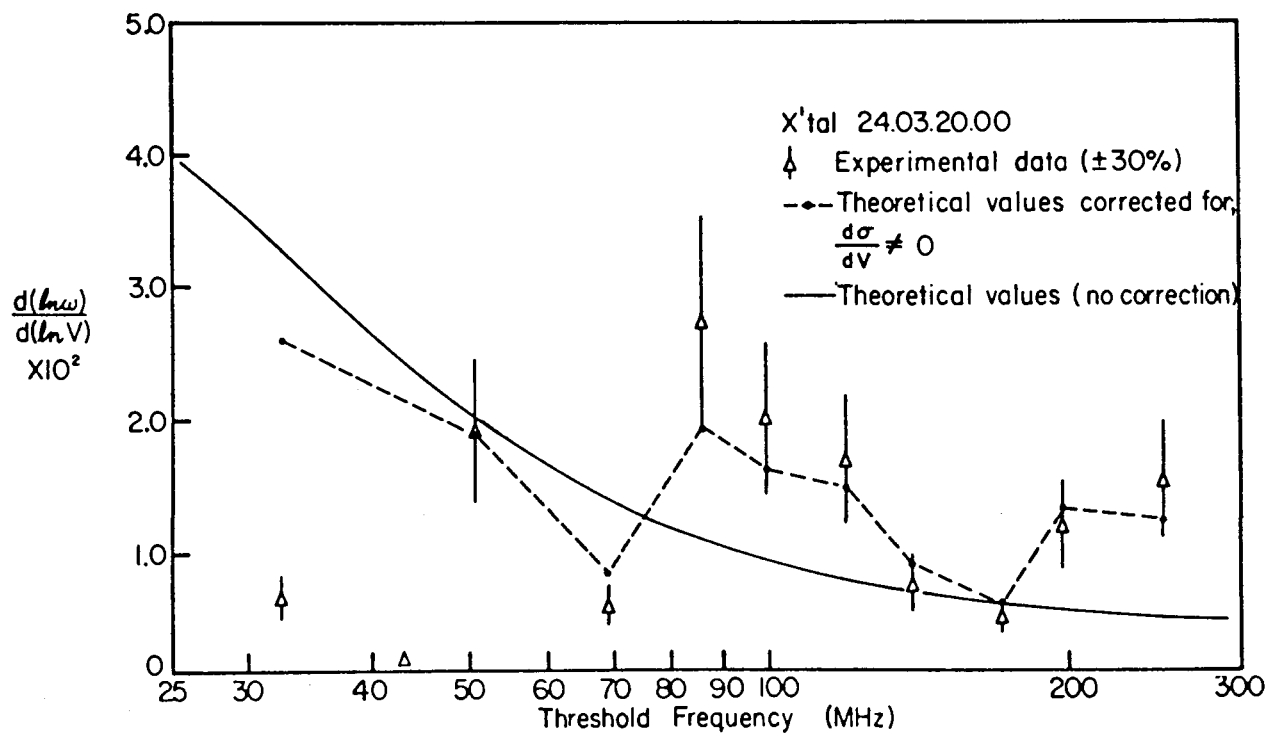

Fig. 4-8(b): X'tal 24,03.20.00; Voltage Tuning Versus Threshold Frequency

was used, viz:

$$\frac{d(\ln\omega)}{d(\ln\sigma)} = \frac{1}{L} \sum_i \frac{d(\ln\omega)}{d(\ln\sigma_i)} l_i \qquad (4\text{-}14)$$

The dashed line of Figure 4-8(a) corresponds to a set of straight lines joining the resulting theoretical points. The solid line of Figure 4-8(a) corresponds to the uniform field expression, equation (4-12), with γ_+ and γ_- evaluated with the aid of equation (4-9) and the data of Table 4-1.

In obtaining the voltage tuning data of Figure 4-8(b) the light level was held constant and a small variation in the bias voltage was introduced from a low frequency oscillator (~10 Hz) via the summing unit of the bias supply. Once again the corresponding frequency shift was monitored by the spectrum analyzer in its high resolution mode.

The theoretical analysis of the voltage tuning data is complicated not only by the presence of a non-uniform field but also by the fact that the conductivity becomes voltage dependent at and above threshold (as evidenced by the non-linear I-V curve of Figure 4-2(a)). Consequently the voltage tuning parameter takes on the following generalized form:

$$\frac{d(\ln\omega)}{d(\ln V)} = \frac{\partial(\ln\omega)}{\partial(\ln V)} + \frac{\partial(\ln\omega)}{\partial(\ln\sigma)} \frac{d(\ln\sigma)}{d(\ln V)} \qquad (4\text{-}15)$$

Now it can be shown that, to a good approximation, the presence of a non-uniform field has little influence on the voltage tuning parameter (as opposed to the conductivity tuning parameter). Thus the principal correction is that indicated by equation (4-15). In carrying out this correction, the I-V curves, at threshold, were used to evaluate, $\frac{d(\ln\sigma)}{d(\ln V)}$. The dashed lines of Figure 4-8(b) correspond to a set of straight lines joining the correspondingly corrected theoretical values. And the solid line corresponds to the simple uncorrected, uniform field expression of equation (4-13).

Aside from one or two anomalous points at the low frequency end of the data, the agreement between experiment and theory is generally quite good and leads to an endorsement of the corresponding theoretical formulation.

CHAPTER V

Conclusions

5-1 Comments on the Fabrication of a Phonon Maser

In structuring a Phonon Maser from CdS the following fabrication sequence was undertaken.

(i) The bulk CdS crystal was first aligned with respect to the desired crystallographic orientation and then cut into wafers (1-2 mm thick).

(ii) The wafers were then annealed in a S_2 atmosphere for 24 hours at 1000°C.

(iii) An individual wafer was then mounted onto the polishing jig and again aligned (under maximum resolution) to the desired crystallographic orientation.

(iv) The surface was then polished flat to within $\lambda_{Na}/2$.

(v) The wafer was then turned over and the second surface polished parallel to the first (to within one second of arc) and equally as flat.

(vi) Ohmic contacts were then made to the faces of the polished wafer.

(vii) And finally the wafer was diced into a number of individual units (~4 mm^2).

In developing this procedure, the polishing steps posed the greatest problem. However, by employing specially fabricated lapping plates, a unique wafer mounting technique, and an interferometric monitoring scheme the problems encountered were eventually overcome.

Another area of considerable difficulty was the application of transparent ohmic contacts to the crystal faces. This was eventually resolved by doping the surfaces with Indium (in an H_2 environment).

The detailed presentation of the fabrication procedure (as reported by Appendix I) corresponds to a sequence of steps capable of producing workable structures and is the result of much trial and error.

5-2 Comments on the Linear Formulation

In chapter IV data was presented in relationship to:

(i) the threshold frequency - current density (conductivity) dependence,

(ii) the threshold velocity - threshold frequency dependence,

(iii) the threshold frequency - temperature dependence,

(iv) the conductivity tuning - threshold frequency dependence, and

(v) the voltage tuning - threshold frequency dependence.

Correspondingly a theoretical analysis, based on the linear formulation of Chapter II was undertaken. On the basis of the resulting high correlation between the experimental and theoretical results one is justified in adopting the linear, phenomenological model as a reasonable representation of the threshold response of a Phonon Maser.

In reality, however, the linear formulation has been tested for active shear mode Phonon Maser structures only. The applicability of the formulation to the active longitudinal structure is in principle suggested. However, a more detailed analysis of the stability of such a configuration needs to be undertaken to guarantee that the principal axis longitudinal mode is indeed activated before some off-axis, quasi-shear mode. This follows from the realization that in general the c-axis longitudinal velocity is larger than an off-axis, quasi-shear velocity and that gain exists for both waves. Consequently it is possible that the quasi-shear threshold field (or more correctly the component of field in the quasi-shear direction) is lower than that

corresponding to the longitudinal mode. If so the quasi-shear mode will be activated first, identifying the longitudinal mode as an unstable configuration. It is important to point out that this problem is not applicable to the active shear mode structure utilized in this study, since the corresponding velocity is a minimum along the principal axis (Vr-71). That is, the active shear mode structure is a stable configuration.

In a further discussion of the acceptability of the linear formulation it is noteworthy to point out that throughout the analysis the influence of trapping centers was ignored completely. This point of view is justified by the apparent success of the analysis and leads one to conclude that trap-free crystals were indeed obtained. The success in obtaining crystals so characterized is attributed to the care taken in annealing the crystals and the virtues of the oxygen desorption associated with the H_2 - Indium diffusion of the Ohmic contacts. Particularly, it was noted that a significant trapping concentration with introduced when Indium diffusion was attempted in the absence of H_2.

5-3 Comments on the Non-Linear Analysis

Upon realizing that the threshold measurements were made on macroscopic signals (stabilized through intrinsic non-linearities) and yet agreed favorably with the linear

formulation, one is lead to conclude that, to first order, the non-linearities have virtually no influence on:

(i) the frequency determination of the threshold signal, or

(ii) the dispersion of the threshold signal.

However, as evidenced by the experiment results, the non-linearities do play a role in:

(iii) the generation of second harmonics,

(iv) the establishment of a non-linear I-V response, and,

(v) gain saturation.

Of these last three points (iii) and (iv) are accounted for (in a qualitative way) by the non-linear analysis of Chapter III. However, the analysis in no way suggests gain saturation and it is not obvious at this point whether a gain limited dispersion relationship can be generated by the inclusion of an inhomogeneous term in the defining set of equations. The existence of gain saturation can, nevertheless, be argued from at least two points of view:

(i) Due to the intrinsic anharmonicity of the phonon-phonon interaction mechanism, the lattice loss term Γ_L, will in general be dependent on signal strength. Consequently as the acoustical signal grows the lattice losses will increase, resulting eventually in an equil-

ibrium situation. In addition as the lattice loss term increases the frequency of maximum gain will be shifted downward in a manner suggested by equations (2-67) and (2-69). Both features are borne out by experiment

(ii) An alternate or, perhaps more realistically, a competing mechanism responsible for gain saturation stems from the realization that as the acoustical signal grows the conduction electrons become concentrated in the potential wells set up by the piezoelectric fields. The net result is a decrease in the effective conductivity of the sample. Upon extrapolating the linear results of equation (2-60) we see that to a first approximation

$$\Gamma_N(\omega_o) \sim \omega_o^2 \sim \sigma_{eff} \qquad (5\text{-}1)$$

Thus as the acoustical signal grows the effective conductivity decreases, resulting in a corresponding decrease in Γ_N. In this way gain saturation is established. In addition, it follows naturally from equation (5-1) that associated with gain saturation is a down shift in the frequency of maximum gain. In

this case it is worthy to note that, whereas, Γ_N is proportional to the effective conductivity, the frequency of maximum gain is only proportional to the square root of σ_{eff}. Thus the principal effect associated with the potential bunching of the conduction electrons is gain saturation, with the down shifting in frequency being of secondary important. Herein we again have qualitative agreement with experimental behavior.

It is noteworthy at this point to make reference to two outstanding papers by P.N. Butcher and N.R. Ogg, (Bu-68) and (Bu-69). Their work consists of a unique, one way travelling wave analysis of the current density non-linearity under consideration. The transposition of their formulation to the two anti-directed travelling waves, characteristic of a Phonon Maser, is however, less than straight forward (due to the cross interaction of the two waves). Nevertheless, their conclusions are qualitatively similar to those presented above, viz: gain saturation and a down shifting in the frequency of maximum gain (brought about by the potential bunching of the conduction electrons and a corresponding decrease in σ_{eff}).

Before concluding this section there remains one further non-linear feature worthy of discussion. The arguments

to be presented, however, are purely speculative at this time.

Experimentally it is observed that once a mode pattern becomes established (corresponding generally to the threshold frequency and its first harmonic) the conductivity and/or drift field have to be altered far beyond that associated with the frequency shift to an adjacent mode before the system, in fact, alters its mode structure. The conclusion drawn from this behavior is that a strong mode locking action becomes established and a significant shift in the frequency of maximum gain is required to bring about a change in the frequency structure. One possible source of this locking action stems from a self generated parametric amplification effect. The argument proceeds as follows.

If in addition to the externally applied D.C. bias field, E_0, one applies an A.C. field, $E_1\cos\omega_1 t$, ($E_0 >> E_1$) then there will be generated counter-directed travelling waves for each principally-directed wave (of frequency, ω) provided, $\omega_1 = 2\omega$. That such waves are indeed generated follows readily from the charge density-electric field product that appears in the expression for the current density, viz:

$$ne^{i(kx-\omega t)}E_1 e^{i2\omega t} = nE_1 e^{i(kx+\omega t)} \qquad (5\text{-}2)$$

$$ne^{i(kx+\omega t)}E_1e^{-i2\omega t} = nE_1e^{i(kx-\omega t)} \qquad (5\text{-}3)$$

Since $E_0 >> E_1$ such terms can be treated as source terms in an iterative calculation similar to that of Chapter III. However, a self consistent analysis, for a one way travelling wave, has been treated by V.M. Levin and L.A. Chernozatonskii (Le-70) resulting in the conclusion that

$$\gamma = 1 - \frac{\mu E_0}{s_0} \rightarrow 1 - \frac{\mu E_0}{s_0} - \alpha(\mu E_1)^2 \qquad (5\text{-}4)$$

where α is a positive frequency dependent function.

The significance of equation (5-4) becomes meaningful to the topic of mode locking when one recalls that the electric fields associated with the non-linear, second harmonic source terms, J_3 and J_4, (equation (3-10) and (3-11)) are virtually spatially independent. Herein then lies the origin of the effective external field, $E_1\cos 2\omega t$. Since such a field reduces the value of E required to maintain the same gain value, the outlined interaction between the fundamental signal and its first harmonic corresponds to the reduction in the total energy of the system resulting in a preferred, stable configuration.

To be rigorous the interaction outlined above must be treated in a self consistent manner, however, as indicated

the necessary elements are present to establish the existence of such a phenomena. Indeed, it is not unlikely that such an interaction mechanism is related, in some way, to the outstanding spectral purity of the maser signal (as documented by the high Q values).

5-4 Area of Future Investigation

The apparent success of the work reported establishes a reasonable theoretical model for the threshold response of a Phonon Maser. With this as a starting point the following areas of future investigation are worthy of consideration.

(i) As indicated in section 5-1 the study undertaken was restricted to an active principal axis, shear mode structure. To established the general applicability of the theoretical formulation, an investigation of the active principal axis longitudinal; the active off-axis, quasi-longitudinal; and the active off-axis, quasi-shear mode structures needs to be undertaken. In doing so the question of mode stability needs to be resolved.

(ii) No attempt was made to monitor the acoustical signal. Acknowledging freely the difficulty in doing so, such information would nevertheless provide an independent

check of the theoretical formulation and also test the applicability of the open circuit voltage-strain relationship, equation (2-95), and the D.C. acoustoelectric current-strain relationship, equation (3-37). In addition the harmonic structure of the acoustical signal should provide further insight into the non-linear features of the system.

(iii) In the experimental study undertaken only the frequency (and its related characteristics) were monitored. In attempting to monitor the wave vectors (though scattering experiments) a whole new area of fruitful investigation is opened up. In principle, further insight into the linear and non-linear features of the system should result.

(iv) On the theoretical front the whole area of a proper non-linear analysis is open to investigation. Out of such an analysis should come a proper formulation of:

(a) harmonic generation,

(b) a non-linear I-V response,

(c) gain saturation,

(d) mode locking, and

(e) line width determination.

The four areas presented here are by no means meant to be a complete survey and undoubtedly new areas will arise as one's understanding of the Phonon Maser phenomenon increases.

Appendix I

Phonon Maser Fabrication

The material used in this study was vapor phase grown CdS that had been purchased from Eagle-Picher Industries, Inc.† It was received in the form of large (~10 c.c.) randomly shaped, single crystals of either A, B, or UHP grade. (For the sake of completeness the physical and electronic characteristics of vapor phase grown CdS are summarized in Appendix II.)

In preparing a CdS crystal capable of Phonon Maser action a number of distinct steps were undertaken. These will now be enumerated with discussion given to the problems encountered and the care required to produce a workable unit.

I-1 Aligning, Wafering and Annealing Procedure

In fabricating a Phonon Maser the large randomly shaped crystal was first mounted onto a goniometer and aligned, using X-ray diffraction, to a preferred crystallographic

---

† Eagle-Picher Industries, Inc., P.O. Box 1090
Miami, Oklahoma, U.S.A., 74354.

orientation. Using a wire saw the crystal was then cut, into 1-2 mm thick wafers, parallel or perpendicular to the polar c-axis (corresponding respectively to a shear or longitudinal maser structure).

To enhance the desired electronic and piezoelectric characteristics of CdS, the wafers were next subjected to an annealing process. This was initiated by thoroughly cleaning the wafers with an ultrasonic cleaner in alternating baths of acetone and methyl alcohol. The wafers were then sealed in an evacuated quartz tube along with a small quantity of 6 nines purity sulfur. The amount of sulfur used was based on a partial pressure of 0.17-0.18 atmospheres of S_2 gas at 1000°C. The quartz tube and its contents were then placed in a furnace and held at a temperature of 1000°C for 24 hours.

The effects of such an annealing process on CdS have been studied by R.B. Wilson (WI-66), D.L. White, et al. (Wh-65), and M.K. Parsons and F.L. English (Pa-67). Their findings indicate the following characteristic changes in CdS;

(i) an increase in the piezoelectric coupling coefficient resulting from;

(a) an improvement in the stoichiometric ratio of Cd and S in normally sulfur deficient, vapor phase grown CdS,

(b) a decrease in the stacking fault density (characteristically responsible for reversing the polarity of the c-axis),

(c) a reduction in the electron trapping density,

(ii) a decrease in the dark conductivity (which in the case of UHP crystals is reduced from an initial value of 10^{-1} $(\Omega\text{-cm})^{-1}$ to a final value of 10^{-6});

(iii) an increase in photoconductivity.

These results are in agreement with the findings of this author and are correlated with greater success in obtaining Phonon Maser action in annealed crystals over crystals that were not annealed.

As noted by Parsons and English (Pa-67) the magnitude of the S_2 partial pressure was of fundamental importance to the success of the annealing process. If the partial pressure was too high, a decrease in the piezoelectric coupling coefficient and an increase in resistivity inhomogeneity was observed. Whereas, if the partial pressure was too low, little change was observed over the un-annealed samples.

I-2 Polishing

Once annealed, the two faces of the wafers were

polished flat, parallel, and perpendicular to the desired crystalographic axis. These three steps were of utmost importance to the successful fabrication of a workable unit and were carried out with great care and precision as attested to by Figs. I-1 and I-2. That is, Fig I-1(a) represents an overall flatness of $\lambda_{Na}/2$, Fig. I-2(b) an overall parallelism of under 2 seconds of arc, and Figs. I-2 a crystalographic alignment to within 30 minutes of arc.

In carrying out these steps a crystal wafer was first mounted onto the head of a Logitech† polishing jig. The jig is constructed with a gimbal adjustment which allows one to align the surface to be polished at any angle with respect to the polishing plane. Utilizing this feature the mounted crystal was aligned once again via X-ray diffraction such that the desired crystalographic axis was perpendicular to the polishing plane. The precision to which this could be done was limited by the spot size of the X-ray patterns and was of the order of 30 minutes of arc.

The polishing was carried out using diamond abrasive on a sequence of tin plates, each corresponding to

---

† Logitech Ltd., 128 Bank St., Alexandria, Dunbartonshire, Scotland.

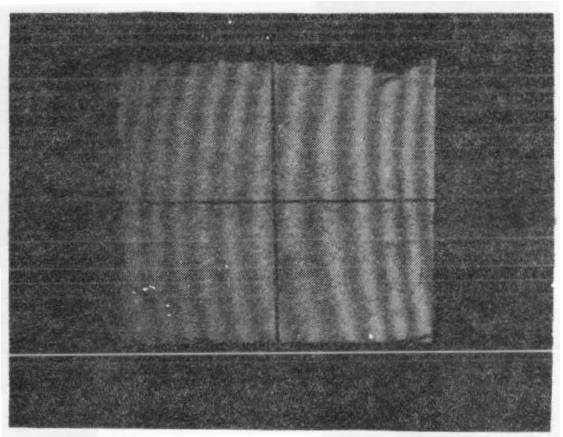

Fig. I-1 (a): Flatness Interference Pattern

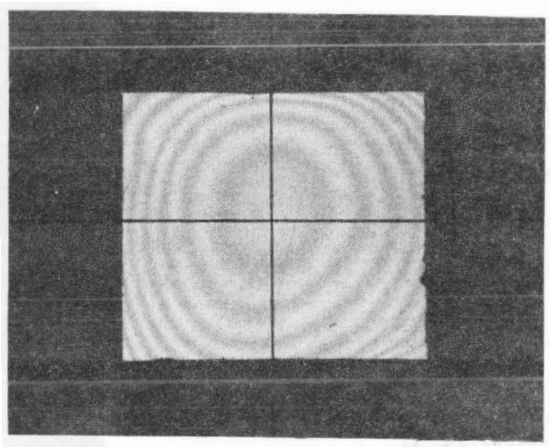

Fig. I-1 (b): Parallelism Interference Pattern

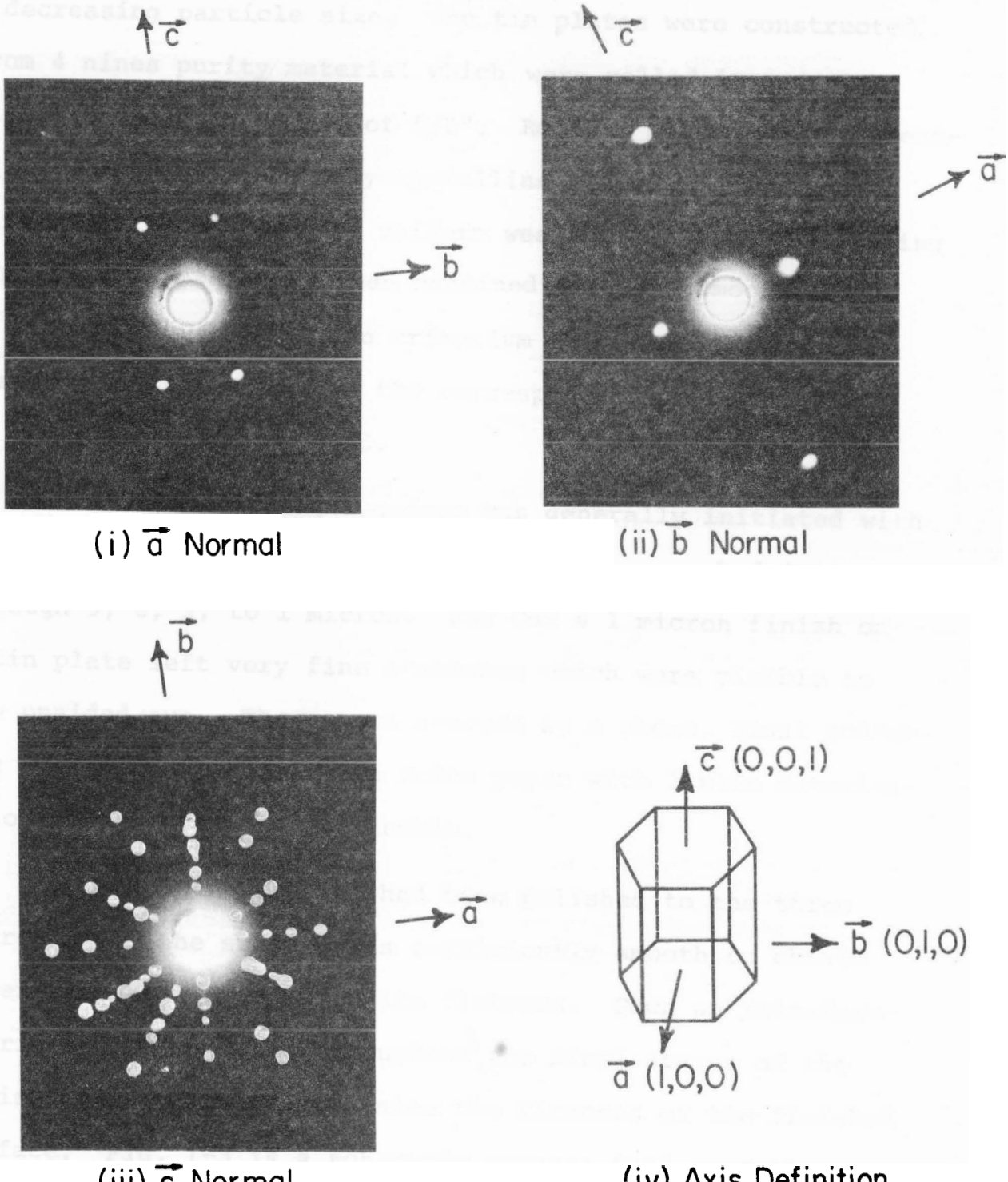

FIG. I-2: PRINCIPAL AXIS X-RAY DIFFRACTION PATTERNS

a decreasing particle size. The tin plates were constructed from 4 nines purity material which were rolled in a common direction to a thickness of 5/8". Rolling served to preferentially align the tin's polycrystalline structure in a common direction, resulting in a uniform wearing action. The lapping surface of a plate was then machined flat and smooth on a lathe, subject to the criterium that the lathe grooves were to be no deeper than the corresponding particle size of the abrasive to be used.

The polishing sequence was generally initiated with a particle size of 15 microns from which one worked down through 9, 6, 3, to 1 micron. For CdS a 1 micron finish on a tin plate left very fine scratches which were visible to the unaided eye. These were removed by a short, final polishing of 1 micron abrasive on Pelon paper with little deterioration to the flatness attainable.

Once the crystal had been polished to the three micron level the surface was sufficiently smooth to obtain interferometric data as to its flatness. Such an interferometric scheme was used throughout the final stages of the polishing sequence to guarantee the flatness of the finished surface. Fig. I-3 is a schematic representation of the interferometer arrangement and Fig. I-1(a) is an example of the interference pattern obtained.

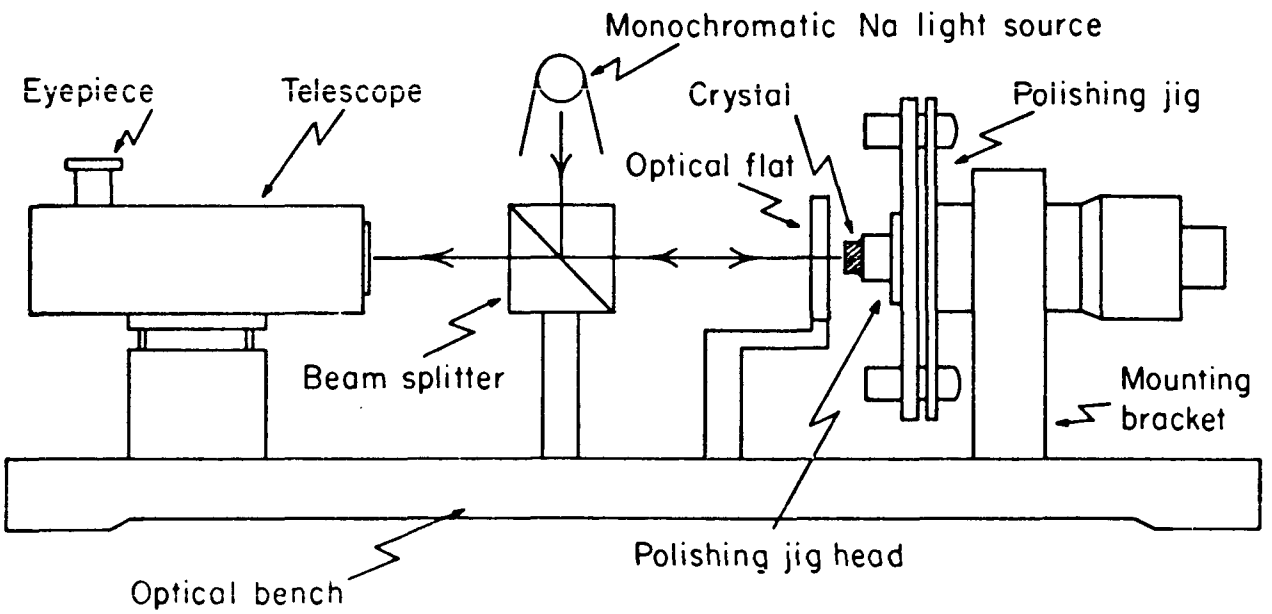

Fig. I-3: Flatness and Parallelism Interferometer System

In setting up the interferometer the polishing jig was transferred to a support which placed the crystal face next to an optical flat and at a slight angle with respect to it. The optical flat was of known flatness, viz: $\lambda_{Na}/10$, and served as a standard for the measurement. The crystal face was then illuminated with monochromatic light by means of a beam splitter. With the spacing between the optical flat and the crystal less than the coherence length of the light, a local interference pattern was set up. This could be viewed directly, however, a telescope was used since it not only magnified the pattern but also allowed a record to be taken via a camera attachment to the eyepiece.

If the crystal face was perfectly flat, the slight angle between it and the optical flat would generate an interface pattern of alternating light and dark straight lines. The spacing between two adjacent dark lines would be inversely proportional to the angle between the two surfaces and would correspond to half a wavelength increase in the spacing as one moved along the face of the crystal, away from the apex of the angle. Any deviation from the straight line pattern represented a measureable degree of non-flatness of the crystal face. As can be seen from Fig. I-1(a) this deviation is of the order of $\lambda_{Na}/2$ for the overall crystal. It is to be noted that while the flatness measurement utilized optical wavelengths, the unit was ultimately subject to acoustical wavelengths which

were typically 20 times longer. Thus as an acoustical system the results of Fig. I-1(a) represent a surface of high specular reflection, that is, one possessing a high degree of spacial coherence.

Once the first surface of the wafer had been polished to one's satisfaction the crystal was turned over and the second surface polished equally as flat and in addition parallel to the first. The degree of parallelism not only influenced the, Q, of the one dimensional cavity but also determined the proper crystalographic orientation of the second surface.

To obtain the degree of parallelism desired one proceeded as follows. First the second crystal face was polished to the 3 micron level which, as already noted provides a reasonable reflecting surface. A laser was then used to obtain a crude degree of parallelism by:

(i) directing the beam at the crystal face;

(ii) noting the distance, S, between the two beams reflected respectively from the front and back surfaces;

(iii) adjusting the jig so as to move the spot reflected from the back surface a distance, $\Delta S = 0.40S$[†], along the line joining the

---

[†] ΔS is based on the formula, $\Delta S/S = 1/n$, where, n, is the index of refraction.

original spots; and then

(iv) repolishing the surface to this new orientation.

The spot spacing quickly converged to zero in two or three cycles of the above procedure and with a long optical path the degree of parallelism obtained was good to within a few minutes of arc. The precision obtainable was ultimately limited by the spot size of the laser beam.

At this point one resorted to an interferometric measurement to improve the resolution. The same arrangement, Fig. I-3, was used except now the optical flat was removed and one monitored the local interference pattern set up by the front and back surfaces of the crystal. If the two surfaces were perfectly flat and parallel, the interference pattern would consist of a completely dark or light image over the whole face of the crystal, depending on whether it were an even or odd number of half wavelengths thick. Deviations from this idealized condition are characterized by the ring pattern of Fig. I-1(b).

In establishing parallelism the objective was to place the center of the ring pattern in the center of the crystal and to minimize the number of rings in the pattern (for each new ring represented a variation in thickness of $\lambda_{Na}/2$ and thus a deviation from parallelism). With the ring pattern in the center of the crystal one could attribute the

remaining degree of non-parallelism to the non-flatness of the two sides. That is, the ring structure resulted from the crystal being slightly convex. The pattern represented by Fig. I-1(b) indicates a slightly convex shape with a non-parallelism of under 2 seconds of arc for the worst regions.

Throughout the polishing sequence it was mandatory that the crystal remain rigidly bonded to the head of the polishing jig in order to attain the degree of flatness and parallelism desired. Initially this was achieved by using an acetone soluble adhesive tradenamed Crystalbond 509[†]. To make the bond, the jig head and the crystal were heated to a temperature of not less than 170°F. At this temperature the crystal bond became fluid and tacky and was easily transferred to the two items. Once coated with the adhesive the jig head and crystal were mated and allowed to cool. The resulting bond proved suitable rigid and in addition was easily released in an acetone bath. However, in spite of its many virtues this material had to be abandoned. For it was eventually discovered that in heating the crystal to 170°F, electron trapping levels were introduced, the density of which in most cases proved sufficient to extinguish the maser action. Subsequently, the following cold bonding scheme

---

[†]Obtained from Aremco Products, Inc., P.O. Box 145, Briarcliff Manor, N.Y. 10510, U.S.A.

was introduced which overcame this problem.

The jig head and crystal were painted with a soluble adhesive and allowed to dry. (For this, commercial fingernail polish was used.) The painted crystal was then bonded to the jig head by a hard setting epoxy. Once cured, the epoxy provided a rigid bond which could be removed later in an acetone bath. (For, while the acetone had little effect on the epoxy, it would nevertheless dissolve the thin layer of adhesive paint, thereby releasing the crystal.)

I-3 Application of Ohmic Contacts

The remaining step in the fabrication of a Phonon Maser was the application of ohmic contacts to the two polished faces of the crystal. With the objective in mind of controlling the conductivity of the crystal via its photoconductive response, this could be done in either of two ways. Namely, if the faces were to be illuminated the contacts must be optically transparent, whereas, if the edges were to be illuminated they could be opaque. The two options will now be discussed in detail, with the starting point in each case being a crystal that has been thoroughly cleaned in alternating baths of acetone and methyl alochol.

For edge illumination a simply evaporation of from 500 to 1000 Å of Indium was sufficient to establish an ohmic contact. Indium was used because of its ability to make a

more truly ohmic contact with CdS than any other metallic material. Nevertheless, other materials such as Gallium and Aluminum (Pi-67) have been used with reasonable success.

For the optically transparent contacts the procedure was somewhat more involved and was based on a modified technique reported by Y.T. Sihvonen and D.R. Boyd (Si-60). In this case the polished crystal was placed within a pyrex tube along with a small quantity (~100 mgm) of Indium. The tube was evacuated (10^{-6} mm of Hg) and then filled, with H_2 gas, to a partial pressure of 0.5 atmospheres. Once filled, the tube was then sealed off. (It is recommended that the tube be of reasonable length (~20 cm) and that it be sealed as quickly as possible so as to minimize any heating and thus alteration in the partial pressure of the encapsulated H_2 gas.)

Once sealed, the tube was placed in a furnace which had been preheated to 500°C. The tube and its contents were maintained at this temperature for 10 minutes, then removed and allowed to quench quickly to room temperature.

The net result of this procedure was the production of an optically transparent ohmic contact by the diffusion of Indium into the crystal and the formation of a highly doped n-type surface layer. The purpose of the H_2 gas, over and above preventing an evaporation layer from forming, was

to exploit its chemical reducing character to clean the crystal surface of oxygen (which is readily absorbed by CdS). This not only enhanced the diffusion rate but also guaranteed a more uniform diffusion depth. For the time, temperature, and H partial pressure specified the diffusion depth, as monitored by the field profile of a biased crystal, was typically 50μ and characterized by a surface impedance of under 200 Ω/square.

An important feature to note in using this procedure, is to avoid rubbing the surfaces of the crystal. For in spite of its transparent appearance there is, nevertheless, a very thin layer of Indium on the surface, which from experience was found to play an important role in forming the contact but unfortunately could be easily removed. It is even suggested that a thin (~50 A) evaporated overcoating of Gold or Aluminum be applied to protect this layer.

Throughout most of the work relating to this thesis the diffusion contact scheme was used because a more uniform spacial conductivity could be obtained by facial illumination over edge illumination.

Having successfully formed an ohmic contact the edges of the wafer were trimmed to remove all shunting electrical paths. The resultant wafer constituted a usable Phonon Maser. However, in most cases the wafer was diced

into a number of smaller sections (~4 mm^2) to produce several identical units. In this way up to 30 units (~4 mm^2) were produced from a single wafer with a yield approaching 100%.

Appendix II

Physical and Electronic Properties of CdS

The following data is a summary of the physical and electronic properties of vapor phase grown CdS and are taken from the compilation prepared by M. Neuberger (Ne-69).

Molecular weight	144.476
Density	4.820 gm/c.c.
Hardness	3-3.5 Mohs
Cleavage Axis	[1, 0,0]
Symmetry	hexagonal, wurtzite (6mm)
Lattice spacing	a = 4.1368 Å
	c = 6.7162 Å
	Cd-S = 2.526 Å
Phase Transition (Hex. to Cubic)	33kbars @ 300°K
Melting Point	1475 ± 15°C @ 100 Atms.
Sublimation Point	1350 °C @ 1 atms.
Specific Heat	0.080 cal/gm°K @ 300°K
Debye Temperature	286°K
Thermal Conductivity	0.2 watts/cm°K @ 300°K
Thermal Expansion	
along a-axis	$4.0\ 10^{-6}$ /°K
along c-axis	$2.1\ 10^{-6}$ /°K

Electron Mobility	200-350 $cm^2/V\text{-}sec$ @ 300 K
Hole Mobility	10-15 $cm^2/V\text{-}sec$ @ 300 K
Electron Effective Mass	0.20 M_o
Energy Gap	
E || C	2.425 ev @ 300 K
E $\perp$ C	2.410 ev @ 300 K
Work Function	5.01 ev
Electron Affinity	4.79 ev
Refractive Index	
n_o	2.506 @ λ = 6000 Å
n_e	2.491 @ λ = 6000 Å
Inversion Point ($n_o = n_e$)	5270 Å

Stiffness Tensor (MC-69)

c_{ij}	Value ($\times 10^{11}$ dynes/cm^2)
c_{11}	8.59
c_{12}	5.33
c_{13}	4.61
c_{33}	9.38
c_{44}	1.49
$c_{66} = \frac{1}{2}(c_{11}-c_{12})$	1.63

Piezoelectric Tensor (MC-69)

β_{ij}	Value ($\times 10^4$ statcoul/cm^2)
β_{15}	-6.37
β_{31}	-7.78
β_{33}	14.4

Dielectric Tensor (MC-69)

$\underleftrightarrow{\varepsilon}_i$	Value
ε_1	9.02
ε_2	9.02
ε_3	9.53

Velocity of Sound (MC-69)

s_o	Value (cm/sec)
long. (// c-axis)	4.41×10^5
shear ($\perp$ c-axis)	1.76×10^5

Appendix III

Data Tabulation

The following data tables correspond to the experimental and theoretical analysis of Chapter IV.

Table III-1

Threshold Frequency Versus Current Density

(Re: Fig. 4-4(a))

X'tal 24.01.02.03
L = 1200μ, A = 7.38 mm^2
T = 14°C
μ = 370 cm^2/V-sec

J	f_n(Exp't)	f_n(Th.-corrected)
ma/cm^2	MHz	MHz
3.73	59.886	27.759
7.32	59.007	38.693
16.26	58.973	56.174
38.75	83.573	83.901
56.91	99.191	100.066
83.33	117.066	119.877
108.40	131.948	134.162
151.76	155.785	154.622
222.22	187.018	182.291

Table III-2

Threshold Frequency Versus Current Density

(Re: Fig. 4-4(b))

X'tal 24.03.20.00
L = 582μ, A = 3.59 mm^2
T = 10°C
$\bar{\mu}$ = 310 cm^2/V-sec

J	f_n(Exp't)	f_n(Th.-corrected)
ma/cm^2	MHz	MHz
5.07	32.299	31.337
12.70	42.887	45.751
16.16	56.673	54.816
22.58	68.900	66.940
30.66	82.701	78.083
47.80	96.386	94.879
78.04	119.302	118.688
122.60	139.281	143.689
206.24	171.372	177.086
306.60	204.930	206.299
515.61	266.184	264.250
808.25	299.603	306.718
1198.40	370.307	367.613

Table III-3

Threshold Velocity Versus Threshold Frequency

(Re: Fig. 4-5(a))

X'tal 24.01.02.03

$\frac{-2\ln r}{L} = 5.0\ cm^{-1}$

$\bar{\mu} = 370\ cm^2/V\text{-}sec$

f (Exp't)	v/s_o (Exp't)	v/s_o (Theory)
MHz		
58.973	1.129	1.116
83.573	1.181	1.121
99.191	1.139	1.142
117.066	1.177	1.163
131.948	1.241	1.188
155.785	1.301	1.266
187.018	1.337	1.335

Table III-4

Threshold Velocity Versus Threshold Frequency

(Re: Fig. 4-5(b))

X'tal 24.03.20.00

$-\frac{2\ln r}{L} = 6.0\ cm^{-1}$

$\mu = 310\ cm^2/V\text{-}sec$

f_n(Exp't)	v/s_o(Exp't)	v/s_o(Theory)
MHz		
32.299	1.108	1.234
42.887	1.236	1.154
56.673	1.156	1.143
68.900	1.091	1.108
82.701	1.074	1.120
96.386	1.108	1.136
119.302	1.169	1.164
139.281	1.213	1.182
171.372	1.356	1.264
204.930	1.457	1.333
266.184	1.493	1.464
299.603	1.708	1.608
370.307	1.732	1.770

Table III-5

Threshold Frequency, Mobility, and Q Versus Temperature

(Re: Figs. 4-6 and 4-7)

X'tal 24.03.20.00

$J = 41.80$ ma/cm^2

$\frac{-2\ln r}{L} = 5.0$ cm^{-1}

$\mu_o = 2.301 \times 10^3$ (cm^2/V-sec)
$a = 6.92 \times 10^{-3}$ (°K)$^{-1}$
$\Big\}$ $\mu = \mu_o e^{-aT}$

$Q_o = 7.851 \times 10^9$
$a = 2.732 \times 10^{-2}$ (°K)$^{-1}$
$\Big\}$ $Q = Q_o e^{-aT}$

T	f_n(Exp't)	f_n(Th.-corrected)	μ	Q
°C	MHz	MHz	cm^2/V-sec	
-20	90.346	93.512	410	7.53×10^6
-10	91.852	92.073	370	6.12×10^6
0	91.824	90.835	340	4.59×10^6
10	93.348	89.456	320	3.73×10^6
20	93.320	88.318	300	2.33×10^6
30	93.323	87.069	290	2.07×10^6

Table III-6

Conductivity Tuning Versus Threshold Frequency

(Re: Fig. 4-8(a))

X'tal 24.03.20.00

f_n (Exp't)	$\frac{d(\ln\omega)}{d(\ln\sigma)}$ (Exp't)	$\frac{d(\ln\omega)}{d(\ln\sigma)}$ (Th.-corrected)
MHz		
32.299	-1.47×10^{-3}	-2.59×10^{-3}
42.887	-2.31×10^{-3}	-2.23×10^{-3}
50.548	-3.47×10^{-3}	-3.77×10^{-3}
68.900	-3.15×10^{-3}	-3.34×10^{-3}
85.746	-3.08×10^{-3}	-3.07×10^{-3}
99.474	-2.77×10^{-3}	-2.57×10^{-3}
117.886	-3.49×10^{-3}	-3.16×10^{-3}
136.120	-2.57×10^{-3}	-2.74×10^{-3}
171.372	-2.74×10^{-3}	-2.85×10^{-3}
204.930	-2.73×10^{-3}	-2.73×10^{-3}
261.572	-3.15×10^{-3}	-3.21×10^{-3}

Table III-7

Voltage Tuning Versus Threshold Frequency

(Re: Fig 4-8(b))

X'tal 24.03.20.00

f_n (Exp't)	$\frac{d(\ln\omega)}{d(\ln V)}$ (Exp't)	$\frac{d(\ln\omega)}{d(\ln V)}$ (Th.-corrected)
MHz		
32.299	6.69×10^{-3}	2.61×10^{-2}
42.887	2.04×10^{-3}	2.15×10^{-2}
50.548	1.92×10^{-2}	1.88×10^{-2}
68.900	5.99×10^{-3}	8.53×10^{-3}
85.746	2.73×10^{-2}	1.94×10^{-2}
99.474	2.01×10^{-2}	1.63×10^{-2}
119.302	1.70×10^{-2}	1.47×10^{-2}
139.281	7.68×10^{-3}	9.07×10^{-3}
171.372	5.23×10^{-3}	6.14×10^{-3}
197.352	1.21×10^{-2}	1.33×10^{-2}
249.292	1.55×10^{-2}	1.25×10^{-2}

Bibliography

Ad-66 E.L. Adler and G.W. Farnell; J. Acoust. Soc. of Am. 39, 960, (1966)

Ba-68 V.I. Baibakov; Sov. Phys. -S.S. 10, 533, (1968)

Bu-68 P.N. Butcher and N.R. Ogg; J. Phys. D. 1, 1271, (1968)

Bu-69 P.N. Butcher and N.R. Ogg; J. Phys. D. 2, 333, (1969)

Ec-63 S.G. Eckstein; Phys. Rev. 131, 1087, (1963)

Gu-66 V.L. Gurevich and B.D. Laikhtman; Sov. Phys. - S.S. 7, 2603, (1966)

Gu-68 Yu. V. GulyaeV and V.V. Proklov; Sov. Phys. - Semi. 1, 1245, (1968)

Gu-69 V.L. Gurevich; Sov. Phys. - Semi. 2, 1299, (1969)

Hi-69 F.S. Hickernell; Tech. Report: RADC - 7R -68 - 489, Jan. (1969)

Hu-59 A.R. Hutson; J. Phys. Chem. of Solids 8, 467, (1959)

Hu-60 A.R. Hutson; Phys. Rev. Letters 4, 505, (1960)

Hu-61 A.R. Hutson, et al.; Phys. Rev. Letters 7, 237, (1961)

Hu-62 A.R. Hutson and D.L. White; J. Applied Phys. 33, 40, (1962)

Hu-70 A.J. Hughes, et al.; J. Phys. D. 3, 751, (1970)

In-29 International Critical Tables; 5, 221, (1929)

Ki-67 Y. Kikuchi, et al.; Japan. J. Appl. Phys. 6, 1251, (1967)

Ko-64 E.D. Kolb and R.A. Laudise; J. Amer. Ceram. Soc. 48, 342, (1964)

Ky-54 J.J. Kyame; J. Acoust. Soc. of Am. 26, 990,(1954)

Le-70 V.M. Levin and L.A. Chernozatonskii; Sov. Phys. - S.S. 11, 2679, (1970)

Ma-50 W.P. Mason, "Piezoelectric Crystals and Their Applications to Ultrasonics" (D. Van Nostrand Co. Inc., N.Y. 1950) p. 84

Ma-67 J.D. Maines; S.S. Comm. 5, 271, (1967)

Ma-69 J.D. Maines and E.G.S. Paige; J. Phys. C. 2, 175, (1969)

Ma-70 R. Mauro and W.C. Wang; Phys. Rev. B 1, 683,(1970)

MC-69 J.G. McCallum; Ph.D. Thesis, Simon Fraser University (1969)

MF-63 J.H. McFee; J. of Appl. Phys. 34, 1548, (1963)

MF-66 J.H. McFee; "Physical Acoustics" (Academic Press, N.Y.; Edited by W.P. Mason, 1966) Vol. IV, part A, p. 1

Mr-69 F.G. Marshall; Electron. Lett. 5, 581, (1969)

Mr-70 F.G. Marshall; Electron. Lett. 6, 243, (1970)

Ne-69 M. Neuberger; "II - VI Semiconducting Compounds Data Tables (Electronic Properties Information Center, Hughs Aircraft Co., U.S.A., 1969)

Ni-60 H.D. Nine; Phys. Rev. Lett. 4, 359, (1960)

Ny-60 J.F. Nye; "Physical Properties of Crystals" (Oxford Press, Great Britain, 1960)

Pa-67 M.K. Parsons and F.L. English; Appl. Phys. Lett. 11, 283, (1967)

Pi-67 F.A. Pizzarello; J. of Appl. Phys. 38, 1752, (1967)

Si-60 Y.T. Sihvonen and D.R. Boyd; Rev. of Sc. Inst. 34, 992, (1960)

Sp-62 H.N. Spector; Phys. Rev. 127, 1084, (1962)

Sp-63 H.N. Spector; Phys. Rev. 130, 910, (1963)

Sp-68 H.N. Spector; Phys. Rev. 165, 562, (1968)

Vr-71 J. Vrba; Private Communication, (1971)

We-56 G. Weinreich; Phys. Rev. 104, 321, (1956)

Wh-62 D.L. White; J. Appl. Phys. 8, 2547, (1962)

Wh-65 D.L. White, et al.; Proc. of IEEE 53, 2157, (1965)

Wh-66 D.L. White and W.C. Wang; Phys. Rev. 149, 628 (1966)

Wi-66 R.B. Wilson; J. Appl. Phys. 37, 1932, (1966)